

UPPER MANTLE VELOCITY STRUCTURE BENEATH THE
TIBETAN PLATEAU FROM TRIPLICATED SEISMIC *P*
WAVEFORMS

Risheng Chu, B.S.

An Abstract Presented to the Graduate Faculty of
Saint Louis University in Partial Fulfillment
of the Requirements for the Degree of
Doctor of Philosophy

2008

Abstract

In this study, P -wave waveforms in the upper-mantle distance range between 12° and 30° were analyzed to investigate upper-mantle P velocity structures beneath the Tibetan Plateau and surrounding areas. The waveform data were from 1,715 earthquakes of magnitudes larger than 5.0 between 1990 and 2005 that occurred within 30° from the center of the plateau. I first used teleseismic recordings of these events to verify their focal mechanisms from the Harvard CMT solutions and found 504 events with good focal mechanisms. I then developed a new method to estimate their source time functions and focal depths. For each event, I used the theoretical Green's functions to deconvolve with the teleseismic P -wave waveforms to obtain the source time function. The focal depth of the event was adjusted until the source-free P waveforms match the theoretical Green's functions. By using the method I obtained source time functions and depths for the 504 events. Comparison with the Harvard CMT solutions showed that Harvard CMT catalog systematically over-estimated both the source durations and depths.

I divided the studying area into 6 regions and modeled upper-mantle-distance P waveforms with turning points beneath each region separately. The results show that the upper-mantle P -wave velocity structures beneath India, the Himalayas and the Lhasa Terrane are similar and contain a high-velocity lid about 250 km thick. The Tarim Basin also lies above a high-velocity upper-mantle lid. The upper-mantle velocities over 200 km beneath the Qiangtang and Songpan-Ganzi Terranes are lower than those in the north and south, especially beneath the Songpan-Ganzi Terrane. The 410 discontinuity beneath these two terranes are elevated by 20 km. I also found high-velocity anomalies in the transition zone below 500 km under the Lhasa and Qiangtang Terranes. The results suggest that the Tibetan Plateau was generated by the thrusting of the Indian mantle lithosphere under the southern part

of Tibet. A portion of the thickened Asian lithosphere in northern Tibet was delaminated and is now sitting atop of the 410 discontinuity below it. The high-velocity anomalies in the transition zone beneath the Lhasa and Qiangtang Terranes are probably the remnants of subducted India mantle lithosphere.

UPPER MANTLE VELOCITY STRUCTURE BENEATH THE
TIBETAN PLATEAU FROM TRIPLICATED SEISMIC *P*
WAVEFORMS

Risheng Chu, B.S.

A Dissertation Presented to the Graduate Faculty of
Saint Louis University in Partial Fulfillment
of the Requirements for the Degree of
Doctor of Philosophy

2008

© Copyright by
Risheng Chu
ALL RIGHTS RESERVED

2008

COMMITTEE IN CHARGE OF CANDIDACY:

Associate Professor Lupei Zhu,
 Chairperson and Advisor

Professor Robert B. Herrmann

Associate Professor Keith D. Koper

Dedication

This dissertation is dedicated to my wife, Meng Shen, my parents, and my unborn baby.

Acknowledgments

First, I must gratefully and sincerely thank my academic advisor, Dr. Lupei Zhu, for his generous help during my study at Saint Louis University. It is he who has supported and supervised me for more than five years. He guides me into the world of seismology and inspires me to do scientific research. He is not only a perfect advisor on research, but a helpful friend in my daily life. Every person I have met has the same praise, “Lupei is very nice and knowledgeable.”

Second, I thank my committee members, Dr. Robert B. Herrmann and Dr. Keith Koper for their careful review of my dissertation. I also thank other faculty members of the Department of Earth and Atmospheric Sciences, especially Dr. David J. Crossley, Dr. John Encarnición, Dr. Brian J. Mitchell, and Dr. David Kirschner. They have taught me all the necessary knowledge on seismology, geophysics, and geology. Without them, I could not have reached this achievement.

I cannot forget the department staff, Eric J. Haug, Bob Wurth, Cynthia Wise, and Laurie Hausmann. They gave me much help on technical issues, traveling, and course registration.

Moreover, discussions with Don V. Helmberger (Caltech), Chang Li (MIT), Arwen Deuss (Cambridge), and Bin Chen (UIUC) were very helpful and guided me during this research.

I would like to acknowledge Dr. Guoming Xu, my undergraduate supervisor at the University of Science and Technology of China (USTC), who is a very nice person. When I was facing my first difficult choice between Saint Louis University and a German institution, he told me, “Go to the United States, you can learn what you want to learn.” I will always remember his words in my heart.

I’m grateful to Ying Ye, Hongyi Li, and Horng-Shiuann Wu for the help which they provided when I first came to the United States. Without their help, my life

would have been much harder. I thank here Xian Qi and all graduate students of the EAS department for their friendship during these years.

I'm thankful to my parents for their continuous support and encouragement through my education. I would also like to thank my beloved wife Meng Shen for her love, sacrifices, and kindness.

This dissertation work has been funded by the U.S. National Science Foundation through grant EAR-0439992. A special acknowledgment must be given to Data Management Centers of IRIS and Institute of Earth Science, Academia Sinica, Taiwan, for providing high-quality seismic waveform data, which has made this study possible.

Table of Contents

List of Figures	viii
List of Tables	xi
Chapter 1: Introduction	1
Chapter 2: Review of Literature on the Lithospheric and Upper-mantle Structures beneath the Tibetan Plateau	7
2.1 Earthquake depth and focal mechanism studies	7
2.2 Modeling waveforms at upper-mantle distances	9
2.3 Surface wave dispersion inversion and tomography	10
2.4 Receiver function analysis	12
2.5 Travel-time tomography	13
Chapter 3: Method and Data	16
3.1 Determine velocity structure using waveforms at upper-mantle distances	16
3.2 Data	21
3.2.1 Event selection and station locations	21
3.2.2 Preliminary data processing	23
Chapter 4: Earthquake Source Time Functions and Focal Depths	25
4.1 Introduction	25
4.2 Procedure	26
4.2.1 Verify CMT solutions and revise focal depths	26
4.2.2 Estimate earthquake source time functions and depths	28
4.3 Comparison of focal depths and source durations with the Harvard CMT solutions	32
4.4 Source scaling relations of earthquakes around the Tibetan Plateau	32
4.5 Focal depths and mechanisms in and around Tibet	35
4.5.1 The Tibetan Plateau	35
4.5.2 Hindu-Burma	37
4.5.3 Pamir-Hindu Kush	38
Chapter 5: Upper-mantle Velocity Structure Beneath the Tibetan Plateau and Surrounding Areas	40
5.1 Lateral velocity variations revealed by upper-mantle distance waveforms	40
5.2 Waveform modeling and results	49
Chapter 6: Discussion and Conclusions	73
6.1 Uncertainties of the upper-mantle velocity structure	73

6.2	Comparison of the upper-mantle velocity structures with results from previous studies	75
6.3	Implications	76
6.4	Conclusions	78
	References	80
	Vita Auctoris	91

List of Figures

Figure 1.1: Tectonic setting of the Tibetan Plateau	2
Figure 1.2: Mechanisms of India-Eurasia collision	4
Figure 2.1: TIP velocity model	11
Figure 3.1: P -wave triplication profile between 12° and 26°	17
Figure 3.2: Waveforms at the upper-mantle distances for the sensitivity test	19
Figure 3.3: Trade-off of waveform modeling	20
Figure 3.4: Seismicity of the study area	22
Figure 3.5: Station locations of seismic recording experiments	23
Figure 4.1: Locations of 504 earthquakes used	27
Figure 4.2: Inversion of source time function for event 19980502083650 . .	29
Figure 4.3: Inversion of source time function for event 20030726231817 . .	30
Figure 4.4: Inversion of source time function for event 20040810014732 . .	31
Figure 4.5: Focal depths and source durations	32
Figure 4.6: Source durations versus M_w and depths	33
Figure 4.7: Focal depth distribution in and around the Tibetan Plateau .	34
Figure 4.8: Focal depth profiles	36
Figure 5.1: Distribution of turning-points of waveforms	41

Figure 5.2: <i>P</i> -wave profile for event 19900109022926	42
Figure 5.3: <i>P</i> -wave profile for event 19921204113636	43
Figure 5.4: <i>P</i> -wave profile for event 19940701101241	44
Figure 5.5: Travel time residuals below the 660 discontinuity.	45
Figure 5.6: Travel time residuals in the transition zone.	46
Figure 5.7: Travel time residuals above the 410 discontinuity.	47
Figure 5.8: A travel-time residuals profile	48
Figure 5.9: Waveform profile before the depth correction	50
Figure 5.10: Waveform profile after the depth correction	51
Figure 5.11: Turning points beneath India	53
Figure 5.12: Waveform fits for India	54
Figure 5.13: <i>P</i> -wave velocity model for India	55
Figure 5.14: Turning points beneath the Himalayas	56
Figure 5.15: Waveform fits for the Himalayas	57
Figure 5.16: <i>P</i> -wave velocity model for the Himalayas	58
Figure 5.17: Turning points beneath the Lhasa Terrane	59
Figure 5.18: Waveform fits between 24.5° and 26° for the Lhasa Terrane	59
Figure 5.19: Waveform fits for the Lhasa Terrane	60
Figure 5.20: <i>P</i> -wave velocity model for the Lhasa Terrane	61

Figure 5.21: Turning points beneath the Qiangtang Terrane	62
Figure 5.22: Waveform fits between 23° and 28° for the Qiangtang Terrane	62
Figure 5.23: Waveform fits between 19° and 23° for the Qiangtang Terrane	63
Figure 5.24: Waveform fits for the Qiangtang Terrane	64
Figure 5.25: <i>P</i> -wave velocity model for the Qiangtang Terrane	65
Figure 5.26: Turning points beneath the Songpan-Ganzi Terrane	66
Figure 5.27: Waveform fits for the Songpan-Ganzi Terrane	67
Figure 5.28: Waveform fits between 20° and 22° for the SG Terrane.	68
Figure 5.29: <i>P</i> -wave velocity model for the Songpan-Ganzi Terrane	69
Figure 5.30: Turning points beneath the Tarim Basin	70
Figure 5.31: Waveform fits for the southern Tarim Basin	71
Figure 5.32: <i>P</i> -wave velocity model for the Tarim Basin	72
Figure 6.1: Travel-time triplications for two different event depths	76
Figure 6.2: Collision model for the India-Eurasia convergence	77

List of Tables

Table 3.1: Summary of seismic networks used in this study	24
Table 4.1: Intermediate-depth events in southern Tibet from previous studies	37

Chapter 1: Introduction

Continent-continent collision is a major mountain-building process. For example, the Ural mountains were generated by the collision between the East European craton and the Siberian craton. The Tibetan Plateau, bounded by the Tarim Basin and North China block to the north and the Indian sub-continent to the south, is another example of mountain creation by the collision between the Indian Plate and the Eurasian Plate starting about 70–50 Ma ago (MOLNAR and TAPPONNIER, 1975; MOLNAR *et al.*, 1977; DEWEY *et al.*, 1988). It is the largest and highest plateau in the world, covering an area of more than 2.0 million square kilometers with an average elevation of more than 4,500 meters (Fig. 1.1).

Prior to the India-Eurasia collision, a series of continental fragments, which can be identified by several ophiolite zones in the Tibetan area, were added to the Eurasian Plate. From north to south, they are 1) the Songpan-Ganzi Terrane, 2) the Qiangtang Terrane, and 3) the Lhasa Terrane (DEWEY *et al.*, 1988). The Songpan-Ganzi Terrane accreted to Tarim-North China along the Kunlun-Qinling Suture during the late Permian. Then the Qiangtang Terrane was added to the Songpan-Ganzi Terrane along the Jinsha Suture during the late Triassic or early Jurassic, followed by the accretion of the Lhasa Terrane to the Qiangtang Terrane along the Bangong Suture during the late Jurassic. With the opening of the Indian Ocean, the Indian Plate moved northward and attached to the Lhasa Terrane along the Indus-Zangbo Suture during the Middle Eocene (DEWEY *et al.*, 1988; YIN and HARRISON, 2000).

As India continued to move northward into the interior of Eurasia, at least 1,400 km of N-S convergence took place (YIN and HARRISON, 2000; JOHNSON, 2002). For collisions involving at least one oceanic plate, the convergence is always accommodated by subduction of one of the oceanic plate(s). But if both are

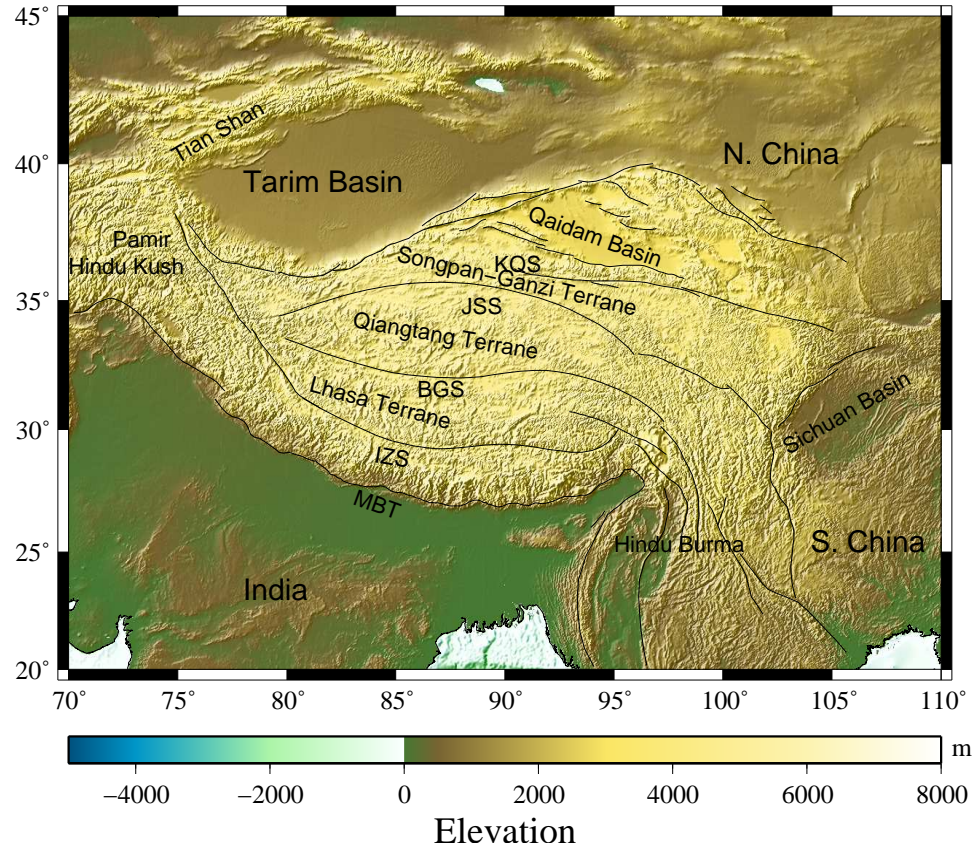


Figure 1.1: Tectonic map of the Tibetan Plateau and surrounding areas. Solid lines are major tectonic boundaries. MBT: the Main boundary thrust, IZS: the Indus-Zangbo Suture, BGS: the Bangong Suture, JSS: the Jingsha Suture, KQS: the Kunlun-Qinling Suture.

continental plates, it is still not clear how such large convergence is accommodated. Various collision models have been proposed to explain the convergence between the Indian Plate and Eurasian Plate and the uplifting of the Tibetan Plateau, including 1) underthrusting of the Indian Plate beneath the Eurasian Plate (ARGAND, 1924; BIRD, 1978; POWELL and CONAGHAN, 1973, 1975; BARAZANGI and NI, 1982), 2) injection of the Indian crustal material into the weak Tibetan lower crust (ZHAO and MORGAN, 1985, 1987), 3) distributed shortening and vertical thickening of the Eurasian lithosphere (DEWEY and BIRD, 1970; DEWEY and BURKE, 1973; ENGLAND and MCKENZIE, 1982; ENGLAND and HOUSEMAN, 1986; DEWEY *et al.*, 1988), 4) Subduction of the Indian Plate underneath the Eurasian Plate at the

Bangong Suture (OWENS and ZANDT, 1997), and 5) intracontinental subduction of south-dipping Eurasian mantle lithosphere underneath Tibet (FAN and WALLACE, 1991; WILLET and BEAUMONT, 1994; TAPPONNIER *et al.*, 2001) (Fig. 1.2).

Each of these models gives a unique crustal and mantle structure. The underthrusting model suggests a shield-like mantle lithosphere beneath the plateau, similar to the one beneath India. The Eurasian mantle lithosphere would be removed to accommodate the Indian Plate (Fig. 1.2A). Injection of the Indian crust into the Tibetan lower crust would require a weak lower crust beneath the Tibetan Plateau (Fig. 1.2B). In the distributed shortening model, in order to raise the northern plateau to reach an elevation of 5 km, the thickened mantle lithosphere beneath northern Tibet would need to be removed by a thermal instability or mantle convection (ENGLAND and HOUSEMAN, 1986; DEWEY *et al.*, 1988) (Fig. 1.2C). Subduction of the Indian Plate under the Bangong Suture would result in thicker crust in southern Tibet than in northern Tibet and a high velocity slab beneath the suture (Fig. 1.2D). Models of intracontinental subduction of the north-dipping Indian Plate and south-dipping Eurasian Plate beneath the Tibetan Plateau can be verified or eliminated by tests to detect such slabs in the upper mantle (Fig. 1.2E). Therefore, the structure beneath the plateau is key to understanding the evolution of this continent-continent convergence.

Much seismological research has been conducted to reveal the structure beneath the Tibetan Plateau, but most studies focus on the structures in the crust and uppermost mantle, which are shallower than 100 km (*e.g.* ZHU *et al.*, 1995; ZHU, 1998; ZHU and HELMBERGER, 1998; KOSAREV *et al.*, 1999; VERGNE *et al.*, 2002; GALVÉ *et al.*, 2002; SCHULTE-PELKUM *et al.*, 2005). Less attention has been given to deeper regions. In addition, current three-dimensional global tomographic images have low resolutions of 300–500 km (*e.g.* VAN DER VOO, 1999; REPLUMAZ *et al.*, 2004; LI *et al.*, 2006, 2008). High-resolution studies using receiver functions and

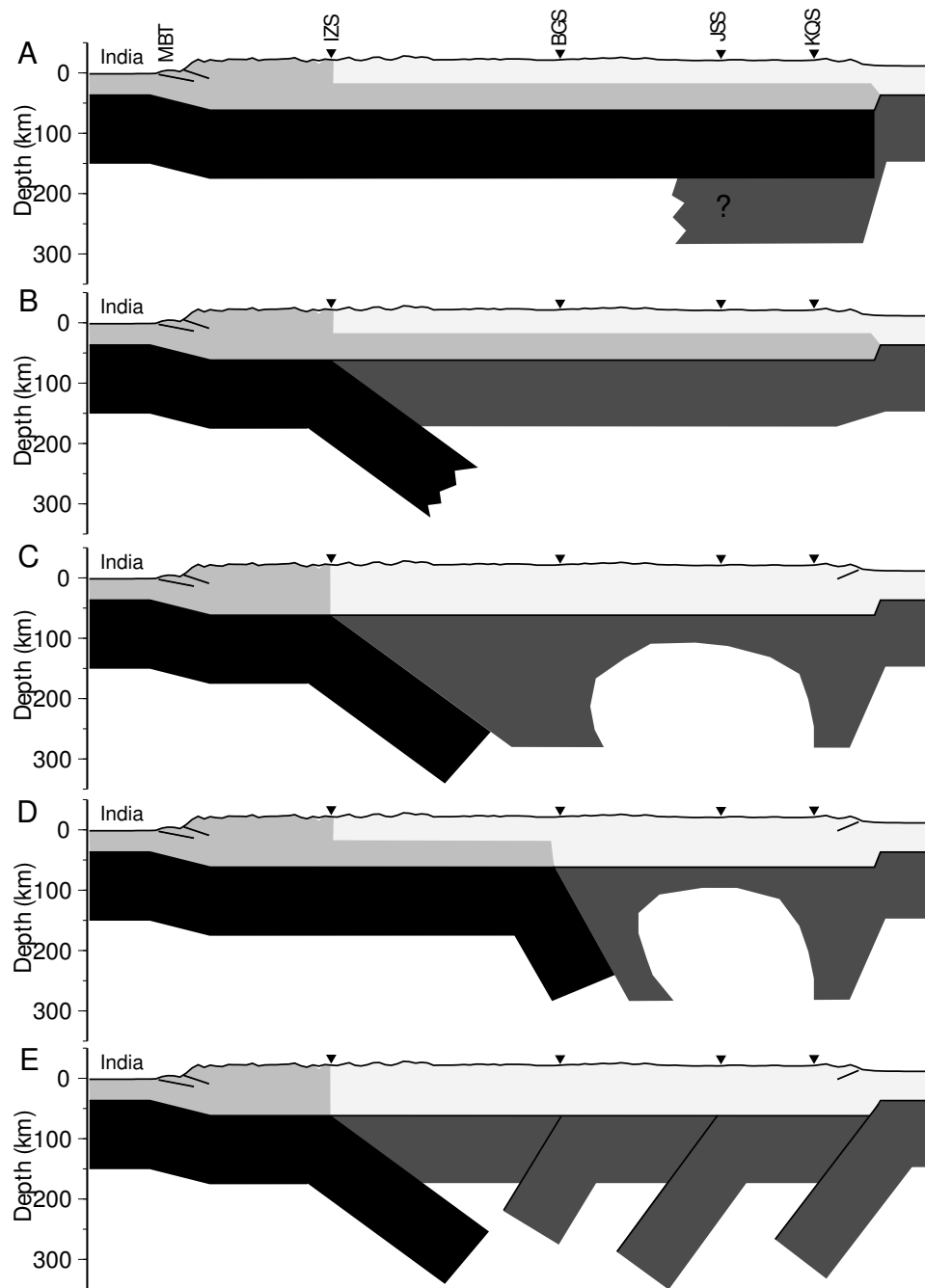


Figure 1.2: Five India-Eurasia collision models: (A) underthrusting, (B) injection, (C) distributed shortening, (D) subduction of the Indian Plate beneath the Bangong Suture, (E) intra-continental subductions.

travel-time tomography cover only small portions of the plateau (*e.g.* MCNAMARA *et al.*, 1997; KAO *et al.*, 2001; KIND *et al.*, 2002). Thus it is necessary to refine the model of the upper mantle velocity structure beneath the entire Tibetan Plateau. The purpose of this study is to obtain a high-resolution model of the three-dimensional upper mantle velocity structure beneath the Tibetan Plateau and surrounding areas.

In this dissertation, I will use waveforms in the distance range of 12° and 30° whose ray paths turn beneath the Tibetan Plateau in the upper mantle between 100 km and 850 km. The waveforms and differential travel times between different phases are very sensitive to upper mantle velocity structure. Such a study is now possible because large amounts of high-quality waveform data have accumulated over the last decade from the increasing number of seismic stations deployed in and around Tibet.

This dissertation starts in Chapter 2 with a review of previous seismic studies on the lithospheric and upper-mantle structures beneath the Tibetan Plateau. These studies include determinations of earthquake focal mechanisms and depths, studies of surface-wave dispersion inversions and tomography, waveform modeling, receiver function analyses, and recent global travel-time tomographic imaging. These studies have provided the first-order constraints on the seismic velocity structures of the Tibetan Plateau.

Chapter 3 focuses on the data and methods I used in this research. I describe waveform characteristics in the upper-mantle distance range as well as my modeling strategy. I then show the earthquake distribution in the study area and the criteria used to select earthquakes from the Harvard Centroid Moment Tensor (CMT) catalog. I show locations of broadband stations from both permanent seismic networks and temporary experiments in and around the Tibetan Plateau.

In order to model waveforms, accurate focal mechanisms, focal depths, and

source time functions are required. The CMT catalog provides preliminary estimations of focal mechanisms, centroid locations and half source durations. However, these routinely calculated parameters are not always reliable. I describe the verification of focal mechanisms in Chapter 4. A new technique to retrieve source time functions from teleseismic waveforms, by which focal depths are re-determined, is also introduced.

Detailed data analysis is presented in Chapter 5. The entire study area is divided into several regions. For each region, waveforms at upper mantle distances are modeled by fitting both amplitudes and differential travel times between different phases. Synthetic seismograms are calculated with generalized ray theory.

This dissertation ends in Chapter 6 with an evaluation of my upper-mantle velocity models and their implications for the tectonic history of India-Eurasia collisions and the formation of the Tibetan Plateau.

Chapter 2: Review of Literature on the Lithospheric and Upper-mantle Structures beneath the Tibetan Plateau

The Tibetan Plateau is a natural laboratory for the study of continent-continent collision. It has attracted the interest of seismologists for several decades. In this chapter, I will review some of the seismological discoveries on the lithospheric and upper-mantle structure beneath the Tibetan Plateau.

Before 1980, exploration of the deep structure of the plateau relied on a few analog seismic stations outside Tibet. Most work used body wave travel times (NI and BARAZANGI, 1983) and surface wave dispersions (*e.g.* GUPTA and NARAIN, 1967; CHEN and MOLNAR, 1975; CHUN and YOSHII, 1977; JOBERT *et al.*, 1985), which helped determine the first-order structural parameters such as average thicknesses and velocities of the crust and mantle lid. In the last two decades, however, a number of international collaborative experiments in and around the Tibetan Plateau have used modern digital seismic instruments. As a result, large amounts of seismic data directly sampled from the plateau have been accumulated. Analyses of these data sets in recent years have greatly advanced our knowledge about the structure of the plateau.

2.1 Earthquake depth and focal mechanism studies

Studying earthquake focal mechanisms and depths provides important information about mechanical properties and stress orientation in the lithosphere. It has been found that earthquakes far from subduction zones in continents are usually concentrated in the upper 20 km of the crust and the uppermost mantle. The lower crust is weak and almost aseismic. Based on these characteristics, CHEN and MOLNAR (1983) proposed that the continental lithosphere consisted of a brittle seismic upper crust, a ductile aseismic lower crust, and a brittle seismically active

uppermost mantle. The brittle-ductile transition in the crust is a result of the thermal gradients in the earth. The second transition between the crust and upper mantle is thought to relate to the mineral changes.

Shallow earthquakes in the Tibetan Plateau are concentrated in the top 15 km of the crust (CHEN and MOLNAR, 1983). Focal mechanisms suggest thrust faulting for earthquakes in southern and northern Tibet and strike-slip faulting for earthquakes in central Tibet. Principal compressive directions are in the N-S direction (MOLNAR *et al.*, 1973; MOLNAR and LYON-CAEN, 1989). These agree with the direction of India-Eurasia collision.

Intermediate-depth earthquakes with focal depths between 70 km and 100 km, thought to occur in the uppermost mantle, were found by several seismologists in the Himalayas and southern Tibet (CHEN and MOLNAR, 1983; ZHU and HELMBERGER, 1996; CHEN and YANG, 2004; MONSALVE *et al.*, 2006). These events displayed strike-slip focal mechanisms with some normal-fault component. These mechanisms were similar to faulting indicated by earthquakes in the top 15 km. The principal P and T axes of the fault-plane solutions showed NS compression and EW extension, which was consistent with the stress field produced by the collision of the Indian Plate (ZHU and HELMBERGER, 1996). This observation implied that these intermediate-depth earthquakes were not related to subduction of the Indian Plate in southern Tibet (CHEN and YANG, 2004). A bimodal distribution of focal depths was thought to explain this intermediate-depth seismogenic region in the continental lithosphere.

However, researchers who studied focal depth distributions in the Tian Shan and northeast Indian Plateau found no evidence to support this bimodal distribution (MAGGI *et al.*, 2000b; MITRA *et al.*, 2005; PRIESTLEY *et al.*, 2008). They suggested that these intermediate-depth earthquakes actually occurred in the lower crust or in a oceanic lithospheric slab, not in the uppermost mantle. A

seismogenic crustal layer with variable thickness (T_s) from 10 km to 40 km was proposed. T_s variations were related to temperature and the presence or absence of small amounts of water, and correlated with the variations in the effective elastic thickness (T_e) (MAGGI *et al.*, 2000a).

2.2 Modeling waveforms at upper-mantle distances

Waveforms in the distance range of 10° to 30° are very sensitive to the velocity structures of the upper mantle. By fitting both arrival times and amplitudes of P -wave waveforms at distances of 9° – 26° , GIVEN and HELMBERGER (1980) revealed a low velocity zone beneath northwestern Eurasia between depths of 150 km and 200 km. They found two velocity increases of 4.5% and 4% at depths of 420 km and 675 km, respectively. The velocity gradient in the transition zone was large compared to those of models in other areas. BECKERS *et al.* (1994) refined models of the upper mantle structure beneath the Tibetan Plateau by fitting P and PP waveforms. In their model, P_n velocities were as low as 8.0 km/s for the northern fold belt and varied from 8.15 to 8.25 km/s for the plateau. A 30-45 km thick lid lay above a low velocity zone with low velocities extending below 200 km depth.

SH waves at the upper-mantle distances of 10° – 30° were used to determine velocity structure in the upper mantle beneath the Indian Shield and the Tibetan Plateau. LYON-CAEN (1986) found that shear velocities in the uppermost mantle beneath these two areas were close to 4.7 km/s. The Indian Shield had a thicker high-velocity lid than the Tibetan Plateau. The velocity between 40 km and 250 km beneath the Indian Shield was between 4.58 km/s and 4.68 km/s, while the velocity between 70 km and 250 km beneath central and northern Tibet was at least 4% slower than that beneath the Indian Shield. No velocity variation was reported below 250 km. This model had a thinner lid and shallower transition zone than the model from BECKERS *et al.* (1994). ZHAO *et al.* (1991) constructed a lithospheric

and upper-mantle velocity model TIP beneath the Tibetan Plateau by modeling S and SS waveforms turning beneath the plateau. The upper-mantle structure beneath the entire plateau was shield-like below 200 km. The lithosphere velocity was slower than that from LYON-CAEN (1986), and no distinct lid was observed (Fig. 2.1).

CHEN and TSENG (2007) modeled P -wave triplication beneath central Tibet and northern India. P -wave velocity jump across the 660 discontinuity beneath central Tibet was remarkably small with a 3.0% velocity jump at about 675 km, while P velocity jumped about 4.4% beneath northern India. The lateral variation of the P -velocity jump between Tibet and India exceeded the known variation of P waves in the lower mantle by a factor of four. The researchers thought that this lateral variation was caused by a detached Indian lithosphere sitting on top of the 660 discontinuity (CHEN and TSENG, 2007).

2.3 Surface wave dispersion inversion and tomography

Surface waves of different frequencies travel at different speeds. Higher-frequency waves in the shallow structure of the earth thus travel slower. This is called surface-wave dispersion, which can be used to determine velocity structure. CHEN and MOLNAR (1975) found a 2.5–7.0 km thick sedimentary layer in the Tibetan area, by using the dispersion of Rayleigh waves. The crustal thickness beneath the Tibetan Plateau was found to be about 70 km (GUPTA and NARAIN, 1967; CHUN and YOSHII, 1977; JOBERT *et al.*, 1985). The lower crust north of the Indus-Zangbo Suture between depths of 40 km and 70 km has a low S -wave velocity, which indicates partial melting (COTTE *et al.*, 1999; RAPINE *et al.*, 2003). RAPINE *et al.* (2003) showed that there was a low-velocity middle-crust layer for southern Tibet. It was thought to be the result of H_2O -saturated melting of the interplate shear zone between the underthrusting Indian crust and the overflowing Eurasian crust. A

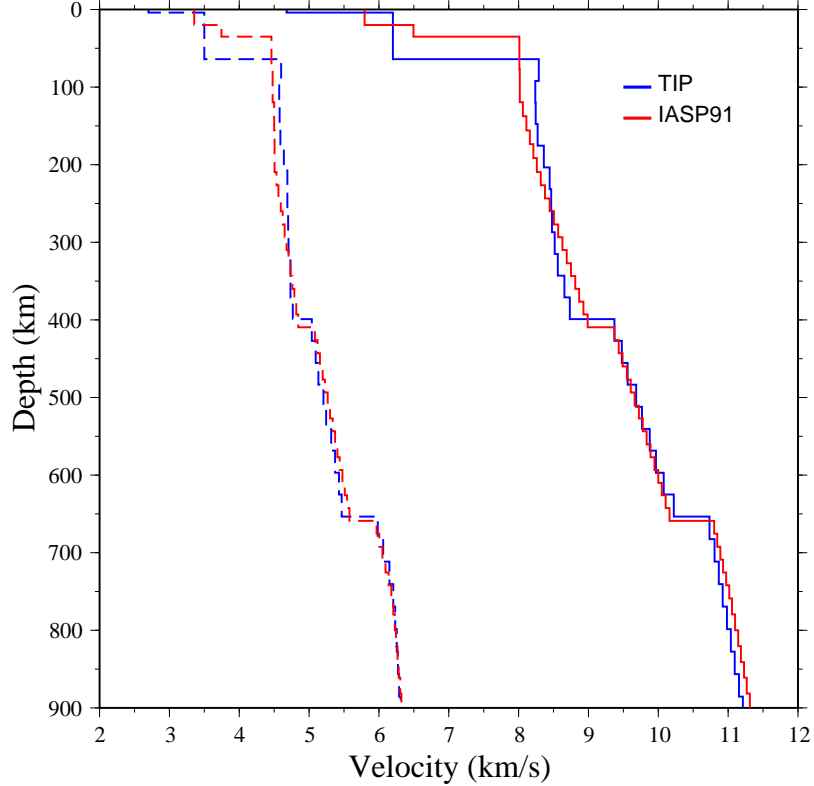


Figure 2.1: Comparison of the TIP model with global average velocity model IASP91. Dashed lines are S -wave velocities and solid lines represent P -wave velocities.

widespread low shear-velocity layer was mapped between the depths of 115 km and 185 km beneath the central and northeast plateau by measuring the fundamental Love and Rayleigh wave phase velocities in the period range of 32–200 sec (CURTIS and WOODHOUSE, 1997).

Rayleigh wave tomography showed that the S_n velocity between the Bangong Suture and the Kunlun Fault was abnormally slow, indicating partial melting in the lower crust and uppermost mantle (HUANG *et al.*, 2003; YAO *et al.*, 2005). JOBERT *et al.* (1985) found a high-velocity lid in the mantle at depths of 100–150 km beneath the Tibetan Plateau. A high-velocity structure with a thickness of about 160 km, interpreted as the subducted Indian lithosphere, plunged northward from 100 km beneath southern Tibet to 150 km beneath the Indus-Zangbo Suture. Another high-velocity anomaly lay under the Qiangtang Terrane between 150 km

and 250 km. It was thought to be the delaminated Eurasian lithosphere (HUANG *et al.*, 2003).

Low group velocities between 20 and 100 sec dominate the Tibet area (WU *et al.*, 1997; RITZWOLLER and LEVSHIN, 1998; CURTIS *et al.*, 1998; VILLASEÑOR *et al.*, 2001), especially in central and north Tibet. The presence of this low-velocity region suggests that the high-velocity Indian lithosphere has not thrusted beneath the Tibetan Plateau. The crustal thickening is the result of the north-south shortening of southern Eurasia's crust, which causes the upper-mantle material under Tibet to flow east when it is blocked by the thick Tarim lithosphere in the west (MOLNAR *et al.*, 1993; VILLASEÑOR *et al.*, 2001; XU *et al.*, 2002).

2.4 Receiver function analysis

The receiver function technique is a method of studying velocity structure in the earth. It is mostly sensitive to *S*-wave velocity discontinuities. By using the receiver function technique along a north-south profile in eastern Tibet, KOSAREV *et al.* (1999), found that the Indian lithospheric mantle was subducting underneath the Tibetan Plateau from 50 km north of the Indus-Zangbo Suture at 80 km to 200 km beneath the Bangong Suture, and that the Eurasian lithosphere mantle was thrusting under the northern margin of the plateau. A “bright spot” was reported beneath the Qiangtang Terrane where these two lithospheres met. These findings were later confirmed by KIND *et al.* (2002) and KUMAR *et al.* (2006).

The same features were reported by KAO *et al.* (2001), WITTLINGER *et al.* (2004), and KUMAR *et al.* (2005) for western Tibet near the Tarim Basin. The lithosphere beneath the Tarim Basin dipped 45°S beneath northwestern Tibet to a 300 km depth. The agreement between these different works indicates that the crust and upper mantle from north and south Tibet interpenetrated each other and that the plateau is formed by a north-dipping subducted Indian continental lithosphere

in the south and a south-dipping Eurasian lithosphere in the north (KUMAR *et al.*, 2006).

YUAN *et al.* (1997) found that both the 410 and 660 discontinuities beneath southern Tibet were at the same depths as the global average. KIND *et al.* (2002) further imaged both discontinuities beneath northern Tibet. They were slightly deeper than those of southern Tibet, indicating that the temperature above the 410 discontinuity was 300°C hotter in the north. The separation of the 410 and 660 discontinuities remained constant for both northern and southern Tibet, which implied that there was no slab penetrating into the mantle (KIND *et al.*, 2002).

2.5 Travel-time tomography

P_n and S_n waves are P and S waves refracted along the Moho discontinuity that marks the boundary between crust and mantle. These waves sample the uppermost mantle. P_n -wave travel-time tomography beneath the Tibetan Plateau showed that average P_n velocities of the northern plateau were 3% slower than those of the southern plateau. P_n in the Qiangtang Terrane is slow relative to both the plateau south of the Bangong Suture and Tarim Basin north of the plateau (ZHAO and XIE, 1993; MCNAMARA *et al.*, 1997; RITZWOLLER *et al.*, 2002; SUN and TOKSÖZ, 2006; HEARN *et al.*, 2004; LIANG *et al.*, 2004; LIANG and SONG, 2006; PEI *et al.*, 2007). S_n -wave propagation in this region is inefficient, which implies that the uppermost mantle beneath the Qiangtang Terrane is fluid-like and indicates partial melting within the uppermost mantle beneath the northern Tibetan Plateau (MCNAMARA *et al.*, 1997; RITZWOLLER *et al.*, 2002; PEI *et al.*, 2007; RODGERS and SCHWARTZ, 1998). P_n -wave velocities in low P_n -velocity regions beneath the Tibetan Plateau are anisotropic with fast directions perpendicular to the surface movement from GPS measurements. This anisotropy pattern indicates that the upper mantle beneath the Tibetan Plateau is extruded to the east (LIANG and SONG, 2006; PEI *et al.*, 2007).

TILMANN *et al.* (2003) imaged a near-vertical high-velocity zone from 100 km to 400 km depth south of the Bangong Suture by using data recorded by the INDEPTH III and the 1991-1992 Sino-US seismic experiments. This high-velocity zone was interpreted as the downwelling Indian mantle lithosphere, which was verified by receiver function studies (KOSAREV *et al.*, 1999; KIND *et al.*, 2002). It accounted for most of the shortening in the mantle since the India-Eurasia collision about 50 Ma ago. In order to balance the deficit of asthenosphere induced by the downwelling lithospheric mantle, TILMANN *et al.* (2003) proposed a convection cell beneath the Eurasian lithospheric mantle between the Bangong Suture and Kunlun-Qinling Suture. The convection cell was superimposed on the eastward extrusion and could explain the presence of the warm mantle beneath north-central Tibet. According to this hypothesis, the thickening of the Tibetan Plateau is the result of continental subduction of the Indian lithospheric mantle.

However, REPLUMAZ *et al.* (2004) and LI *et al.* (2006) pointed out that the Tibetan Plateau was thickened by the subduction of Eurasian mantle and inferred from their tomographic results that high-velocity anomaly underlay only the southwestern margin of the Tibetan Plateau. Other results from REPLUMAZ *et al.* (2004) also showed a continuous S-shaped high-velocity anomaly south of the Indus-Zangbo Suture down to the lower mantle. They interpreted the flat portion in the middle at the depth of 1,000 km as the marker of the India-Eurasia collision. The shallower south-dipping part, which impinged India after the collision began, was the northwards sweep of the active margin of Asia. On the contrary, VAN DER VOO (1999) found that the S-shaped high-velocity anomaly was not continuous. Four separate zones could be identified, which were thought to be the remnants of the Tethyan subducted slabs.

ZHOU and MURPHY (2005) found a slab-shaped high-velocity seismic anomaly beneath the entire Tibetan Plateau and interpreted it as the subducted Indian

lithospheric mantle. A wedge-shaped slow-velocity seismic anomaly was interpreted as the asthenospheric layer. Based on this discovery, they suggested that the Indian lithospheric slab had subducted near-horizontally beneath the entire Tibetan Plateau to depths of 165–260 km.

HUANG and ZHAO (2006) showed that the Indian Plate was separated into the upper crust and the upper-mantle lid during its subduction underneath the Tibetan Plateau. The upper crust caused multilayer crustal subduction under the Himalayas and southern Tibet during its northward advancing. The upper-mantle lid subducted to the upper mantle beneath the Tibetan Plateau at a depth of 200–300 km with a horizontal distance of 500 km.

In summary, previous seismic studies on the Tibetan Plateau either have low resolutions, or cover small portions of the plateau. Triplicated waveform studies treated the Tibetan Plateau as a whole, which is not appropriate as shown by the tomographic results. Surface-wave dispersion and travel-time tomography have lateral resolutions of several degrees. Because of the inaccuracy of earthquake origin time and model parameterization, travel-time tomographic images tend to be blurred, while receiver function technique can give better resolution. However, receiver functions are sensitive to S -wave velocity jump and can not give a detailed structure of velocity change. Another limitation of this technique is that receiver functions can only reveal the structure beneath each station within 20 km. Current station configuration can not provide enough coverage on the Tibetan Plateau. Thus, it is necessary to obtain a high-resolution model of the upper-mantle velocity structure beneath the entire Tibetan Plateau.

Chapter 3: Method and Data

Modeling waveforms at the upper-mantle distances is a powerful tool for studying velocity structures in the upper mantle (*e.g.* HELMBERGER, 1973; GIVEN and HELMBERGER, 1980; GRAND and HELMBERGER, 1985; ZHAO *et al.*, 1991; GARNERO *et al.*, 1992; SONG *et al.*, 2004). In this chapter, I will describe my strategy to determine velocity structures using broadband waveform data recorded by stations around Tibet.

3.1 Determine velocity structure using waveforms at upper-mantle distances

As velocity increases with depth, a seismic wave turns at certain depths before being recorded by a receiver on the surface. If there is a rapid velocity increase or velocity jump, three seismic rays can reach at the same station: 1) a ray turning above the discontinuity, 2) a ray reflected by the discontinuity, and 3) a ray turning below the discontinuity (Fig. 3.1). Consequently, three phases appear on the seismogram. This phenomenon is referred as triplication. In the earth, there are two major global velocity discontinuities in the upper mantle at depths of 410 km and 660 km. Both are due to mineral phase changes (BINA, 1991; SHEARER, 2000). Thus, two sets of triplication exist. For the IASP91 velocity model, the 410 discontinuity's triplication appears from 12° to 21° . The AB and CD branches cross at 18° . The triplication of the 660 discontinuity begins at 17° and ends at 28° . The CD and EF branches meet at around 23° (Fig. 3.1).

Upper-mantle triplications provide a unique way to determine velocity structure above the 410 discontinuity. As shown in Fig. 3.1, the seismic wave of the AB branch travels nearly horizontally near its turning depth and is mostly sensitive to the velocity at this depth. The seismic waves of other branches turn in the

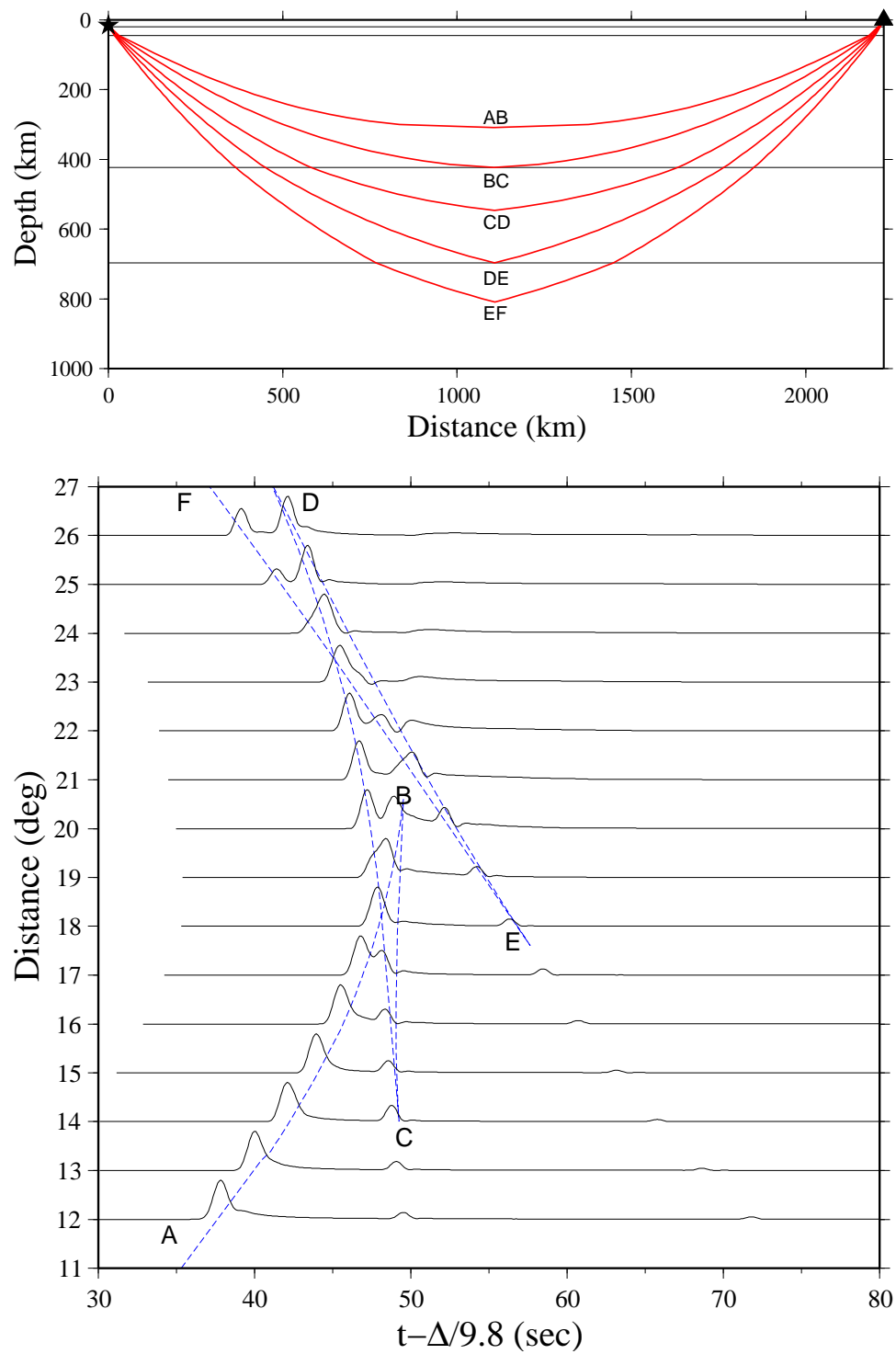


Figure 3.1: Top panel shows seismic ray paths to a station at a distance of 20° . The bottom panel shows a record section of P waves in the distance range of 12° and 26° . Blue dashed lines represent arrival times of different branches associated with the 410 and 660 discontinuities.

transition zone and the lower mantle, where velocity structures are relatively more homogeneous laterally. Their arrivals can serve as reference time marks. Because all the rays share similar paths near the source and station, the differential travel times between the AB branch and the deeper branches are less influenced by the earthquake origin-time error and shallow velocity structural variations.

To demonstrate this, I placed a high-velocity anomaly between 200 km and 250 km in the velocity model used in Fig. 3.1. The P -wave profile of the perturbed velocity model is shown in Fig. 3.2. It shows that this high-velocity anomaly only changes the separations between AB and BC branches in the distance range of 16° to 18° , with the largest separation change at about 17° . Waveforms at other distances are almost identical.

Since the differential arrival times between the AB branch and other branches are used, there is a trade-off between the velocity in the shallow upper-mantle and the deep part. For instance, a large separation between the AB and BC branches could also be explained by a low-velocity anomaly just above the 410 discontinuity or a deeper 410 discontinuity. Fig. 3.3 shows this trade-off by two sets of triplicated waveforms. A deeper 410 discontinuity (at 426 km) can fit the large separation in waveforms at distances between 16° and 18° . In this situation, it cannot be decided whether these waveforms are produced by a deeper 410 discontinuity or by high velocities in the top upper-mantle.

To reduce the trade-off in the waveform modeling, my strategy is to determine velocities in the deep part first by modeling waveforms at large distances, and then to move upward to the shallow depths. The advantage of this modeling technique is that it can reduce the trade-off and eliminate the effect of large velocity uncertainties of the shallow structures, especially the crust. I will use the phase with deep turning depths as the reference phase, on which the synthetic and the observed seismograms are aligned. Velocities near the turning depth of the shallow

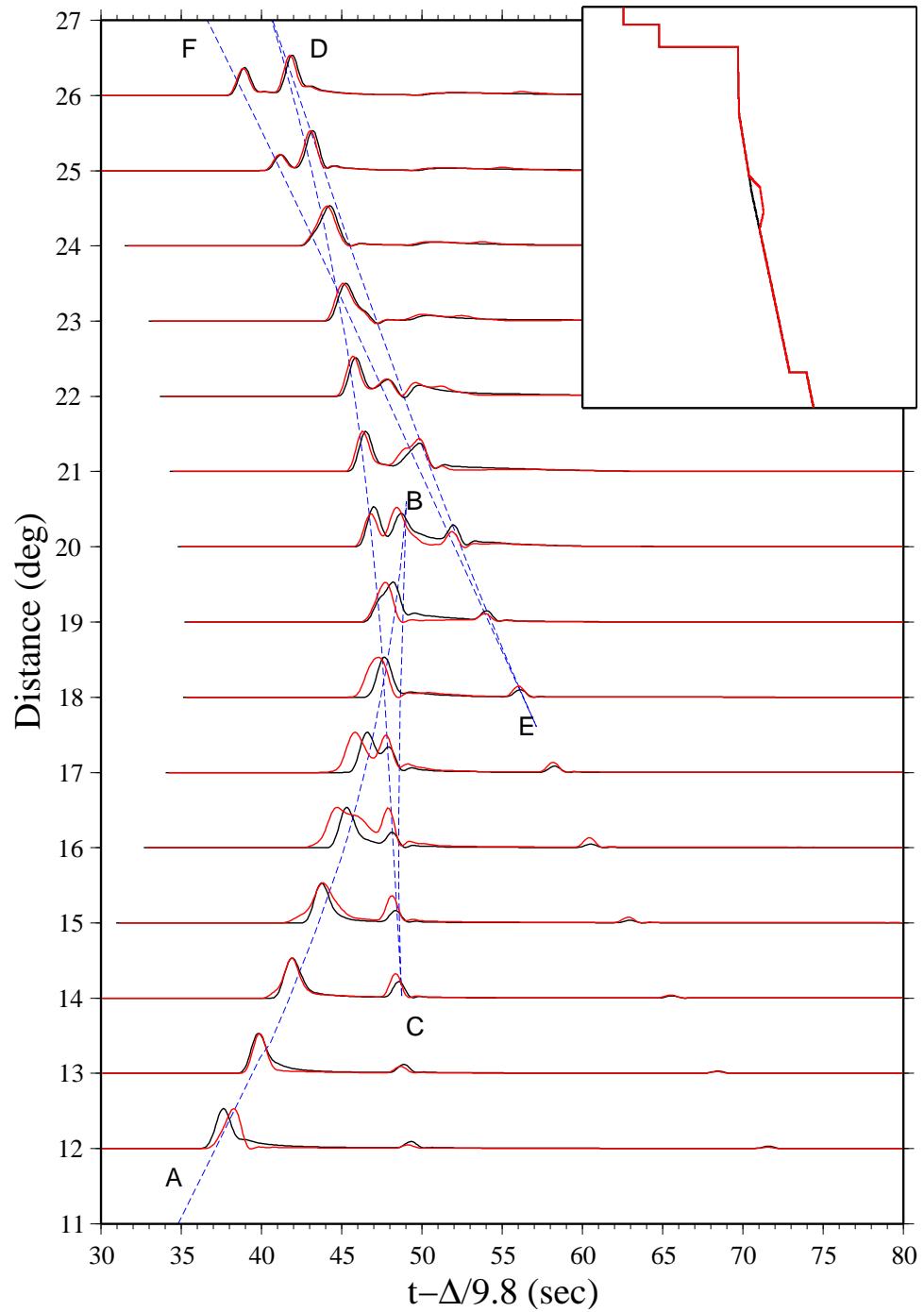


Figure 3.2: *P*-wave profiles of two different upper-mantle velocity models (shown in the insert box). The red-color seismograms correspond to the model with a high-velocity anomaly between 200 km and 250 km.

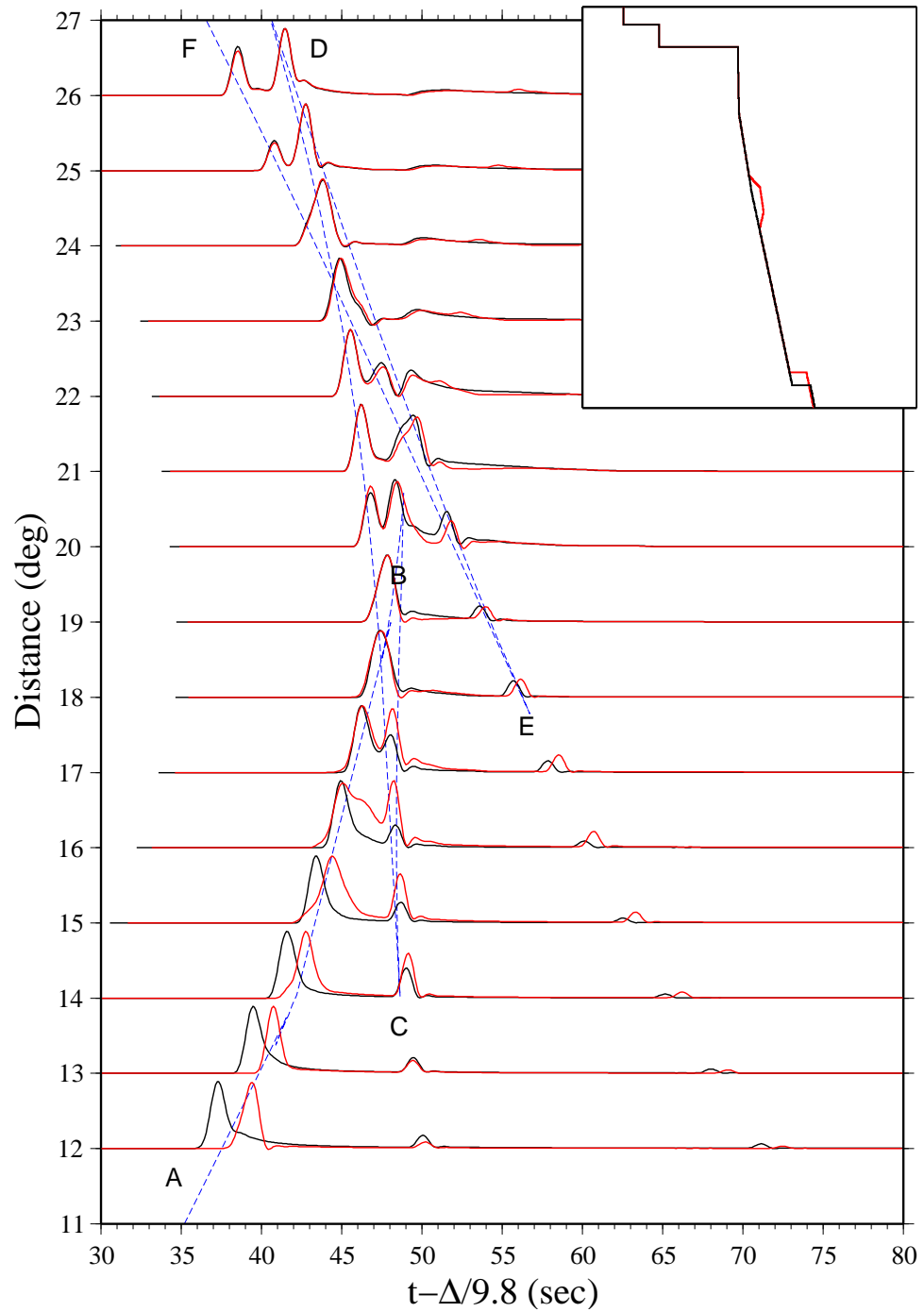


Figure 3.3: The red-color model and P -wave profile are the same as in Fig. 3.2. The black-color profile corresponds to a model without the high-velocity anomaly but with a deeper 410 discontinuity.

phase will be adjusted to fit both the arrival time and amplitude of the shallow phase through trial-and-error.

3.2 Data

3.2.1 Event selection and station locations

In order to study the upper-mantle velocity structures above the 410 discontinuity, seismograms at epicentral distances between 10° and 30° are needed. To ensure that turning points are located in the study area, I restricted earthquakes to those with distances less than 30° from the center of the Tibetan Plateau (85°E , 33°N , Fig. 3.4). Using the Preliminary Determinations of Earthquakes (PDE) catalog, I found 1,715 earthquakes around the Tibetan Plateau between January 1990 and February 2005 with magnitudes larger than 5.0 (Fig. 3.4). 929 of them have the Harvard CMT solutions. Most the events are clustered in four regions: Sumatra, Hindu Burma, Tibetan Plateau, and Pamir-Hindu Kush.

The 1,715 earthquakes were recorded by more than 300 permanent and temporary broadband seismic stations in and around the Tibetan Plateau. Permanent stations include about 48 stations from the Chinese National Digital Seismic Network (CNDSN, network code CD) (LIU *et al.*, 2007), 13 stations from the Kirghiz Telemetered Network (KNET, KN) (MELLORS, 2005; MARTYNOV *et al.*, 1999), 13 stations from the Kazakhstan Network (Kaznet, KZ) (KOPNICHEV *et al.*, 2001), and several Global Seismographic Network (GSN) stations (Fig. 3.4).

Since 1991, many seismic recording experiments have been conducted around Tibet, providing excellent station coverage for the study area (Fig. 3.5). These temporary stations were deployed during several PASSCAL-type experiments: the 1991-92 Sino-US PASSCAL experiment (XC) (OWENS *et al.*, 1993), the 1994 INDEPTH II and 1997-99 INDEPTH III experiments (XR) (ZHAO *et al.*, 1993; NELSON *et al.*, 1996; ALSDORF *et al.*, 1998; ZHAO, 2001), the 1995-96 Nanga

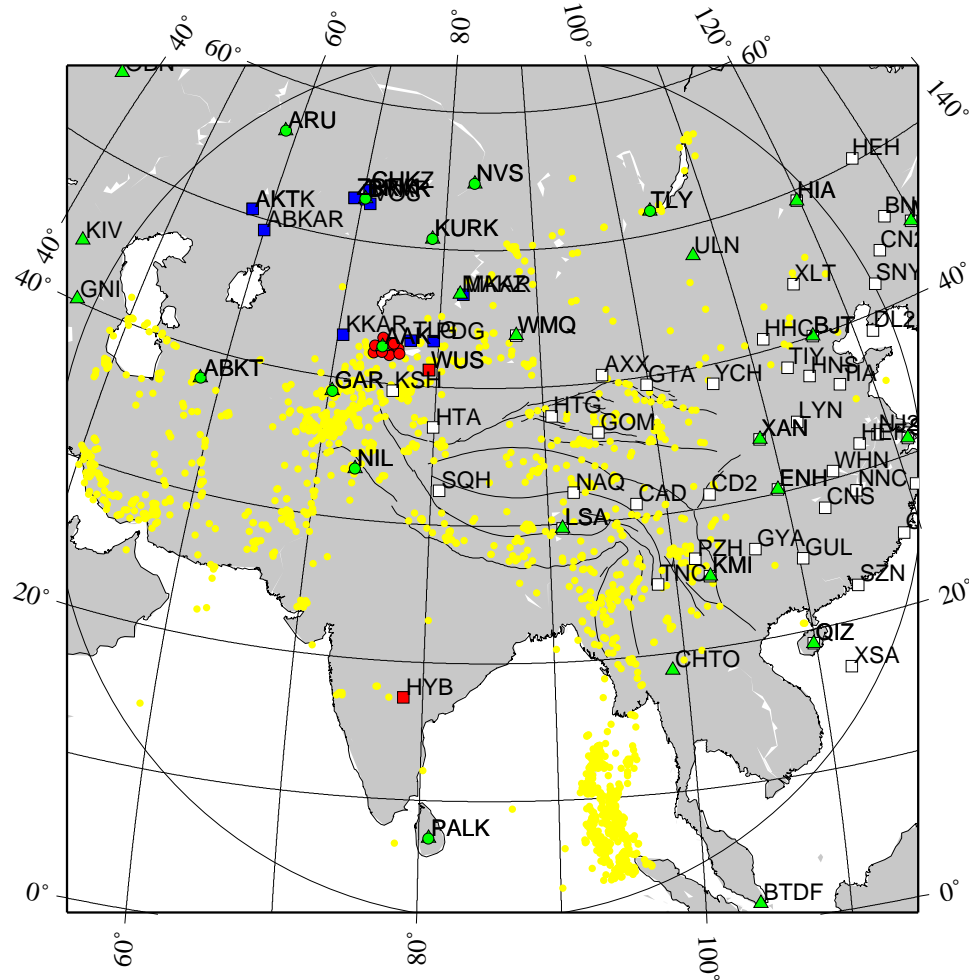


Figure 3.4: Earthquakes with $M_w \geq 5$ from January 1990 to February 2005 with distances less than 30° from the center of the Tibetan Plateau are plotted as yellow dots. Other symbols represent permanent seismic stations around the Tibetan Plateau, including the Chinese National Digital Seismic Network (white squares), the Kirghiz Telemetered Network (red dots), GEOSCOPE stations (red squares), IRIS/IDA network (green dots), the Kazakhstan Network (blue squares), and the Global Seismographic Network stations (green triangles).

Parbat Pakistan experiment (XG) (MELTZER *et al.*, 1996, 2001), the 1997-2001 Tian Shan Continental Dynamics experiment (GHENGIS, XW) (ROECKER, 1999), the 1998 Southwestern Tarim experiment (XM) (KAO *et al.*, 2001), the 2001-02 Himalayan Nepal Tibet Seismic experiment (HIMNT, YL) (DE LA TORRE and SHEEHAN, 2005; MONSALVE *et al.*, 2006), the 2002-03 Bhutan Pilot experiment (XA) (VELASCO *et al.*, 2002, 2007), the 2003-04 Namche Barwa Tibet experiment

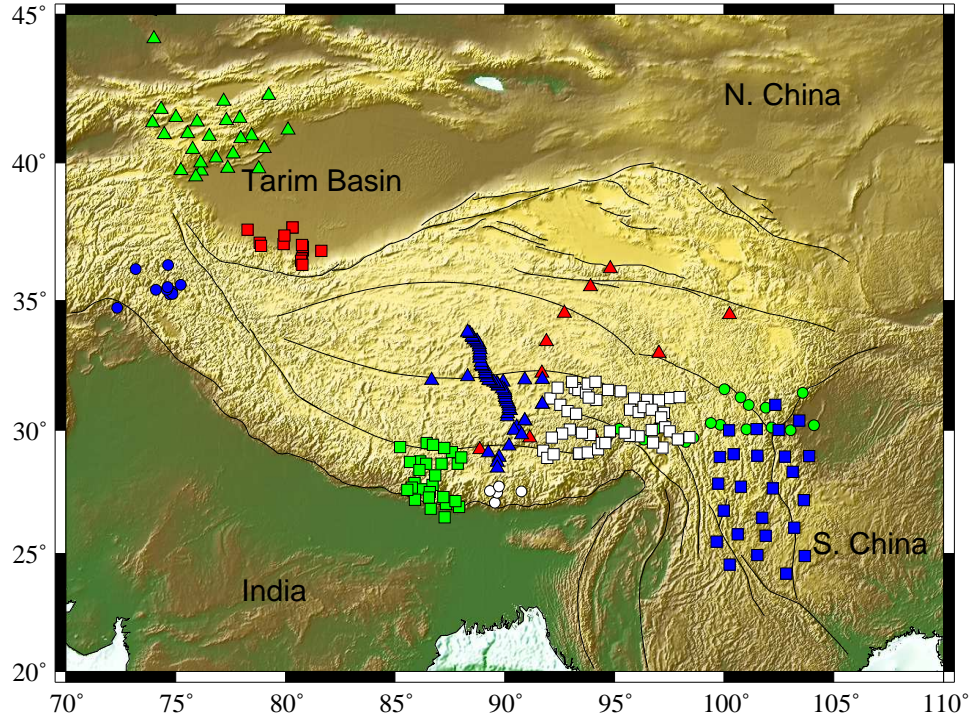


Figure 3.5: Station locations of seismic recording experiments used in this study: the 1991-92 Sino-US PASSCAL experiment (red triangles), the 1994 INDEPTH II and 1997-99 INDEPTH III experiment (blue triangles), the 1995-96 Nanga Parbat Pakistan experiment (blue dots), the 1997-2001 Tian Shan Continental Dynamics experiment (green triangles), the 1998 Southwestern Tarim experiment (red squares), the 2001-02 Himalayan Nepal Tibet Seismic experiment (green squares), the 2002-03 Bhutan Pilot experiment (white dots), the 2003-04 Namche Barwa Tibet experiment (white squares), the 2003-04 MIT-China seismic experiment (blue squares), and the 2004-06 Sichuan Tibet experiment (green dots).

(XE) (SOL *et al.*, 2007), the 2003-04 MIT-China seismic experiment (YA) (VAN DER HILST *et al.*, 2005), and the 2004-06 Sichuan Tibet experiment (XS) (WANG *et al.*, 2006). Most of the temporary stations were deployed around eastern and southern Tibet (Fig. 3.5). Table 3.1 gives a summary of instrument types and durations for all the permanent and temporary seismic stations used in this study.

3.2.2 Preliminary data processing

Waveforms recorded by more than 300 broadband stations were acquired from the IRIS Data Management Center. I used a time window of 30 sec before and

Table 3.1: Summary of seismic networks used in this study

Network	BB stations	Sensors	From	To
CD	48	JCZ-1, CTS-1, STS-2	–	–
KN	13	STS-2	–	–
KZ	13	CMG-3, CMG-40T, STS-2	–	–
XC	11	CMG-3ESP, STS-2	07/1991	07/1992
XR	30	STS-2	05/1994	09/1994
XR	60	STS-2	07/1998	12/1999
XM	14	STS-2	05/1996	09/1996
XW	28	STS-2	10/1997	12/2001
XS	12	STS-2	08/1998	09/1999
YL	28	STS-2	09/2001	04/2003
XG	5	Guralp-40T, STS-2	01/2002	03/2003
XE	51	STS-2	07/2003	12/2004
YA	25	STS-2	09/2003	09/2004
XA	24	STS-2	06/2004	03/2006

60 sec after the predicted P -wave arrival times to isolate the desired P waveforms from the raw data. In order to verify focal mechanisms and depths of the 1,715 earthquakes, I also downloaded teleseismic P and S waveforms recorded by the GSN network from IRIS.

After all waveform data from the 1,715 earthquakes were obtained, I removed instrument responses from each waveform, re-sampled the trace with a sampling rate of 10 points per second, and filtered using a bandpass filter with corner frequencies of 0.02 Hz and 1.0 Hz. P -wave arrival times were picked for each event. To control the waveform quality, I visually inspected each waveform and discarded bad traces. In total, I found 21,407 seismograms in the distance range between 10° and 30° .

Chapter 4: Earthquake Source Time Functions and Focal Depths

4.1 Introduction

Each seismogram is a convolution of the earthquake source time function and the impulse response of earth. The latter is usually expressed in terms of Green's functions. For small earthquakes, seismologists often use a triangle or trapezoid function to approximate the source time function. But for large events, the source time functions are much more complicated and need to be determined by observations.

In order to separate the source and propagation effects, many deconvolution techniques have been developed. One is called the homomorphic deconvolution and uses a linear operator to transform the convolution in the time domain to addition in the quefreny domain (ULRYCH, 1971). The source time function is the low-pass filtered result of the complex cepstrum. One of the difficulties of this technique is the phase unwrapping in the presence of additive noise in the seismogram (JIN and ROGERS, 1983). Another technique uses the empirical Green's function. It uses seismograms from aftershocks, which have similar focal mechanisms and locations as the main shock, as the impulse responses of the earth. Deconvolution of the main shock seismograms with the empirical Green's functions removes the effects of ray path and site response (DREGER, 1994). This approach requires that the corner frequency of aftershock be much larger than that of the main shock. Usually, the magnitude of the aftershock should be two orders of magnitude smaller than the magnitude of the main shock. Since the aftershock seismograms have much smaller amplitudes, they are easily affected by noise. BRUDZINSKI and CHEN (2000) developed a method to use teleseismic P waveforms in similar azimuths as the effective source time function. Because of the depth phases, their method only works for deep events. Otherwise the effective source time function is contaminated

by the depth phases.

I developed a new technique to estimate the source time function and to determine earthquake focal depth simultaneously using teleseismic waveforms.

4.2 Procedure

4.2.1 Verify CMT solutions and revise focal depths

The centroid coordinates and moment tensors (CMT) of earthquakes worldwide with magnitudes larger than 5.0 are routinely estimated by minimizing the misfits between observed and synthetic body and/or surface waves at very long periods (longer than 45 sec for body waves, 135 sec for surface waves). These solutions are compiled in the Harvard CMT catalog (DZIEWONSKI *et al.*, 1981; EKSTRÖM and DZIEWONSKI, 1985). Because long period waves are not sensitive to event depths, the CMT depths are not very reliable. In addition, the centroid depths in the crust are restricted to at least 15 km in order to minimize the instabilities of the moment tensor inversion at very shallow depths (ARVIDSSON and EKSTRÖM, 1998). Therefore, my first step is re-estimating event depths.

At teleseismic distances (30° – 90°), seismic rays travel mostly in the lower mantle and are free of the complexities caused by reflection or refraction in the upper mantle and near the core-mantle boundary. The P -wave seismograms consist of the direct P wave and the depth phases pP and sP . The differential travel times of P - pP and P - sP are controlled by the event depth and can be used to estimate the earthquake focal depth.

Recordings from the GSN stations with distances between 30° and 90° were used for the analysis. I calculated synthetic seismograms with a global average velocity model IASP91 (KENNETT and ENGD AHL, 1991) using the generalized ray theory (HELMBERGER, 1983). The source time functions used in this step are triangle or trapezoid functions. By comparing synthetic seismograms with the

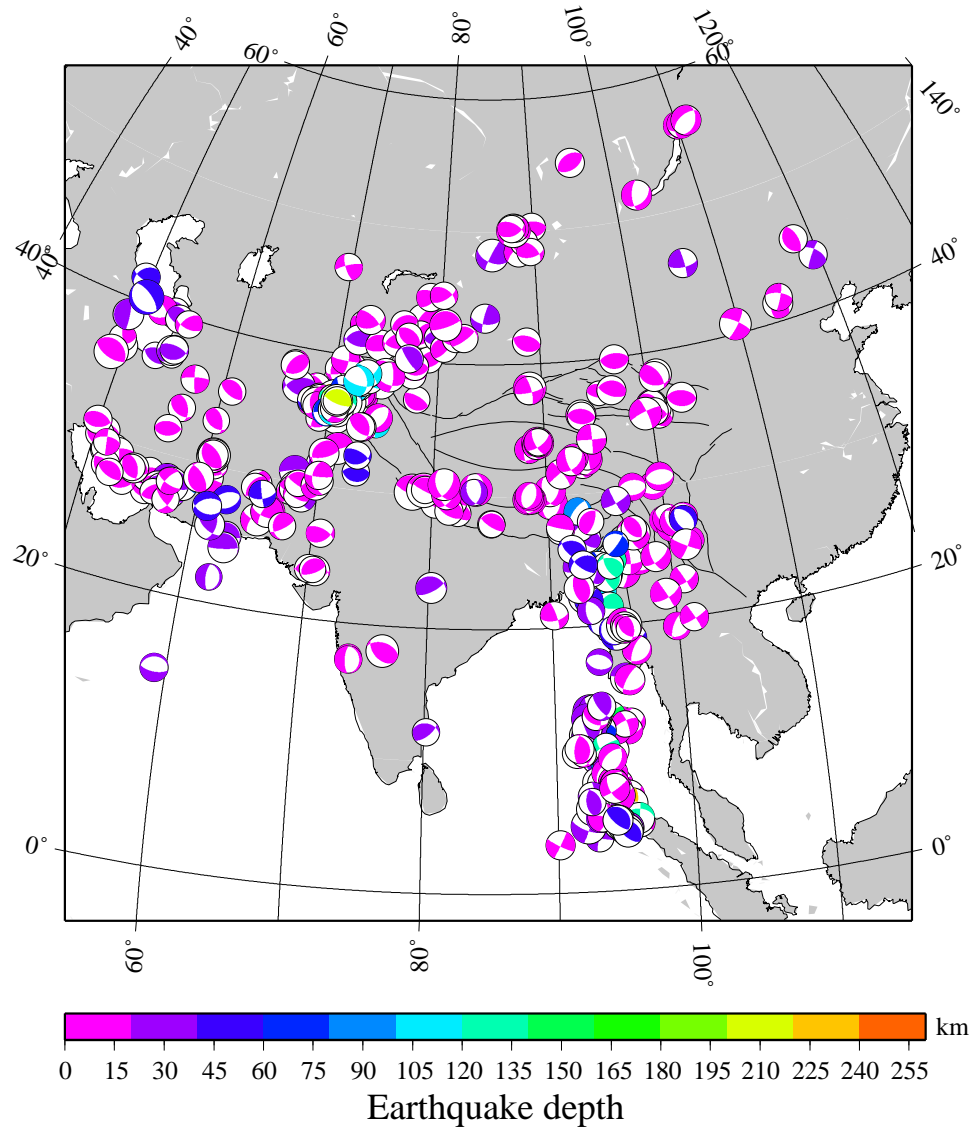


Figure 4.1: 504 earthquakes with verified focal mechanisms and depths using teleseismic P -wave waveforms.

observed data, I could verify focal mechanisms from the CMT solutions. Events with bad focal mechanisms were discarded. I then adjusted event depths by fitting the differential arrival times between P and the depth phases. 504 earthquakes with verified focal mechanisms were selected after this process (Fig. 4.1).

4.2.2 Estimate earthquake source time functions and depths

After the focal mechanism and approximate depth of the earthquake were verified, its teleseismic P -wave waveforms were deconvolved with the impulse responses using a time domain iterative deconvolution technique (KIKUCHI and KANAMORI, 1982). Because source time functions are always positive, I added a positivity constraint to the deconvolution algorithm. I then stacked all the source time functions from stations in different directions to obtain the average source time function.

For deep earthquakes, the separation between the direct P -wave arrival and depth phases are large enough that the focal depth error will not affect the source time function estimation. For shallow events, whose depth phases are within the source duration, accurate source depth is required for a reliable source time function. In this case, I repeated the deconvolution with different focal depths until the synthetic and the resulted impulses responses match (Fig. 4.2).

By applying this method to 504 earthquakes with good focal mechanisms from the CMT catalog, I estimated focal depths and source time functions. Fig. 4.2 shows an example for a deep earthquake with a focal depth at 122 km. The source time function of this event is very simple with a duration of 1.7 sec. Fig. 4.3 shows results for a shallow earthquake at 11 km with a source duration of 3.0 sec. The depths phases are within the source duration. The retrieved source time function is simple and the synthetic impulse responses agree with the observed responses very well. Fig. 4.4 shows the results for a deep earthquake with a complex source time function. Two sub-events can be identified from the estimated source time function.

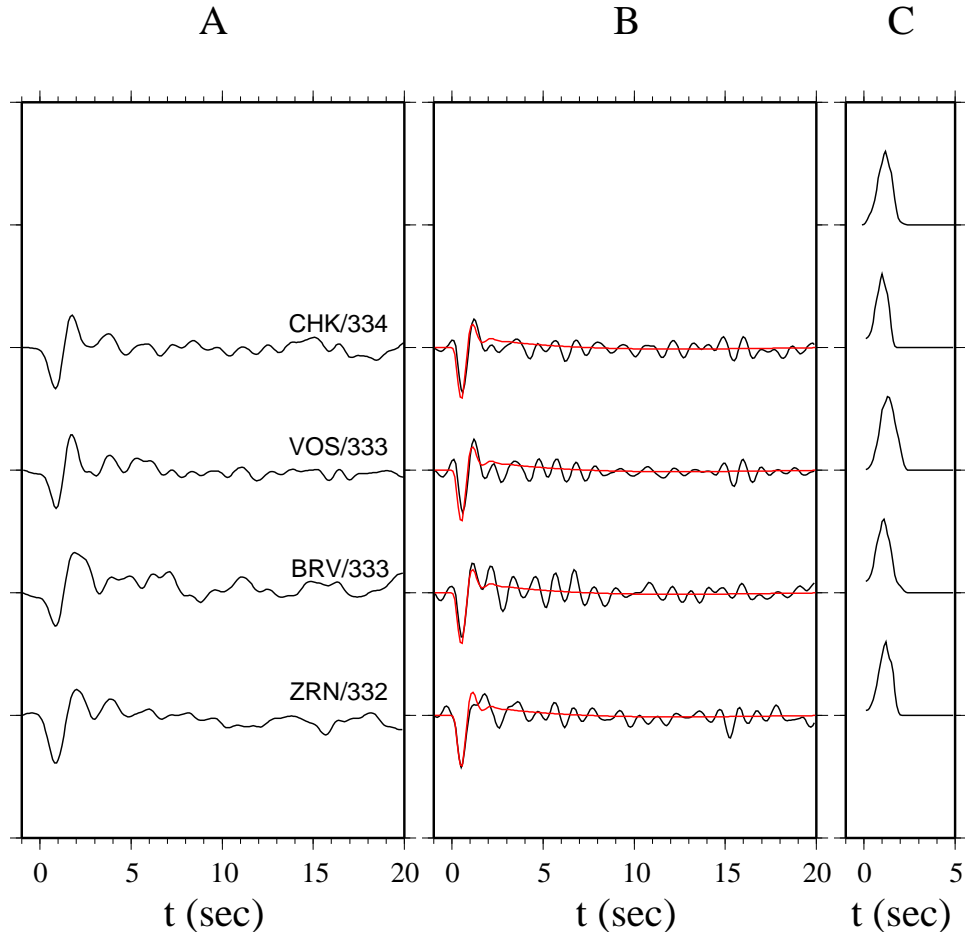


Figure 4.2: An example to illustrate the procedure to obtain earthquake source time function. The event is a $M_w = 5.5$ deep event (19980502083650) in the Hindu-Burma area with a focal depth of 122 km. The vertical components of teleseismic P -wave data (A) are deconvolved from theoretical Green's functions (red traces in B) to obtain the source time functions in C. The top trace in C is the averaged source time function. Deconvolution of data with the averaged source time function yields the “observed” Green's functions shown in black in B. The similarity of the red and black traces in B attests the stability of the approach and the correctness of the focal depth.

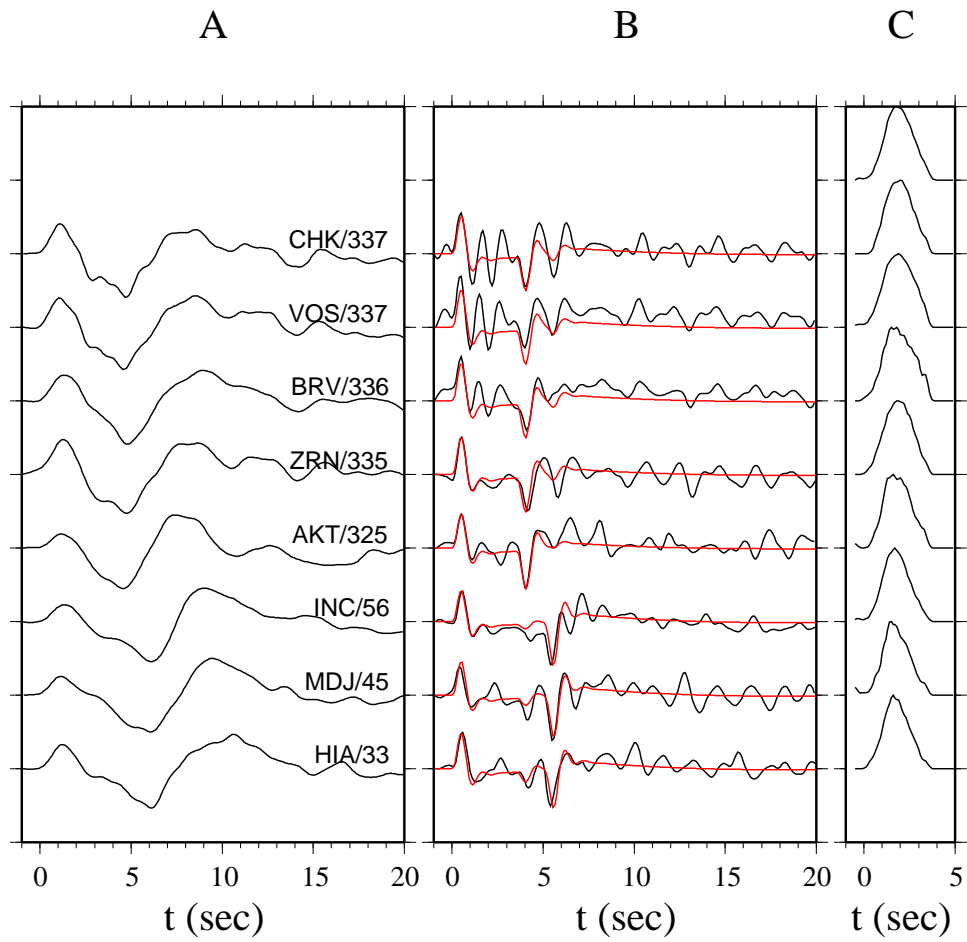


Figure 4.3: Another example to show the procedure to obtain earthquake source time function using a $M_w = 5.6$ shallow event (20030726231817) occurred in the Hindu-Burma area with a focal depth of 11 km, see Fig. 4.2 caption for details.

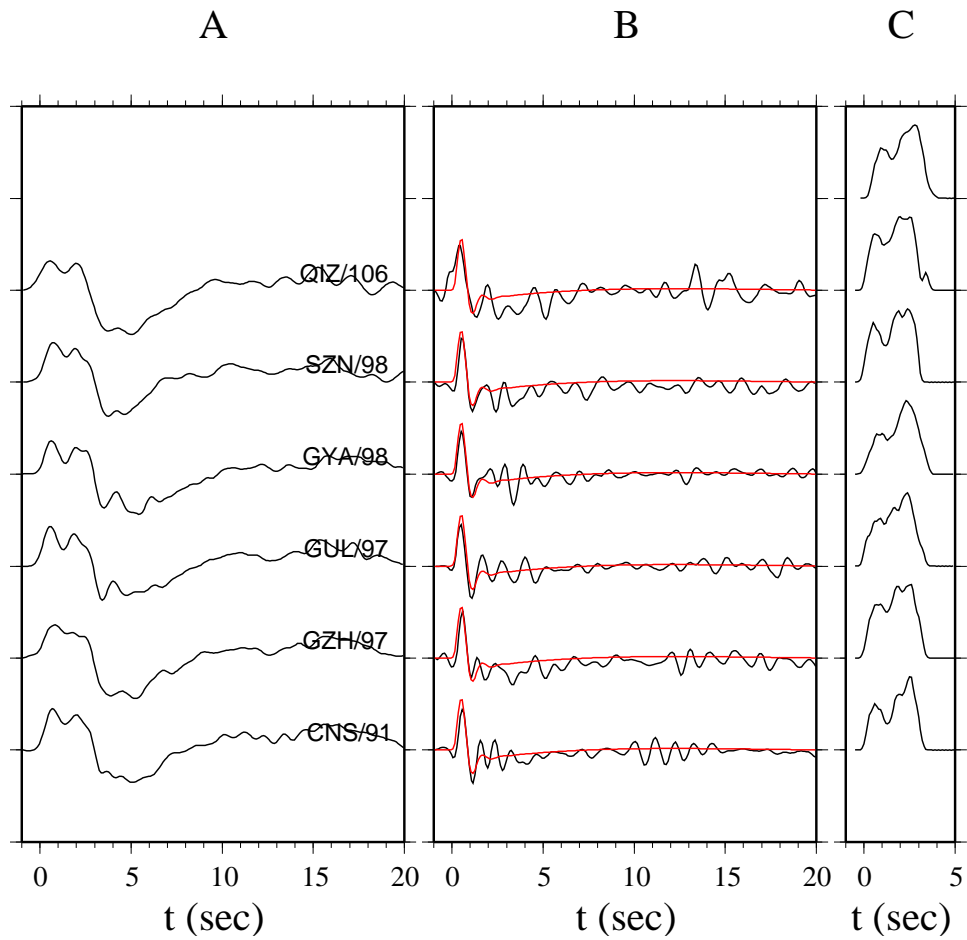


Figure 4.4: The third example to illustrate the procedure to obtain earthquake source time function. The event is a $M_w = 6.0$ deep event (20040810014732) in the Hindu-Kush area with a focal depth of 196 km, see Fig. 4.2 caption for details. This event has a complex source time function.

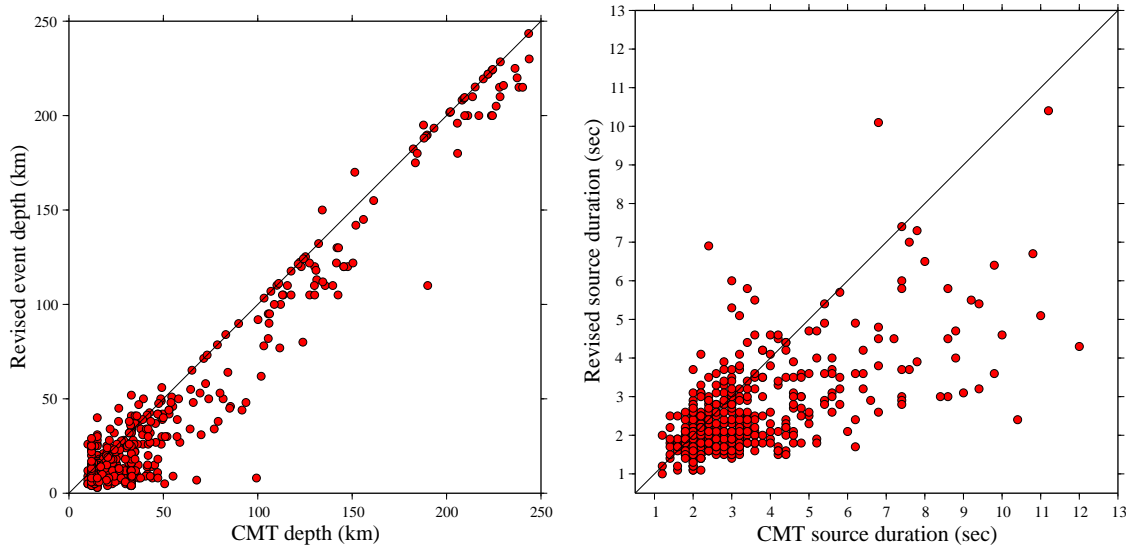


Figure 4.5: Re-estimated focal depths (left) and source durations (right) versus those from the CMT catalog.

4.3 Comparison of focal depths and source durations with the Harvard CMT solutions

I compared the re-determined earthquake depths and source durations with those in the CMT catalog (Fig. 4.5). It is clear that the event depths are systematically shallower than those from the CMT catalog. The differences between the two depths are usually 20–30 km and can be as large as 60 km. In the CMT catalog, there is a minimum depth at 15 km, which corresponds to the cut-off depth of the CMT solutions. The CMT catalog also provides the source’s half duration. It was calculated from the moment magnitude using empirical relations (HELFFRICH, 1997). Fig. 4.5 shows that the source durations in the CMT catalog are systematically longer than the estimated durations.

4.4 Source scaling relations of earthquakes around the Tibetan Plateau

The source time function of an earthquake describes how the fault system releases energy and relates to the rupture dynamics. The duration of the source

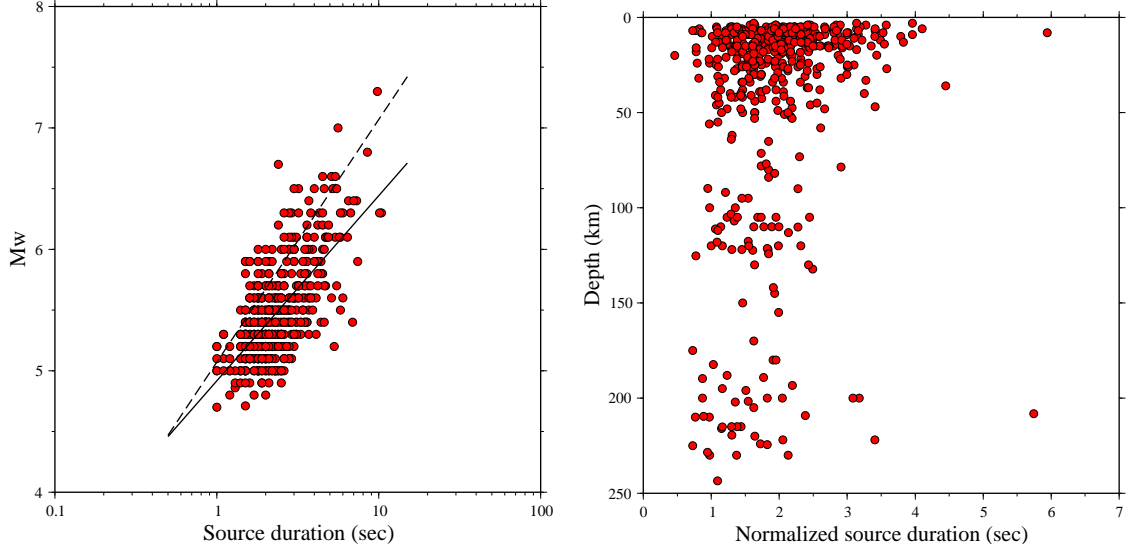


Figure 4.6: Source magnitude versus duration (left) and normalized duration versus focal depth (right). Solid line on the top panel is the least-squares fit line with the relation $M_w = 1.52 \log(\tau) + 4.92$. Dashed line is the empirical relationship $M_w = 2.0 \log(\tau) + 5.07$ by SOMERVILLE *et al.* (1987).

time function can be used to estimate the stress drop of the rupture. Large earthquakes tend to have long source durations. The relationship is approximated by a empirical formula between the seismic moment M_0 and source duration τ (KANAMORI and ANDERSON, 1975; SOMERVILLE *et al.*, 1987),

$$\log M_0 \propto 3.0 \log \tau, \quad (4.1)$$

or

$$M_w \propto 2.0 \log \tau. \quad (4.2)$$

By using a least-squares fit between M_w and $\log \tau$ of my results, I found that the best-fit straight line has a slope of 1.52, which is smaller than 2.0 (Fig. 4.6). The small slope indicates that earthquakes in this area on average have shorter source durations and thus higher stress drops than those in North America (SOMERVILLE *et al.*, 1987).

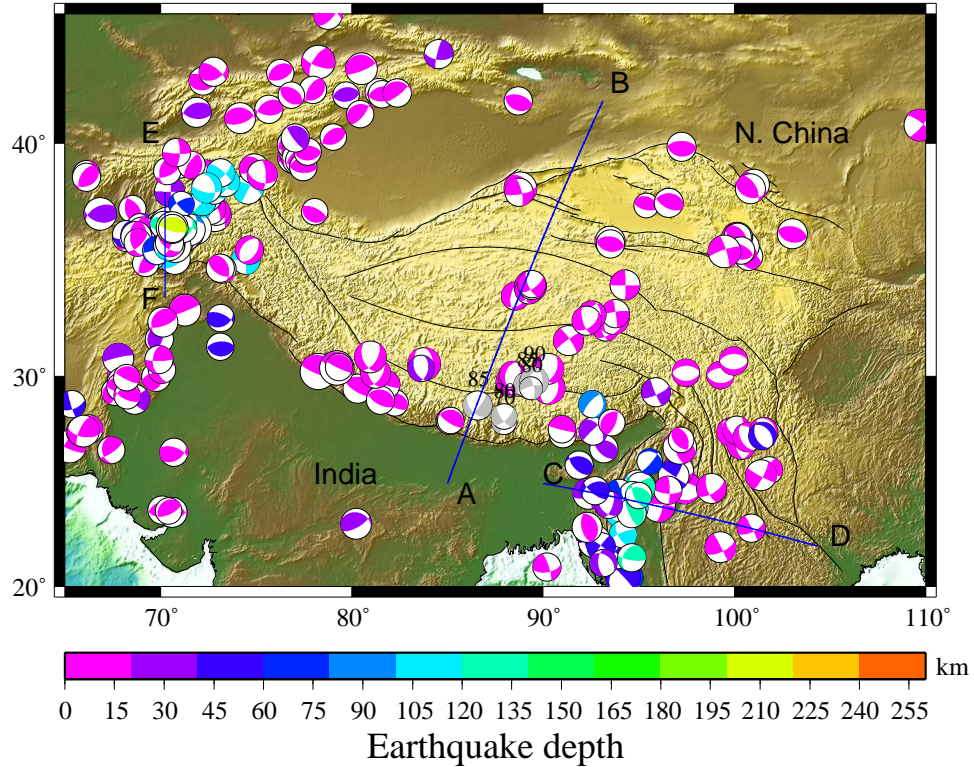


Figure 4.7: Focal mechanisms and depths of earthquakes in and around the Tibetan Plateau. Grey beach balls represent intermediate-depth earthquakes found in previous studies (CHEN and MOLNAR, 1983; ZHU and HELMBERGER, 1996). AB, CD, and EF are three profiles across the Tibetan Plateau, Hindu-Burma, and Pamir-Hindu Kush areas, respectively.

Stress drops, which are related to earthquake source durations, are affected by earthquake depths. Previous studies indicate that deeper earthquakes have shorter source durations and higher stress drops, given the same magnitude (BOS *et al.*, 1998; BILEK and LAY, 1998, 1999; BILEK, 2007). In order to investigate this relation for earthquakes around the Tibetan Plateau, source durations are normalized by Eq. 4.1 to a reference magnitude $M_w = 6.0$. Fig. 4.6 shows that normalized source durations decrease slightly with depth, confirming that stress drops increase with increasing earthquake depth.

4.5 Focal depths and mechanisms in and around Tibet

The re-determined focal depths show that most events in and around the Tibetan Plateau are within the uppermost 15 km of the crust (Fig. 4.7). This shallow distribution of foci indicates that the lithosphere in these areas is relatively warm and that the brittle-ductile transition in the crust is shallow. Deep events with depths larger than 70 km are found in the Hindu-Burma, the Himalayas and southern Tibet, and the Pamir-Hindu Kush areas. Except in southern Tibet, deep earthquakes are related to subduction of ancient slabs.

4.5.1 The Tibetan Plateau

No Wadati-Benioff zone has been observed beneath the India-Eurasia collision zone and the Tibetan Plateau (Fig. 4.8). Earthquakes are concentrated in the uppermost 20 km of crust. Focal mechanisms around Tibetan Plateau indicate three major types of faulting (Fig. 4.7), as previously pointed out by MOLNAR *et al.* (1973) and MOLNAR and LYON-CAEN (1989). They are: 1) thrust faulting in the Himalaya area and northeastern Tibetan Plateau. The principal P-compression axes are in the NE-SW direction, which is consistent with the India-Eurasia collision direction. Thrust angles are shallower in high latitude, indicating the shortening in the forms of folding and thrusting in the north; 2) normal faulting in southern Tibetan Plateau where the plateau reaches its highest elevation; and 3) strike-slip faulting in central and east Tibetan Plateau along major faults. The T-axes are oriented to the E-W and NW-SE directions, which agrees with GPS measurements of crustal movement (WANG *et al.*, 2001).

Only one event in my study was found to be an intermediate-depth earthquake. It is located at 76 km depth beneath the IZS with a normal faulting focal mechanism (Fig. 4.7). I also plotted six intermediate-depth earthquakes discovered so far by MOLNAR and CHEN (1983); CHEN *et al.* (1981); CHEN (1988); ZHU and

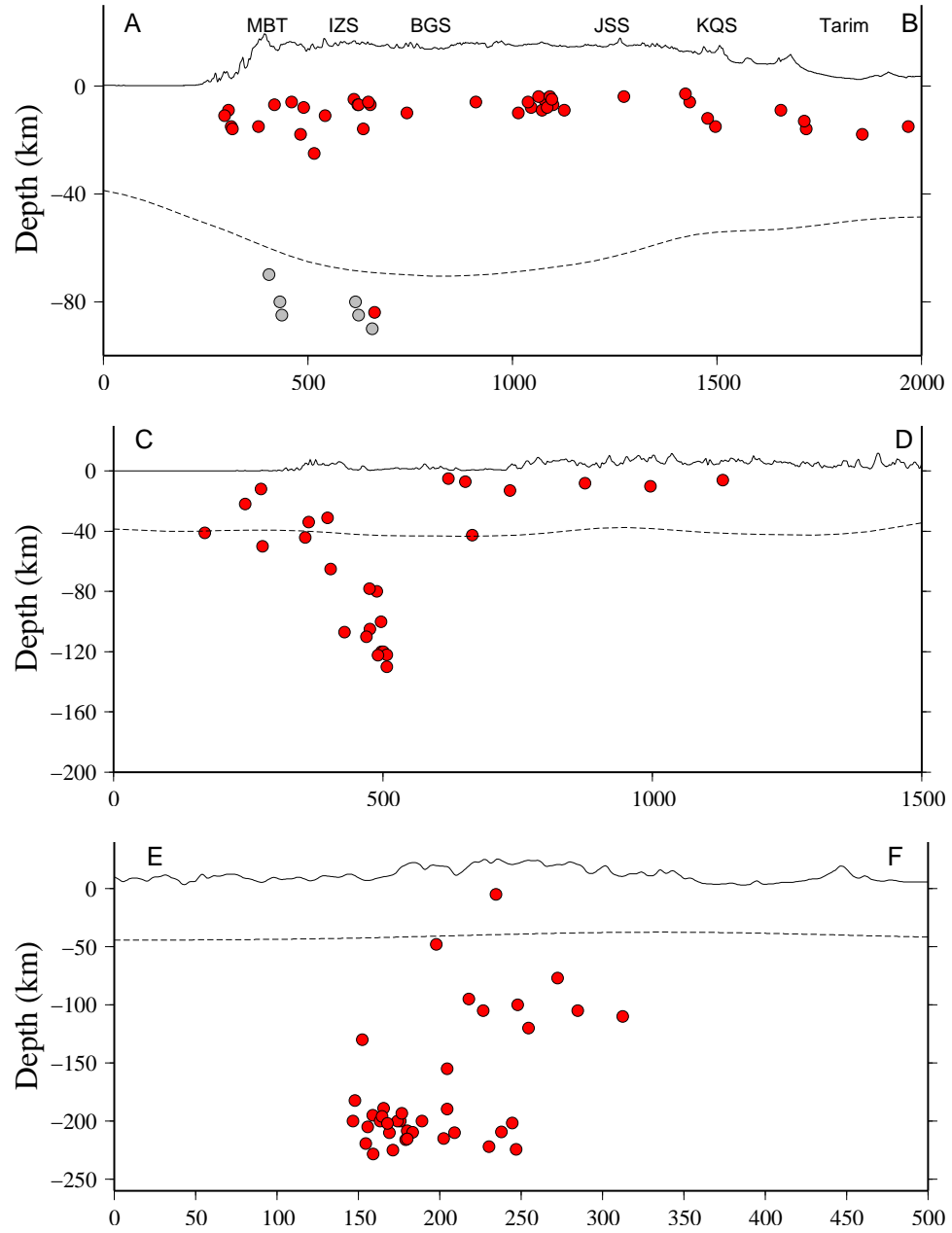


Figure 4.8: Earthquakes (red dots) along three profiles across the Tibetan Plateau (top), the Hindu-Burma (middle), and the Pamir-Hindu Kush (bottom). Positions of these profiles are marked on Fig. 4.7. Dashed lines denote Moho interface from BASSIN *et al.* (2000). The surface topography is amplified by a factor of 3 for the Tibetan Plateau, 5 for other two profiles. MBT: the Main boundary thrust, IZS: the Indus-Zangbo Suture, BGS: the Bangong Suture, JSS: the Jingsha Suture, KQS: the Kunlun-Qinling Suture.

Table 4.1: Intermediate-depth events in southern Tibet from previous studies

Date	Lat.	Lon.	Str./Dip/Rake	Dep,km	Note
08/01/1973	29.60	89.13	220/60/-24	85	MOLNAR and CHEN (1983)
09/14/1976	29.78	89.54	215/52/-68	90	CHEN <i>et al.</i> (1981)
01/10/1986	28.66	86.57	140/46/-163	85	CHEN (1988)
12/21/1991	27.89	87.96	112/82/-179	70	ZHU and HELMBERGER (1996)
03/07/1992	29.44	89.37	350/68/-164	80	ZHU and HELMBERGER (1996)
04/04/1992	28.15	87.96	46/66/-22	80	ZHU and HELMBERGER (1996)

HELMBERGER (1996) (Fig 4.8). These seven events are all in southern Tibet and Himalaya area. CHEN and YANG (2004) argued that these events are not related to subduction because their focal mechanisms resemble to those in the upper crust, and suggested a bimodal distribution of earthquakes in the southern Tibet. However, tomography studies showed that the Indian lithosphere underlay the southwestern margin of the Tibetan Plateau, beneath the IZS (VAN DER VOO, 1999; REPLUMAZ *et al.*, 2004; LI *et al.*, 2006). PRIESTLEY *et al.* (2008) argued that the intermediate-depth events actually occurred at the base of the subducting Indian lithospheric slab, which could accumulate strain at this depth range.

4.5.2 Hindu-Burma

Earthquake fault plane solutions in the Hindu-Burma area show two types of focal mechanisms. Shallow events within the upper crust exhibit strike-slip faulting with the compressional axes in the SE-NW direction, while deep earthquakes are characterized by thrust faulting with the compressive direction in nearly EW. The orientations are compatible with the known tectonic stress direction produced by the subduction of the Indian Plate beneath the southeastern Asian Plate. Intermediate-depth earthquakes in the Hindu-Burma area are the result of the

subduction and reach a depth of nearly 200 km (CHEN and MOLNAR, 1990; KAYAL, 1987; KAYAL and ZHAO, 1998; LE DAIN *et al.*, 1984). Seismicity in this region shows a eastward dipping of the Indian lithospheric slab (Fig. 4.8).

4.5.3 Pamir-Hindu Kush

The subduction between the Indian Plate and the Eurasia Plate in the Pamir-Hindu Kush area displays complex tectonics. Earthquake hypocenters show a 700 km long S-shaped seismic zone extending to a depth of at least 250 km. The seismic zone is associated with a strong velocity anomaly which was thought to be a subducted oceanic lithosphere (MELLORS *et al.*, 1995; KOULAKOV and SOBOLEV, 2006). In western and central Hindu Kush, the Indian plate subducts northwards under the Eurasia Plate, while, under the Pamir, it is unclear whether the Indian plate overturns or the Eurasian Plate subducts southwards (FAN *et al.*, 1994; ZHU *et al.*, 1997; PEGLER and DAS, 1998; PAVLIS and DAS, 2000). Two Wadati-Benioff zones delineated by earthquakes can be easily identified from the profile across the Pamir-Hindu Kush area (Fig. 4.8). The shallower south dipping zone corresponds to the southward subduction. The steeper dipping zone is the India subduction.

There is a seismicity gap at the depth of about 70 km across the profile between the shallow crustal events and deep mantle earthquakes (Fig. 4.8). It has been suggested that this gap indicates the decoupling of crust and upper mantle deformation fields through pervasive deformation of the lower crust beneath the Pamir (PAVLIS and DAS, 2000). It can also be explained by the characteristics of continental subduction (FAN *et al.*, 1994).

In summary, a new method was developed to retrieve source time functions and focal depths from teleseismic P waveforms. I applied this method to 504 earthquakes around the Tibetan Plateau. The results suggest that the Harvard CMT catalog, routinely calculated from very long period body and/or surface

waves, provides very important information about centroid locations and moment tensor, but the focal depths and source durations are not well determined. Both of them are systematically larger than the actual values, especially for shallow events. Source scaling relations of these earthquakes indicated that the stress drops around the Tibetan Plateau are larger than stress drops of earthquakes in North America.

Most of the earthquakes in the Tibetan Plateau and surrounding area are in the top 15 km of the crust. Intermediate-depth earthquakes are clustered in southern Tibet, Hindu-Burma, and Pamir-Hindu Kush area. Deep events in the Hindu-Burma and Pamir-Hindu Kush areas are related to subduction of oceanic slabs. Several earthquakes that occurred in southern Tibet are found to be intermediate-depth earthquakes.

Chapter 5: Upper-mantle Velocity Structure Beneath the Tibetan Plateau and Surrounding Areas

5.1 Lateral velocity variations revealed by upper-mantle distance waveforms

From the 504 events with estimated source time functions and focal depths, I obtained 11,306 P waveforms in the upper-mantle distances with turning points beneath the Tibetan Plateau and surrounding area (Fig. 5.1). The turning points cover most parts of the western Tibetan Plateau, the Hindu-Kush area, and the Hindu-Burma region. Western Tibet, eastern Tibet, and the Tarim Basin have excellent coverage of waveforms with a distance range between 12° and 20° , while central Tibet and southern Tibet have less-than-ideal coverage.

Fig. 5.2 to Fig. 5.4 show typical examples of P -waveform profiles. I first hand-picked the first- P arrival times on all available traces. In order to remove the arrival time delays caused by inaccurate event origin times and near-source structural variation, I calculated an event delay for each event by minimizing the RMS of travel-time residuals between observations and predictions by the IASP91 model for the EF branch. The travel times predicted using the estimated event delays are shown in Fig. 5.2-5.4. It is clear that the predictions agree well with the picked arrival times at distances larger than 20° . The residuals are usually smaller than 1.0 sec. In the distance range between 12° and 20° , the difference between the observed arrival times and predictions can be as large as 7 sec. This indicates large velocity variation in the upper mantle above the 410 discontinuity.

I calculated travel time residuals for all of the 11,306 traces. Fig. 5.5, Fig. 5.6, and Fig. 5.7 show travel-time residuals for traces turning in the lower mantle, in the transition zone, and above the 410 discontinuity, respectively. I placed the travel-time residual at the turning point because it is most sensitive to the velocities

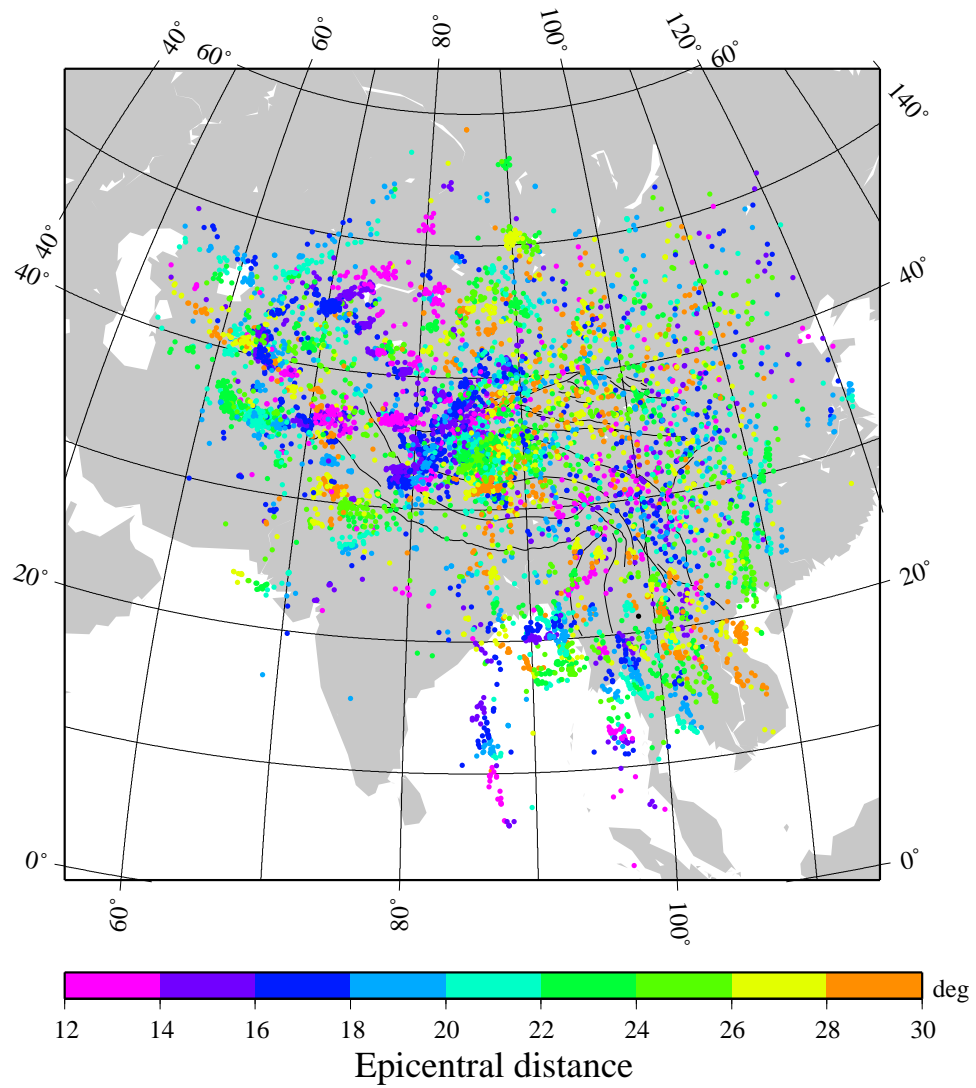


Figure 5.1: Turning point (color dots) distribution of the 11,306 P -wave waveforms from 504 earthquakes. Color scale shows epicentral distance of each trace

19900109022926

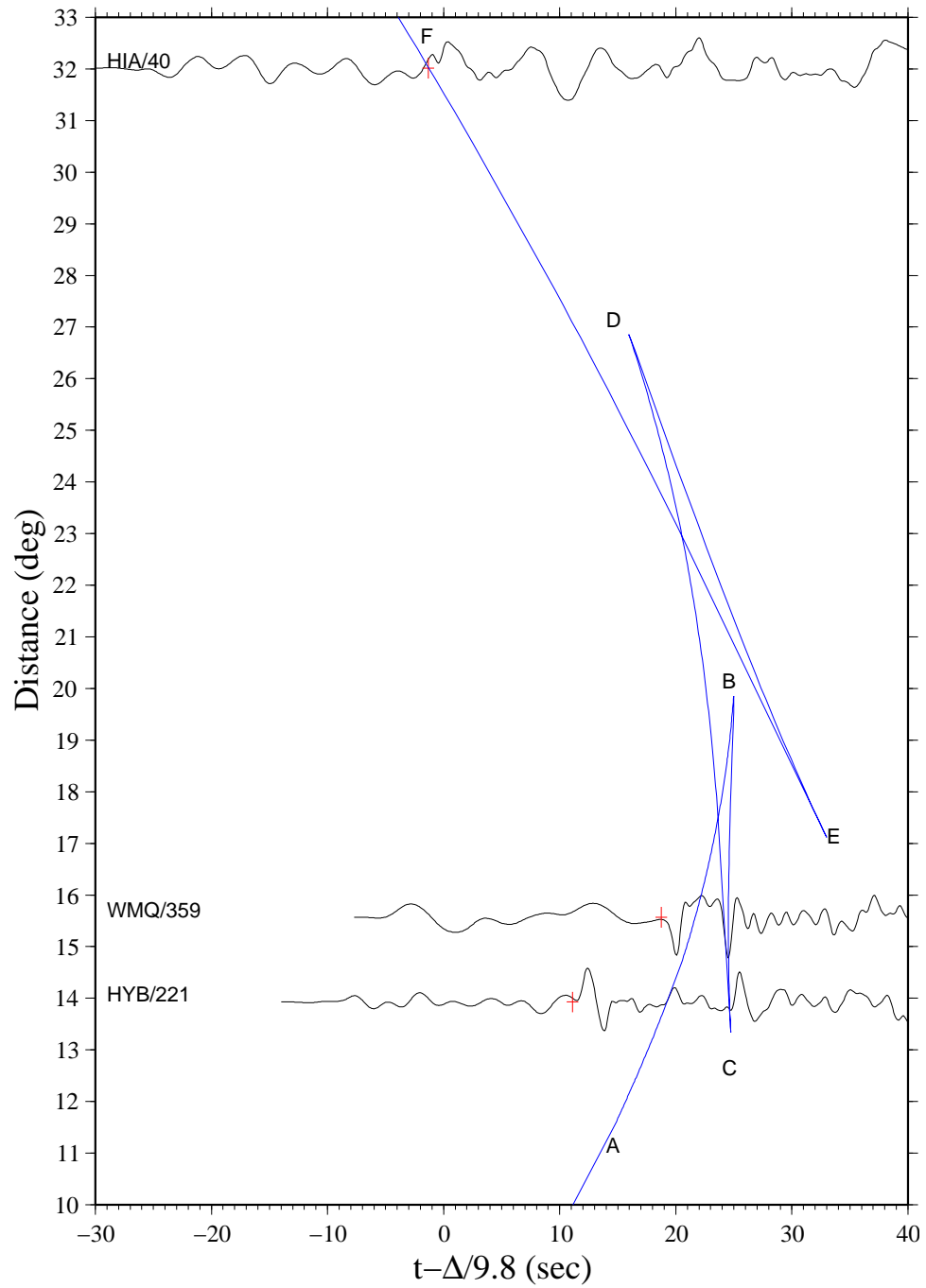


Figure 5.2: *P*-wave profile of event 19900109022926. Red crosses are picked arrival times and blue-color curves represent theoretical arrival times of different branches predicted by the IASP91 model. Numbers after station names are azimuth of each waveform.

19921204113636

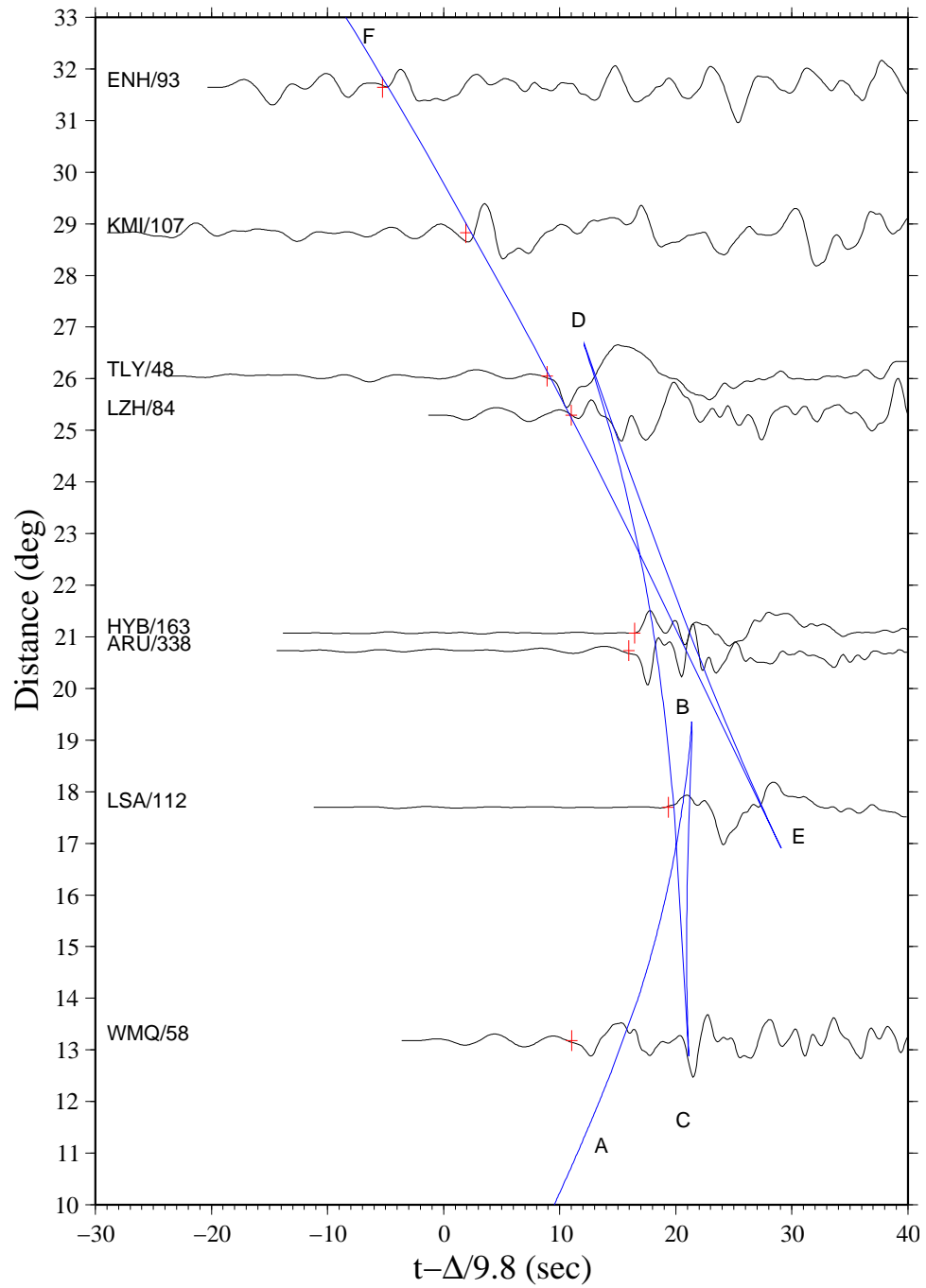


Figure 5.3: *P*-wave profile of event 19921204113636. Red crosses are picked arrival times and blue-color curves represent theoretical arrival times of different branches predicted by the IASP91 model. Numbers after station names are azimuth of each waveform.

19940701101241

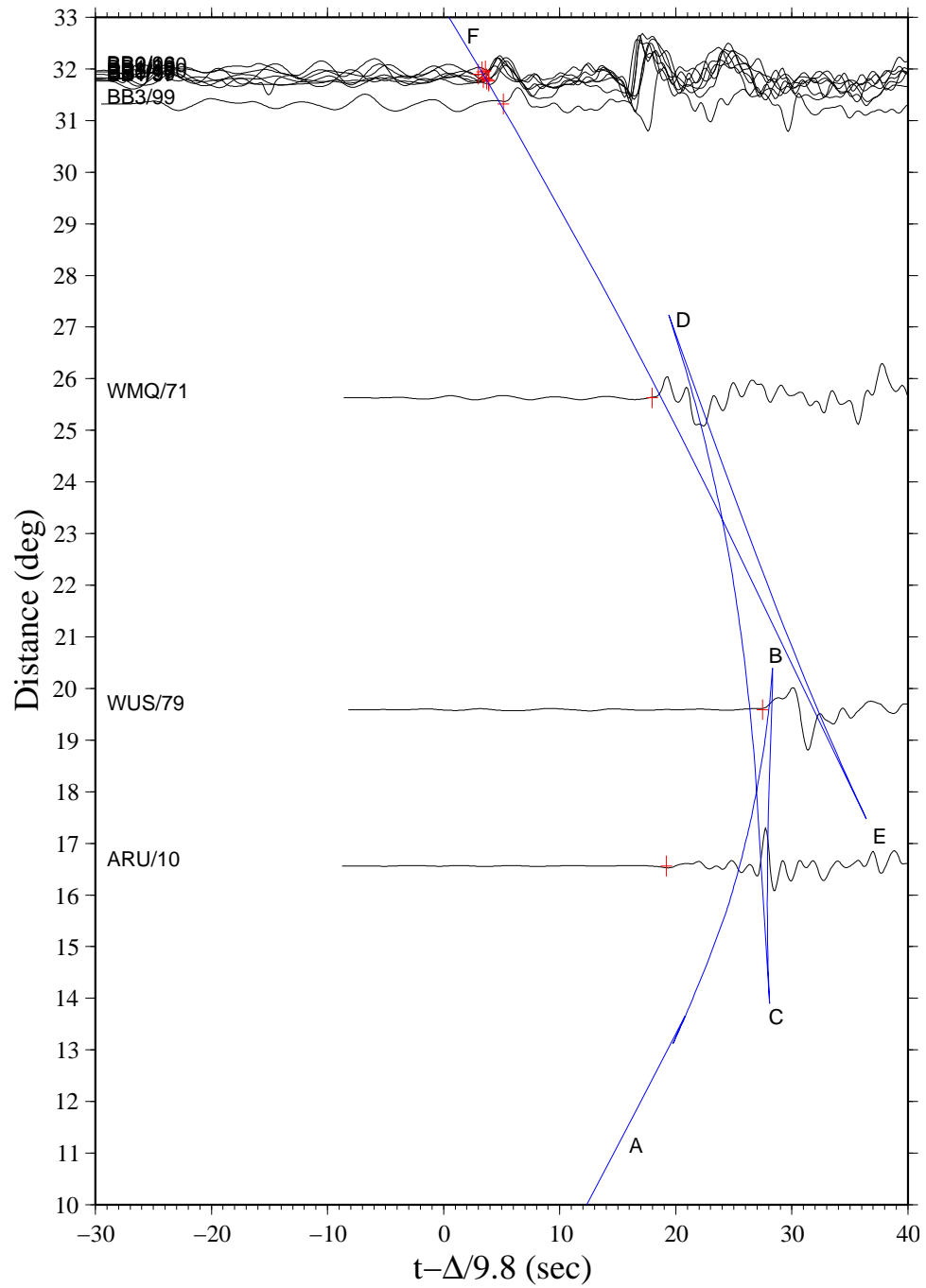


Figure 5.4: *P*-wave profile of event 19940701101241. Red crosses are picked arrival times and blue-color curves represent theoretical arrival times of different branches predicted by the IASP91 model. Numbers after station names are azimuth of each waveform.

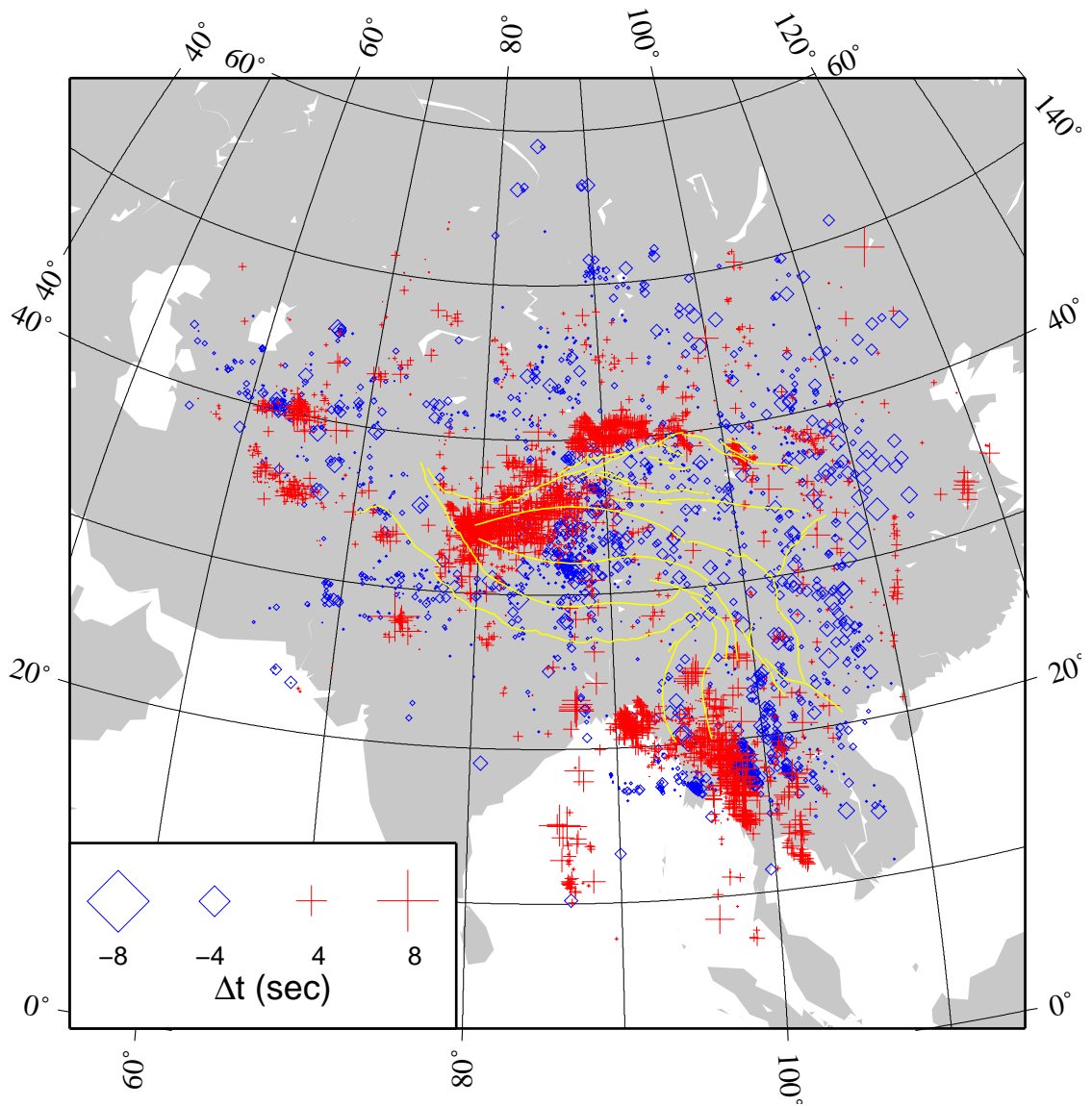


Figure 5.5: Travel-time residuals for seismic rays turning below the 660 discontinuity. Blue diamonds and red crosses represent negative and positive residuals, respectively. Size of the symbol corresponds to magnitude of the residual.

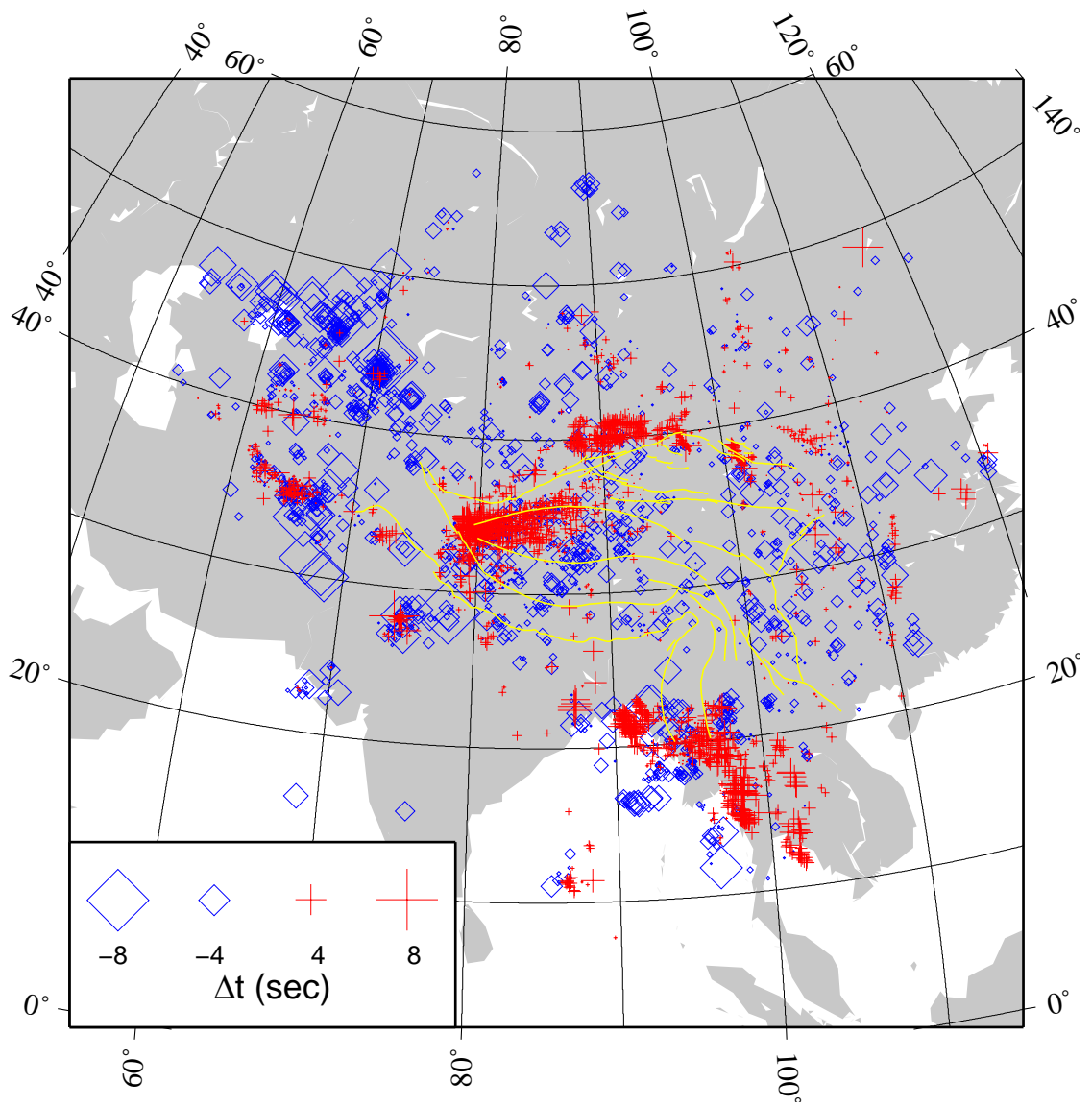


Figure 5.6: Travel-time residuals for seismic rays turning in the transition zone.

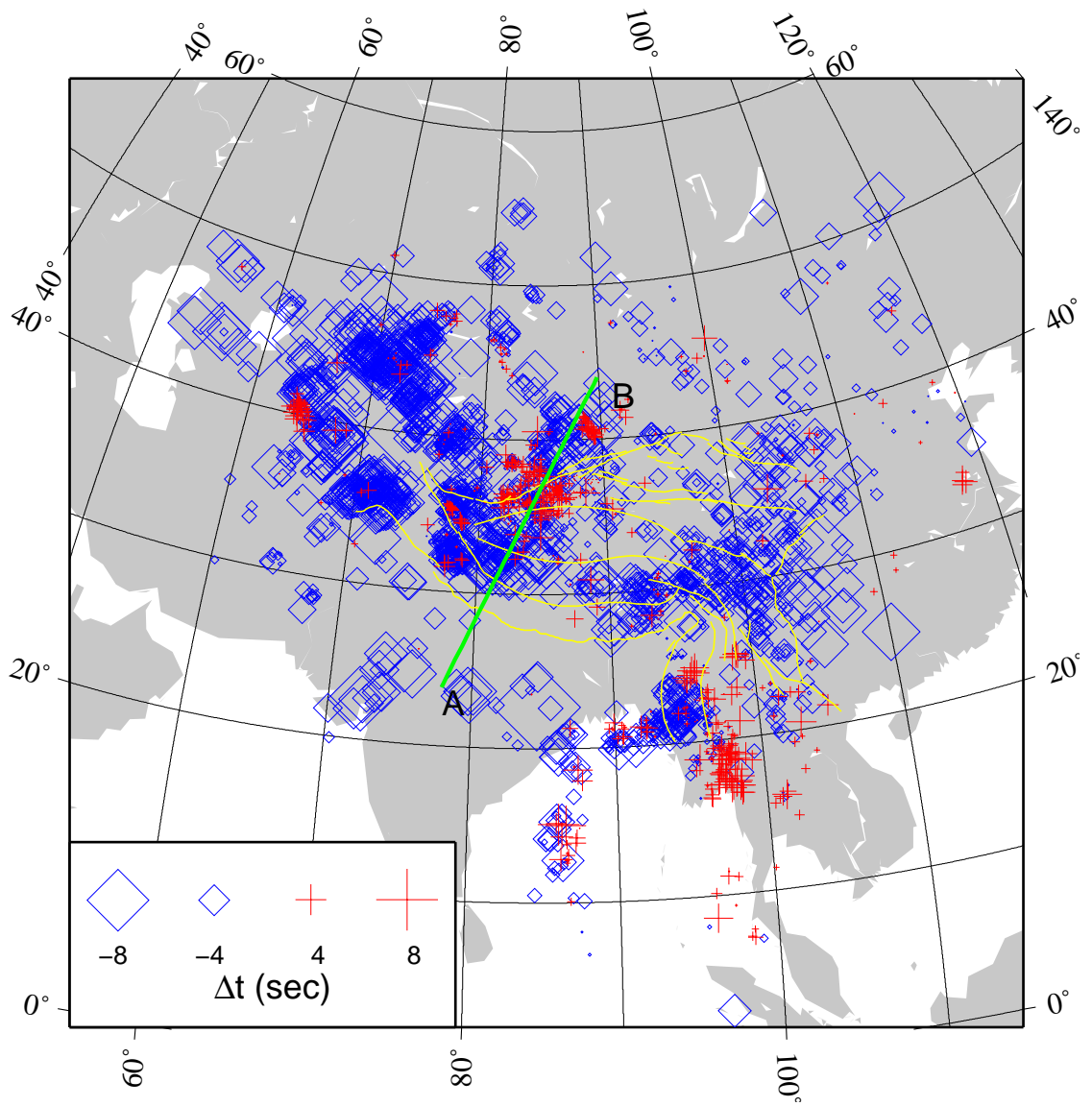


Figure 5.7: Travel-time residuals for seismic rays turning above the 410 discontinuity.

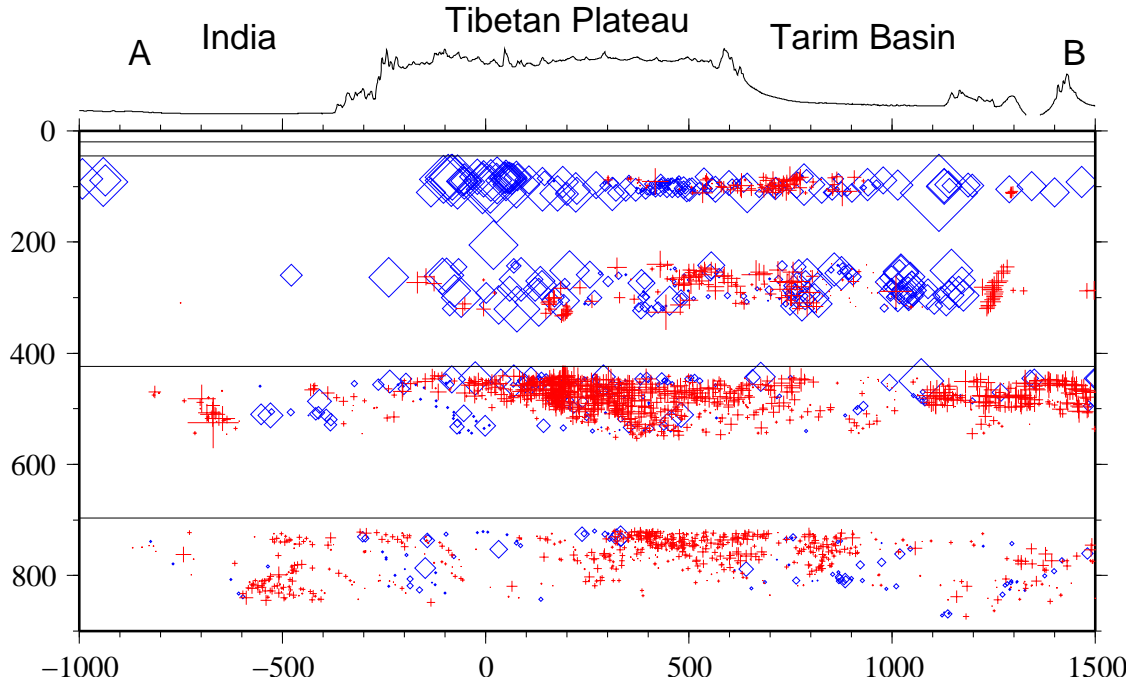


Figure 5.8: Travel time residuals along the AB profile shown in Fig. 5.7. The surface topography is amplified by a factor of 20.

near the turning point. Negative travel-time residuals indicate that the velocities around the turning points are faster than those of the IASP91, and positive residuals suggest slow velocity anomalies.

Travel-time residuals below 410 km are small throughout the study area (Fig. 5.5 and Fig. 5.6), which indicates that the velocities below 410 km beneath the whole area are close to the IASP91. Negative residuals above 410 km dominate most of the area (Fig. 5.7), including India, southern Tibet, central Tibet, and eastern Tibet, which means that the velocities above 410 km are faster than the upper-mantle velocities of IASP91 in these areas. Positive travel-time residuals are mainly concentrated between 200 km and 300 km beneath the Tarim Basin, western Tibet, and southeastern Asia, which suggest lower velocities (Fig. 5.8).

5.2 Waveform modeling and results

Using the distribution of turning points shown in Fig. 5.1 and Fig. 5.7, I divided the area along the AB profile into six regions: India, the Himalayas (HL), the Lhasa Terrane (LS), the Qiangtang Terrane (QT), the Songpan-Ganzi Terrane (SG), and the Tarim Basin (TB). Waveforms with turning points beneath each region were grouped for modeling to obtain the best 1-D upper-mantle velocity model for the region. To ensure good data quality, I inspected each waveform in the group and only kept those with a clear first P arrival. I then used the verified Harvard CMT solutions and revised focal depths to compute synthetic seismograms. This helped identify other late phases. Since the modeling technique relied on using a deep-turning phase, such as the 410 or 660 reflection, as the reference phase to align the data and synthetic waveforms, only traces with at least one clear deep-turning phase were used for the modeling.

The waveforms in each group were from different earthquakes at various depths. In order to construct a single epicentral distance profile for modeling using waveforms of different earthquakes in the group, it was necessary to correct for the source-depth effect because waveforms from a deep earthquake had larger effective epicentral distances on the profile than those from a shallow event. Fig. 5.9 shows synthetic P waveforms from two events, one at a depth of 30 km and the other at 10 km. The two sets of waveforms are aligned at the first arrivals. It can be seen that the late phases are misaligned at a given epicentral distance. I chose 10 km as the reference source depth because most of the events used in this study were shallow earthquakes with focal depths at 4–30 km (Fig. 4.5). Differences between the true and effective epicentral distances were calculated using the ray parameter of the trace and a background velocity model. After correcting for the source-depth effect, all seismograms can be placed on a single epicentral distance profile (Fig. 5.10).

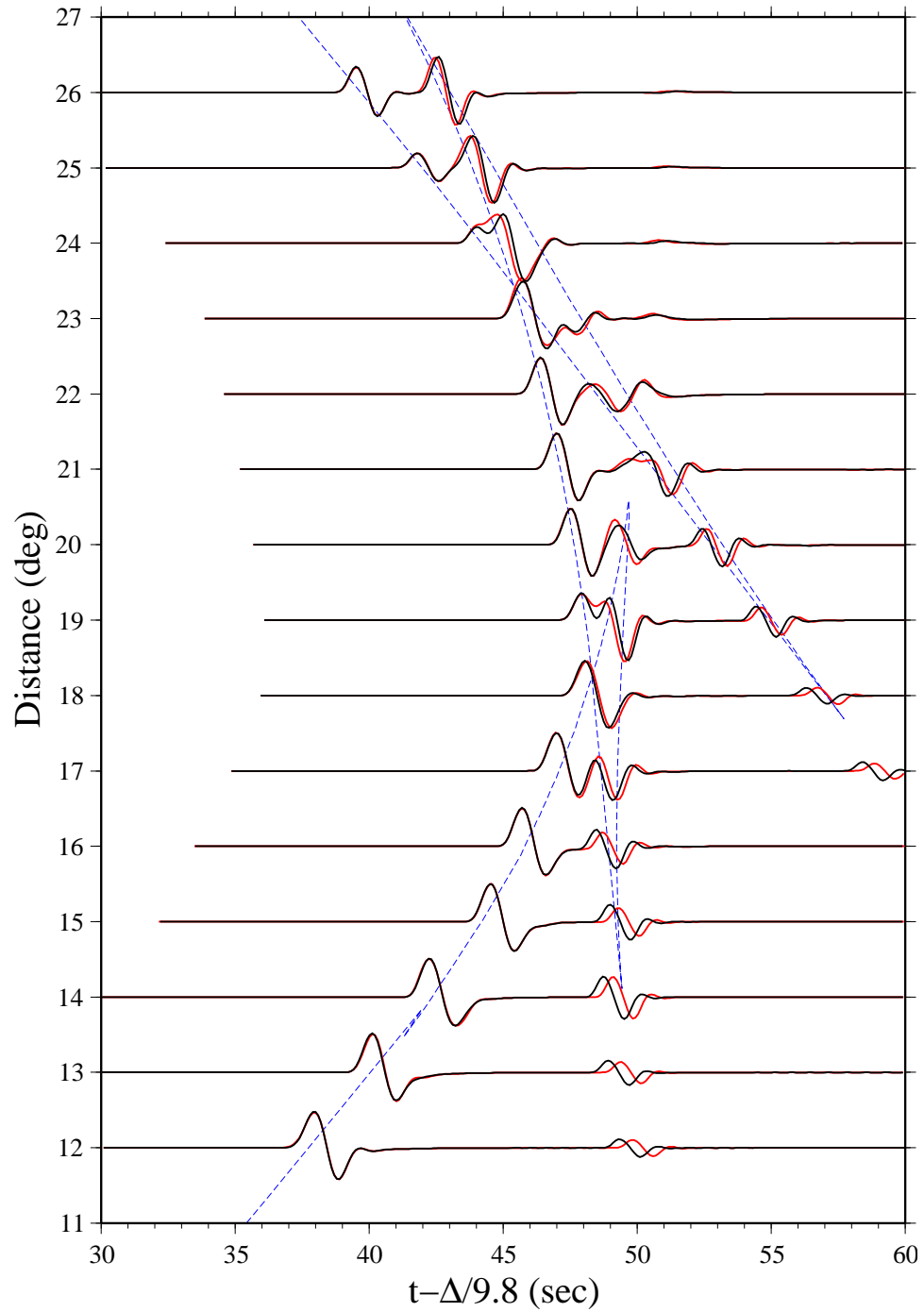


Figure 5.9: Synthetic P waveforms in the upper-mantle distances from two earthquakes with the focal depths at 30 km (black) and 10 km (red). All waveforms are aligned on the first arrivals.

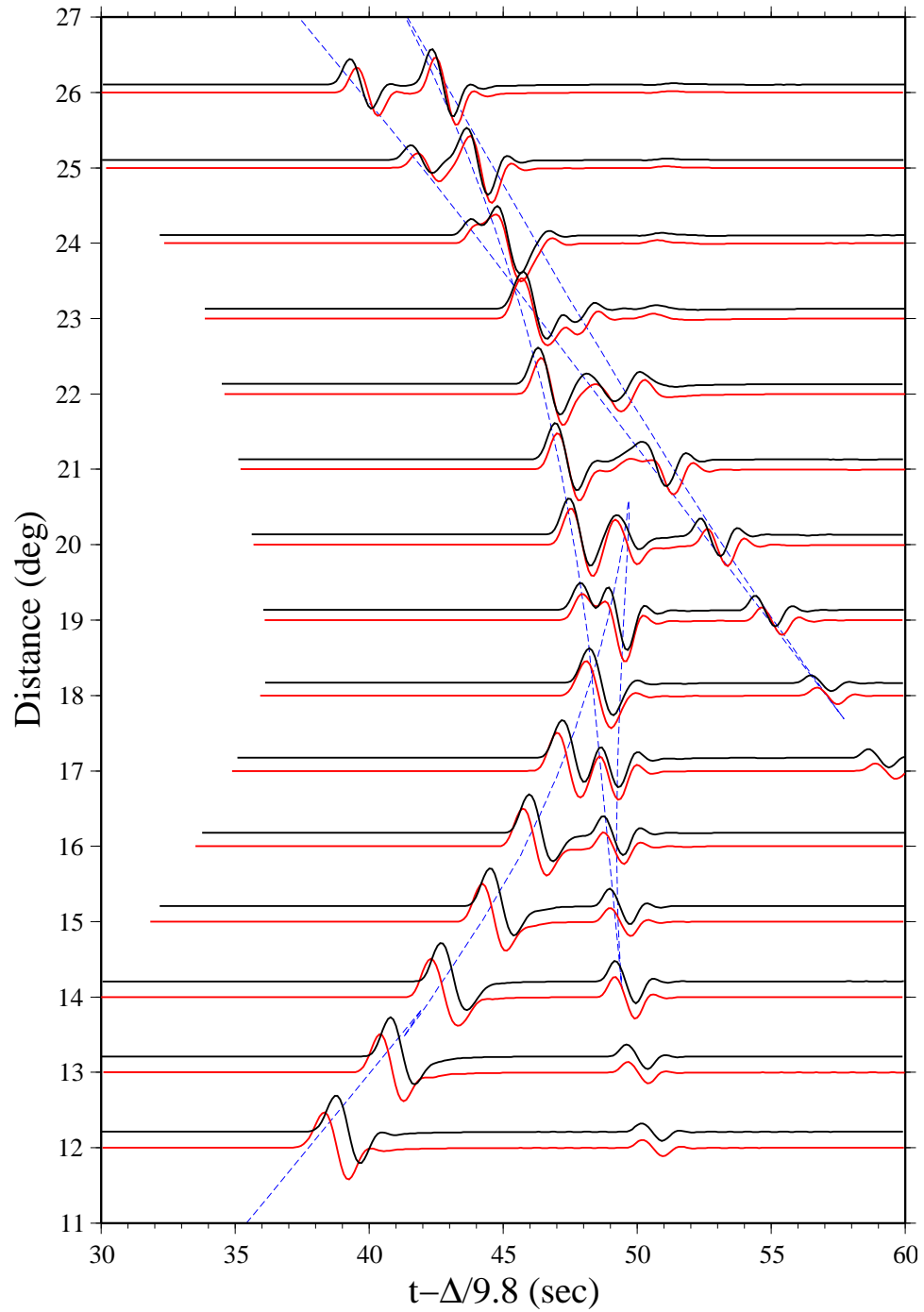


Figure 5.10: Same as in Fig. 5.9 except that the epicentral distances of the waveforms from the 30 km deep event (black) have been corrected to the effective epicentral distances of a 10 km deep source.

There were fewer usable traces with turning points beneath India compared to other regions, mainly due to small number of stations in the region. Fig. 5.11 shows locations of events and stations used for obtaining velocity structure beneath India. A total of 12 traces were selected. I first modeled the traces at distances of 22° to 28° to constrain the velocity structure between the 660 and 410 discontinuities. Synthetic seismograms of the IASP91 model matched the observations well. This meant that the velocity structure below the 410 was the same as the global average model. At shorter distances from 16° to 19° , the separations between the AB and CD branches in the observations were about 5 sec larger than the predictions of the IASP91 model, suggesting high-velocity anomalies in the upper mantle above the 410 discontinuity. I estimated the turning depths of these waveforms using the IASP91 model and adjusted velocities around the turning depths until the synthetics matched the data. Fig. 5.12 shows the final waveform fits. The best-fit velocity model has a thick high-velocity lid to a depth of 250 km with a P -wave velocity of 8.41 km/s (Fig. 5.13).

A similar upper-mantle velocity structure was obtained for the Himalayas (Fig. 5.14–5.16). A high-velocity lid was also found for the Lhasa Terrane (Fig. 5.17–5.20). The Lhasa Terrane had similar velocity structure above the 410 discontinuity as India and the Himalayas, but in order to fit the smaller separations between the CD and EF branches between the distances of 24° and 26° (Fig. 5.18), a high-velocity perturbation of a 0.2 km/s increase in the bottom of the transition zone was required (Fig. 5.20).

Modeling the waveforms at large distances for the Qiangtang Terrane also resulted in similar high-velocity anomaly in the transition zone beneath the region. The observed CD-EF separations at distances larger than 25° are smaller than the predictions of the IASP91 model. (Fig. 5.22), but separations between 20° and 25° agreed with the IASP91 predictions. This constrained the anomaly's location to be

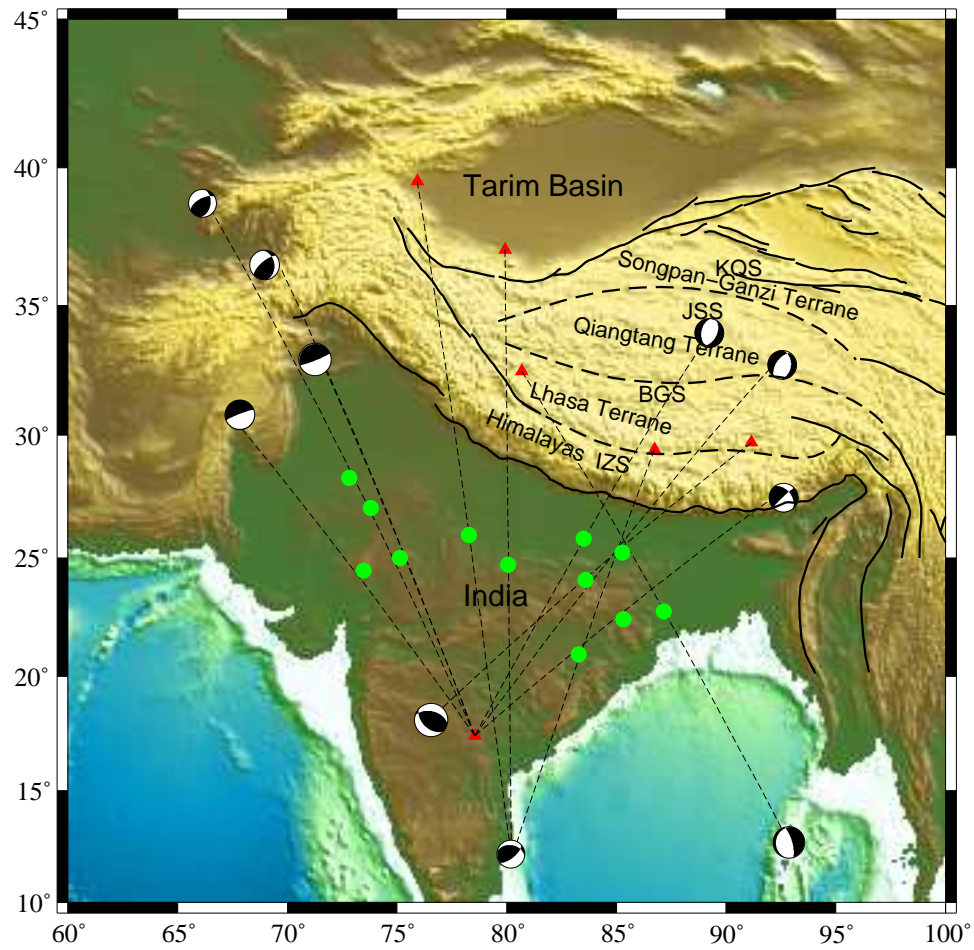


Figure 5.11: Event-station pairs used to obtain the upper-mantle velocity structure beneath India. Green dots are turning points.

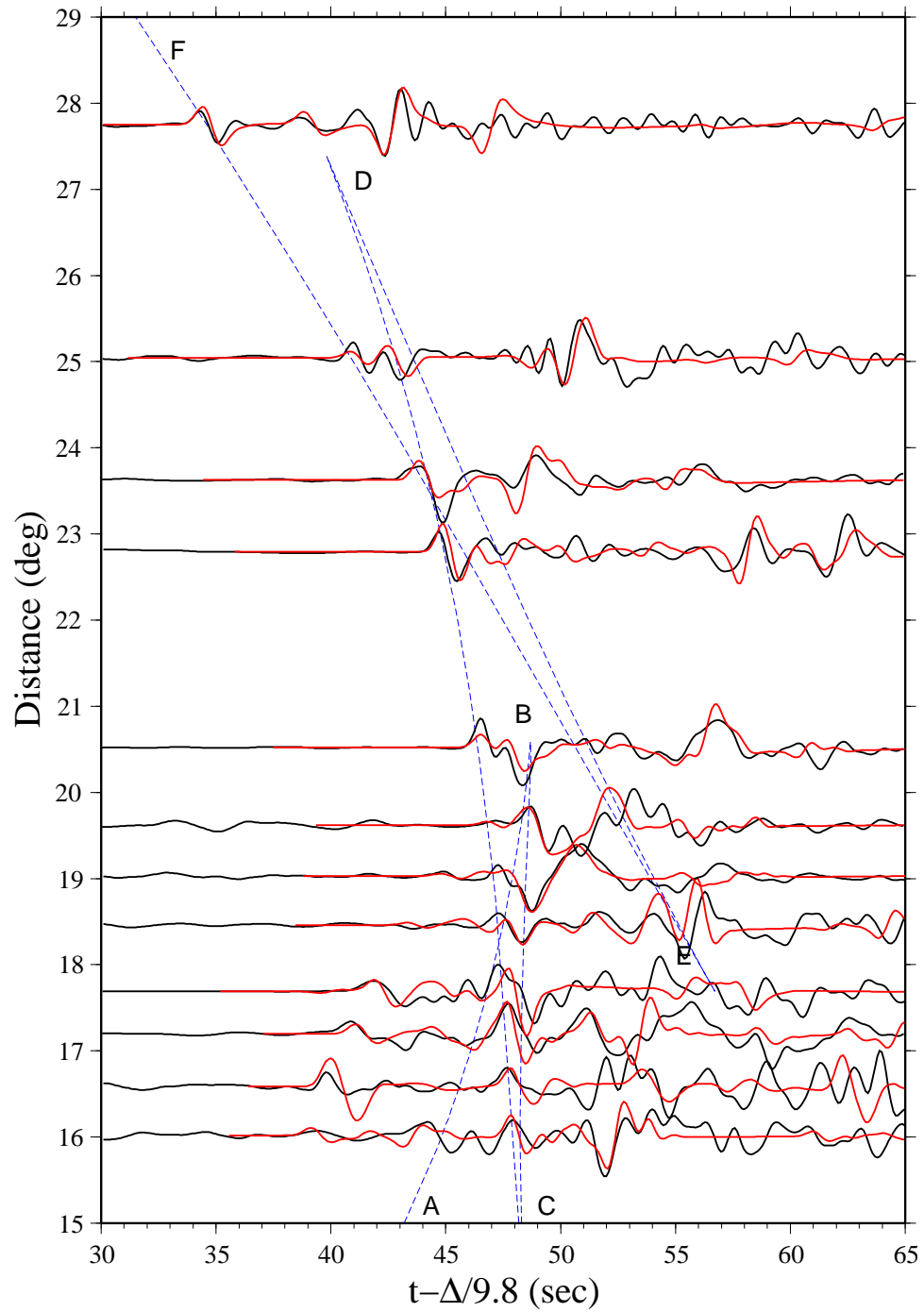


Figure 5.12: Waveform fits for India. Black-colored seismograms are observed data. Red traces are synthetic seismograms of the best 1-D model shown in Fig. 5.13. Blue lines represent arrival times predicted by the IASP91 model.

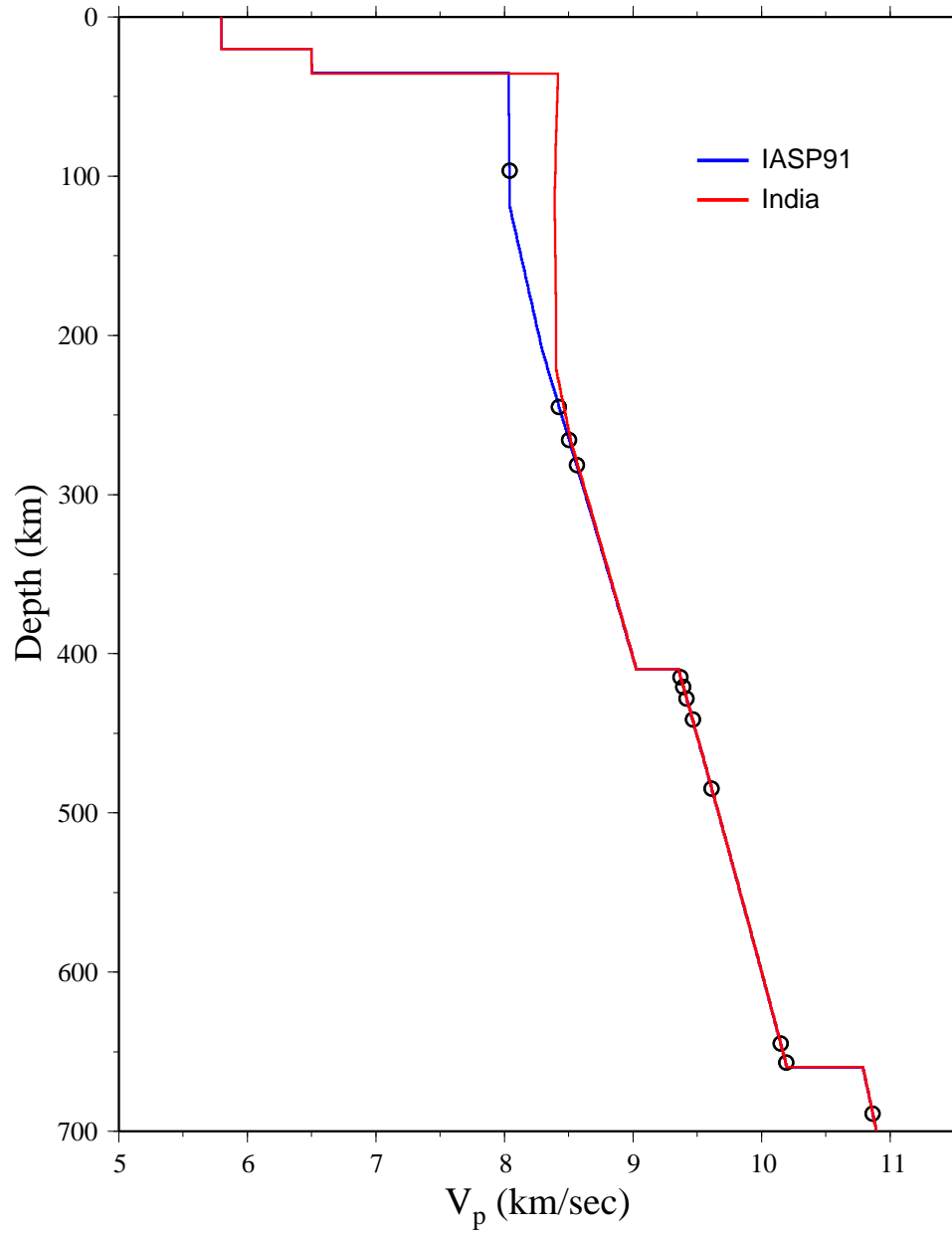


Figure 5.13: P -wave velocity model for India. Black circles represent the turning depths of the waveforms in Fig. 5.12.

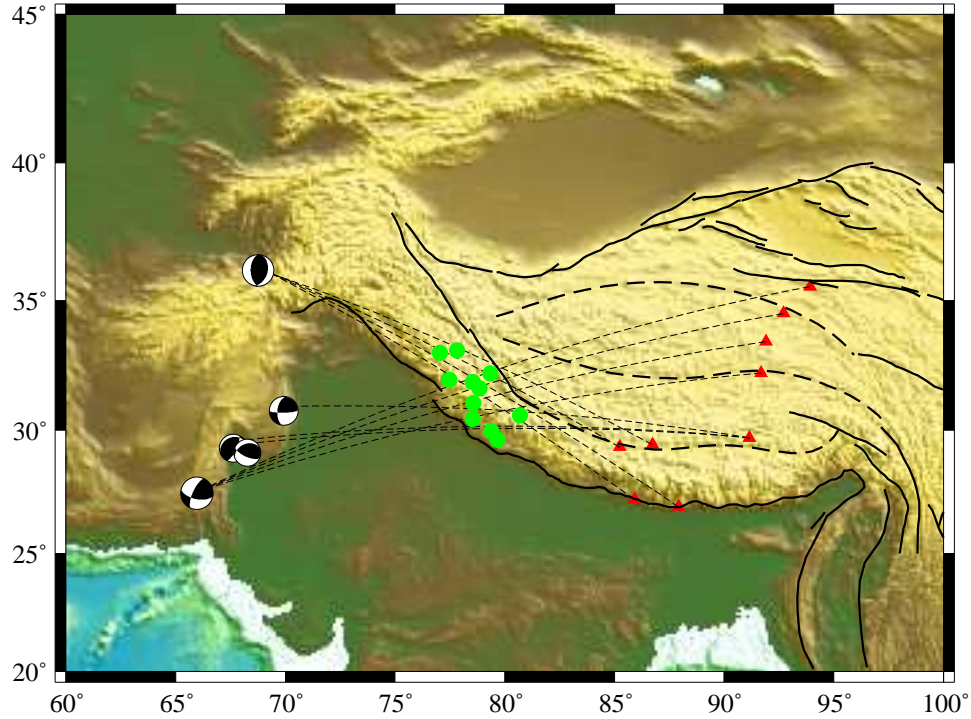


Figure 5.14: Event-station pairs used to obtain the upper-mantle velocity structure beneath the Himalayas.

in the bottom half of the transition zone. The velocity structure near the 410 discontinuity was also different from the global average model. The observed BC branch reached beyond 23° , but the predicted B-cusp of the IASP91 model ended around 20° (Fig. 5.23). The broader BC branch required a larger velocity jump at the 410 discontinuity. Since the velocity value below the 410 discontinuity was determined by the waveform modeling at large distances, I reduced the velocity above the discontinuity. The discontinuity was also moved 20 km shallower in order to fit the waveforms between distances of 16° and 18.5° (Fig. 5.24). A small discontinuity at a depth of 270 km with a velocity jump of 2.5% was needed to explain an additional triplication in the waveforms of the AB branch between 13° and 18° . The upper-mantle velocities above 270 km were higher than those of the IASP91 model but lower than those beneath the Lhasa Terrane and India.

The transition-zone velocity structure beneath the Songpan-Ganzi Terrane was

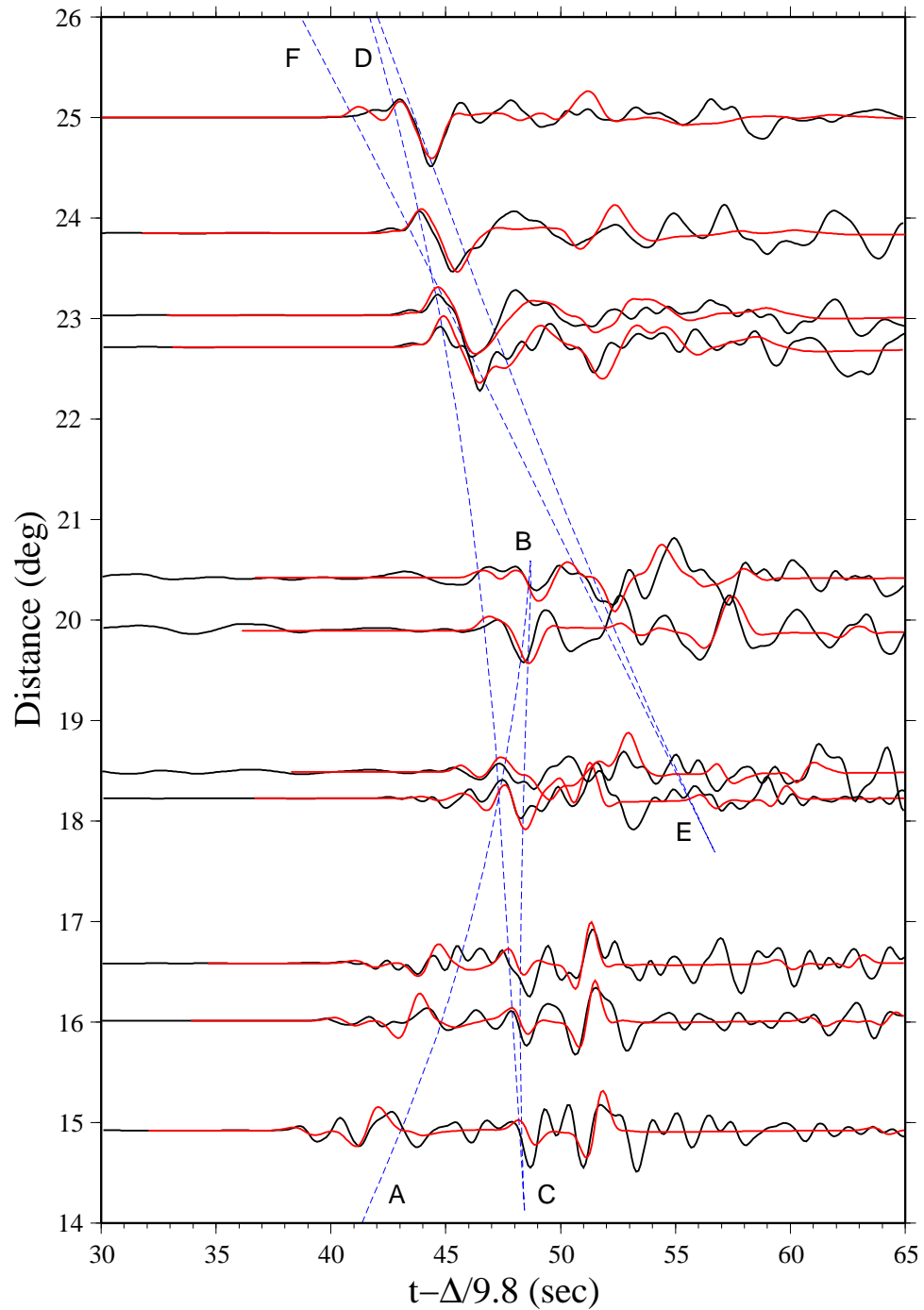


Figure 5.15: Waveform fits for the Himalayas. Black-colored seismograms are observed data. Red traces are synthetic seismograms of the best 1-D model shown in Fig. 5.16. Blue lines represent arrival times predicted by the IASP91 model.

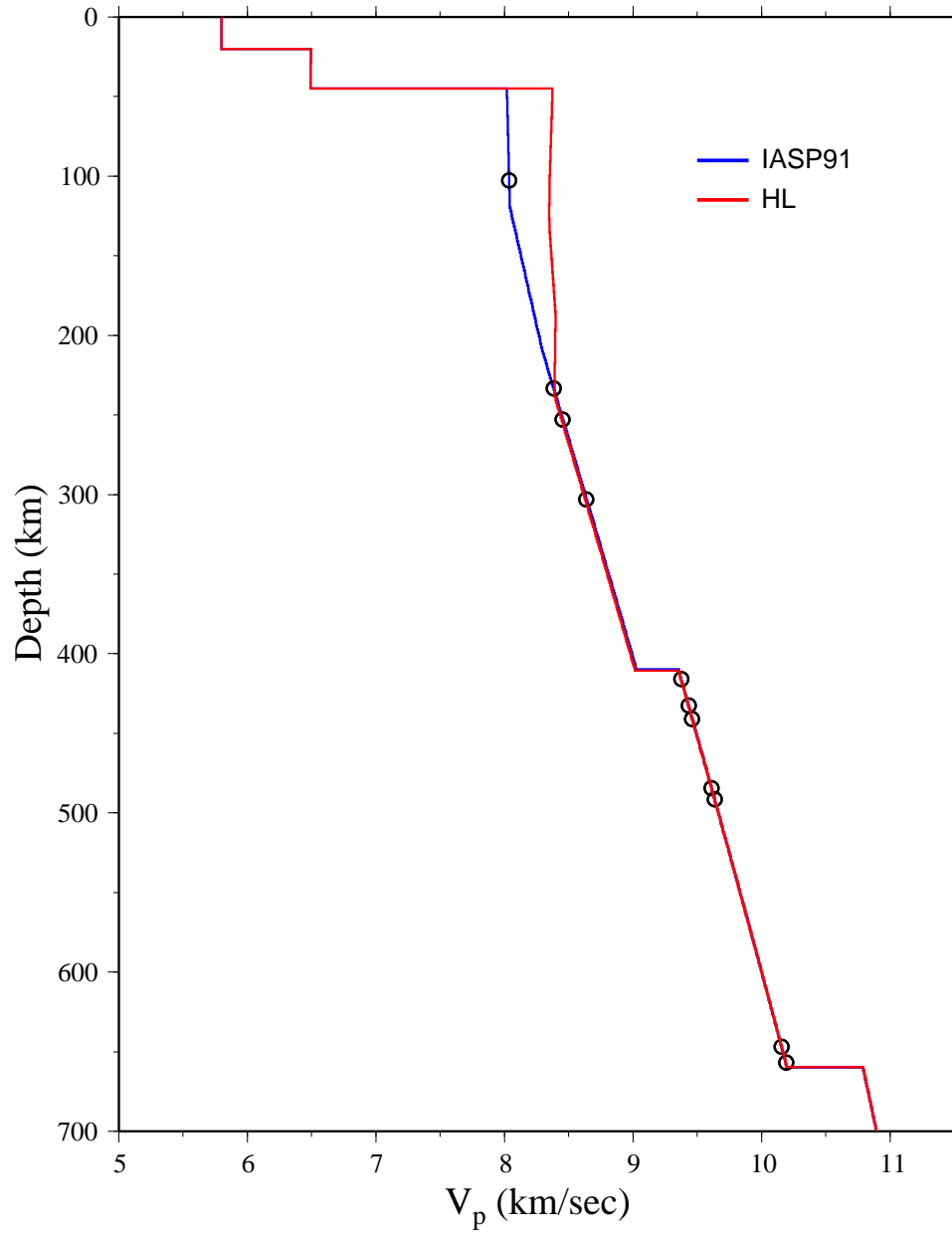


Figure 5.16: P -wave velocity model for the Himalayas. Black circles represent the turning depths of the waveforms in Fig. 5.15.

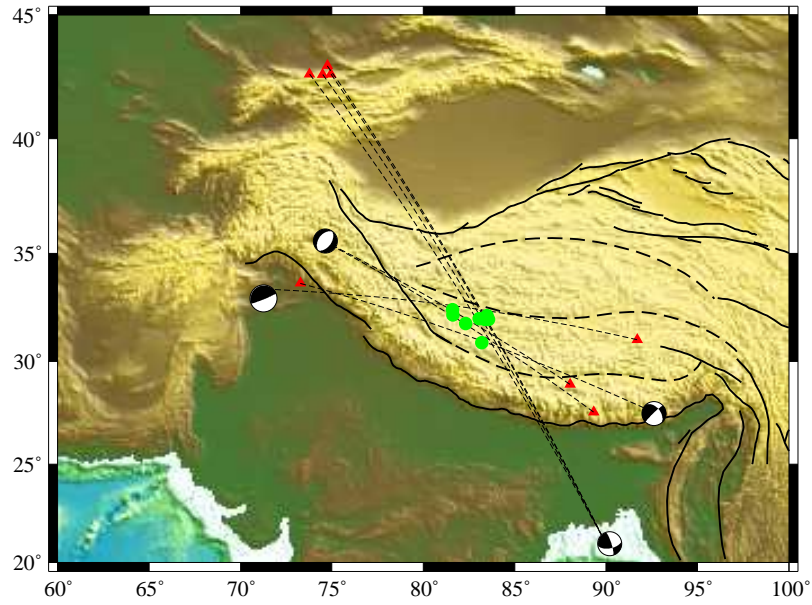


Figure 5.17: Event-station pairs used to obtain the upper-mantle velocity structure beneath the Lhasa Terrane.

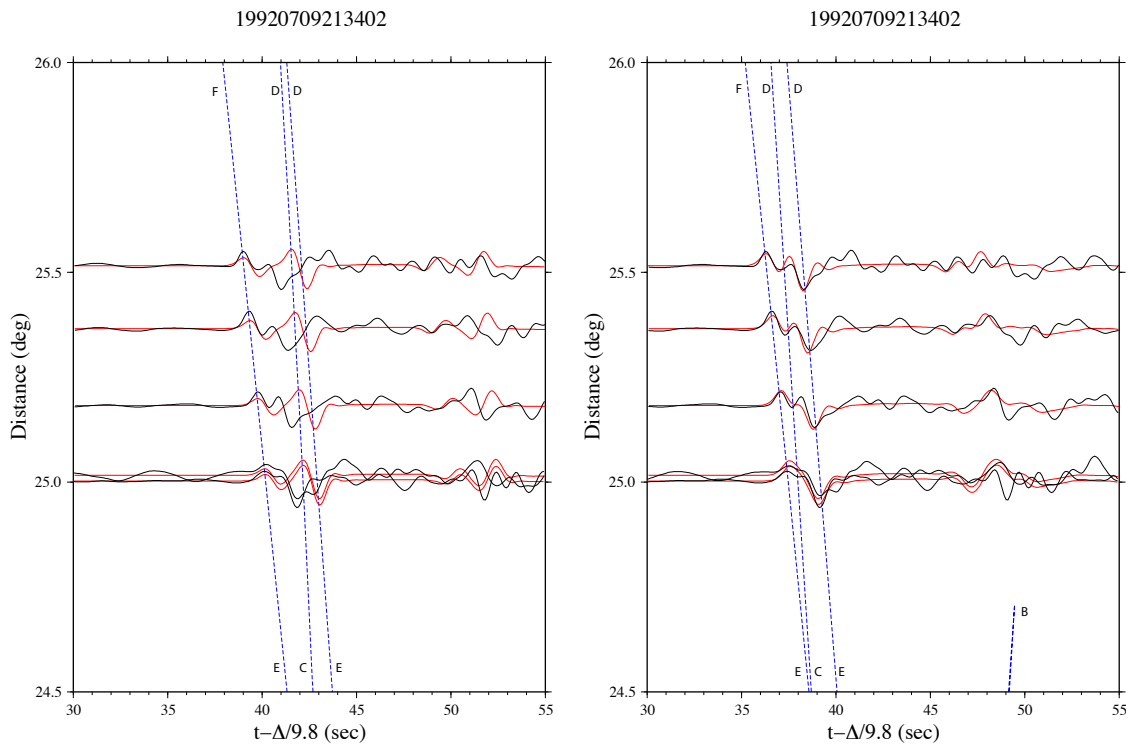


Figure 5.18: Arrival times (blue dashed lines) and synthetics (red-colored traces) predicted by the IASP91 model (left) and the best velocity model for the Lhasa Terrane (right).

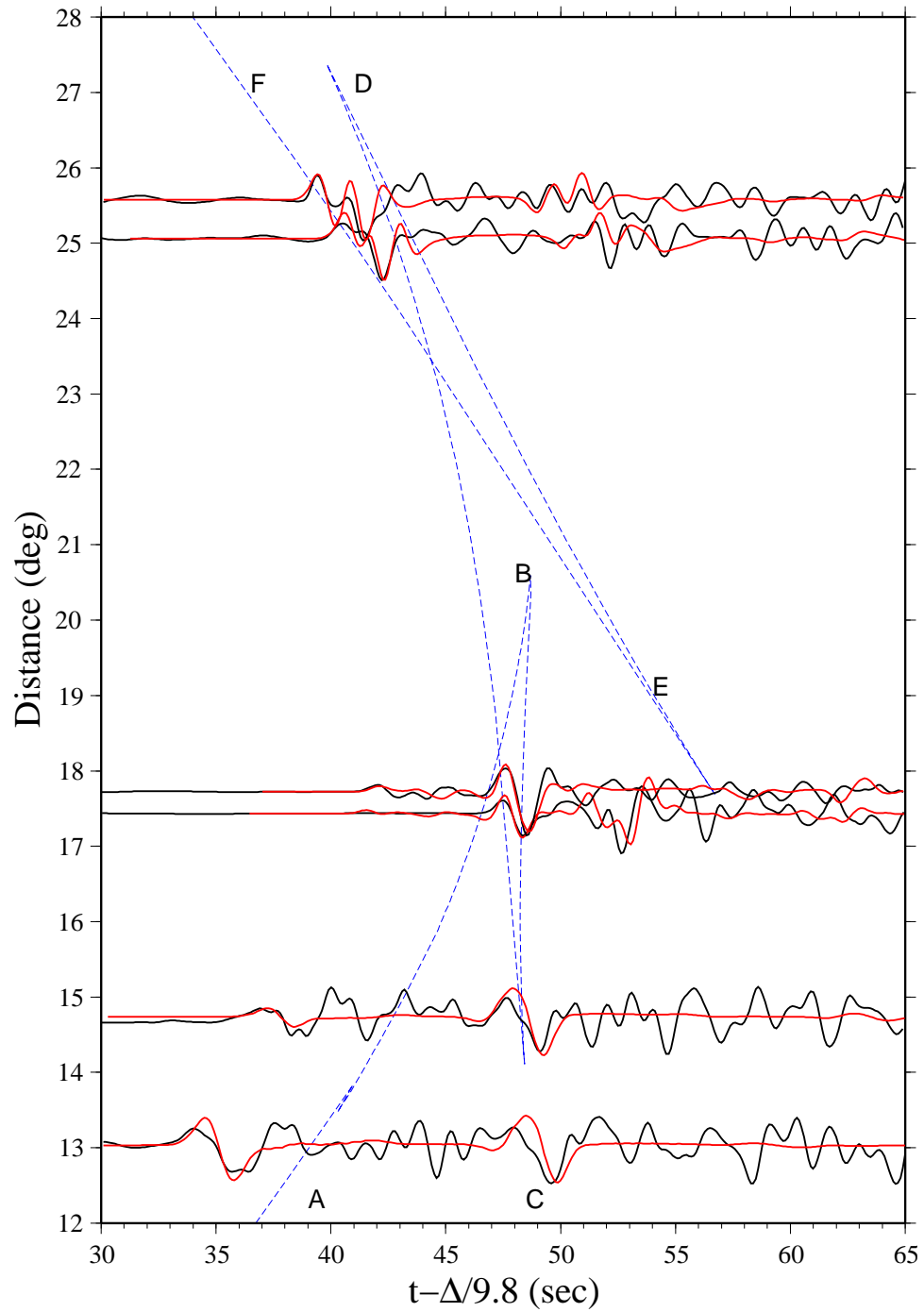


Figure 5.19: Waveform fits for the Lhasa Terrane. Black-colored seismograms are observed data. Red traces are synthetic seismograms of the best 1-D model shown in Fig. 5.20. Blue lines represent arrival times predicted by the IASP91 model.

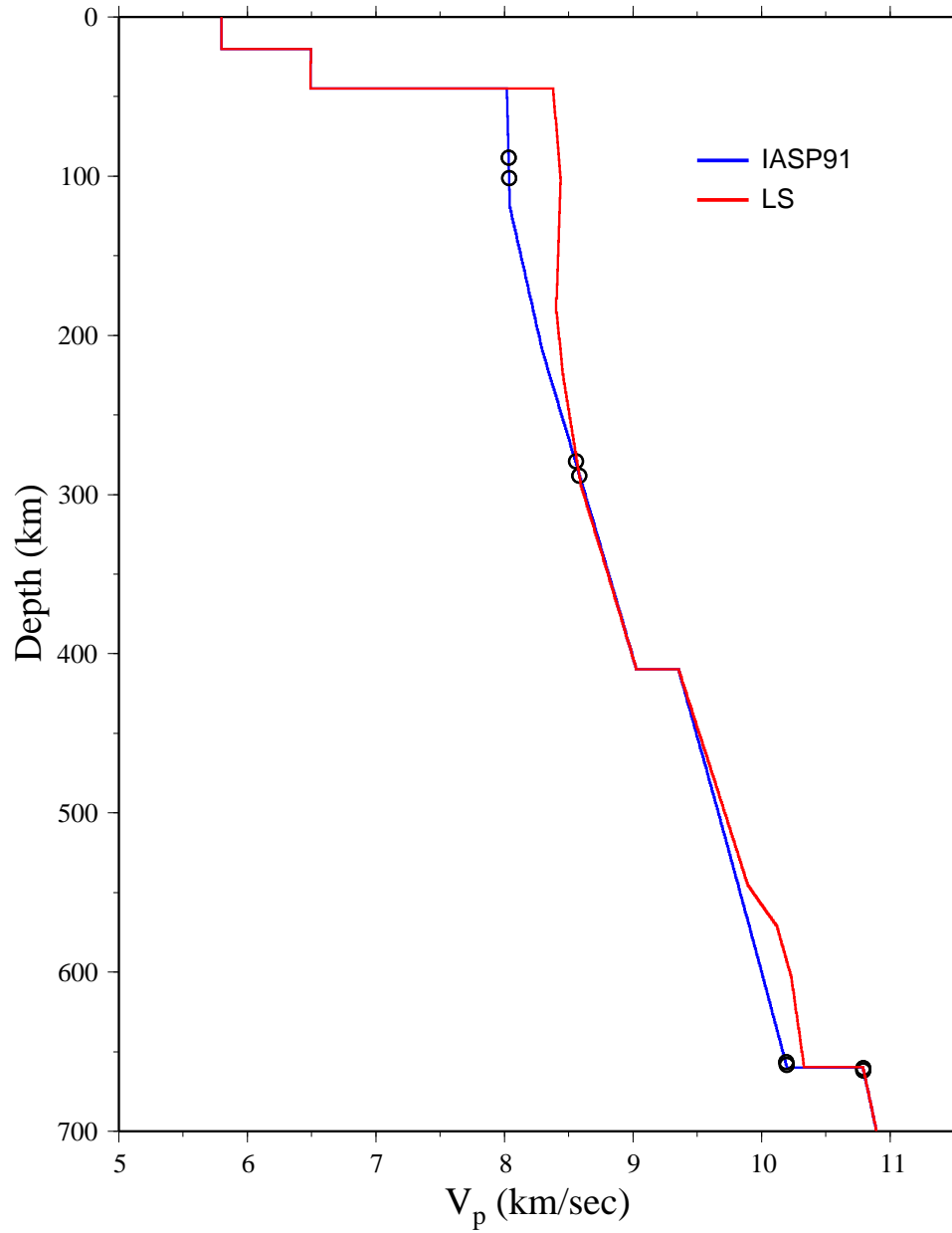


Figure 5.20: P -wave velocity model for the Lhasa Terrane. Black circles represent the turning depths of the waveforms in Fig. 5.19.

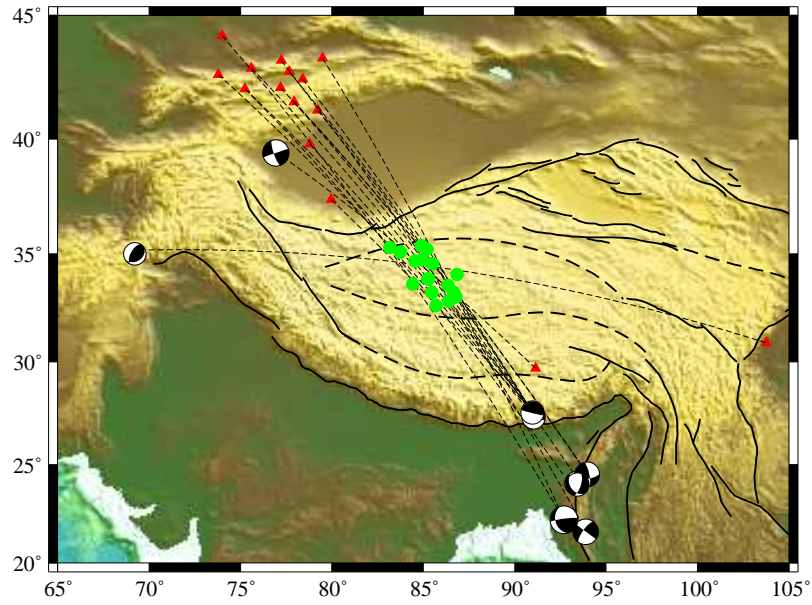


Figure 5.21: Event-station pairs used to obtain the upper-mantle velocity structure beneath the Qiangtang Terrane.

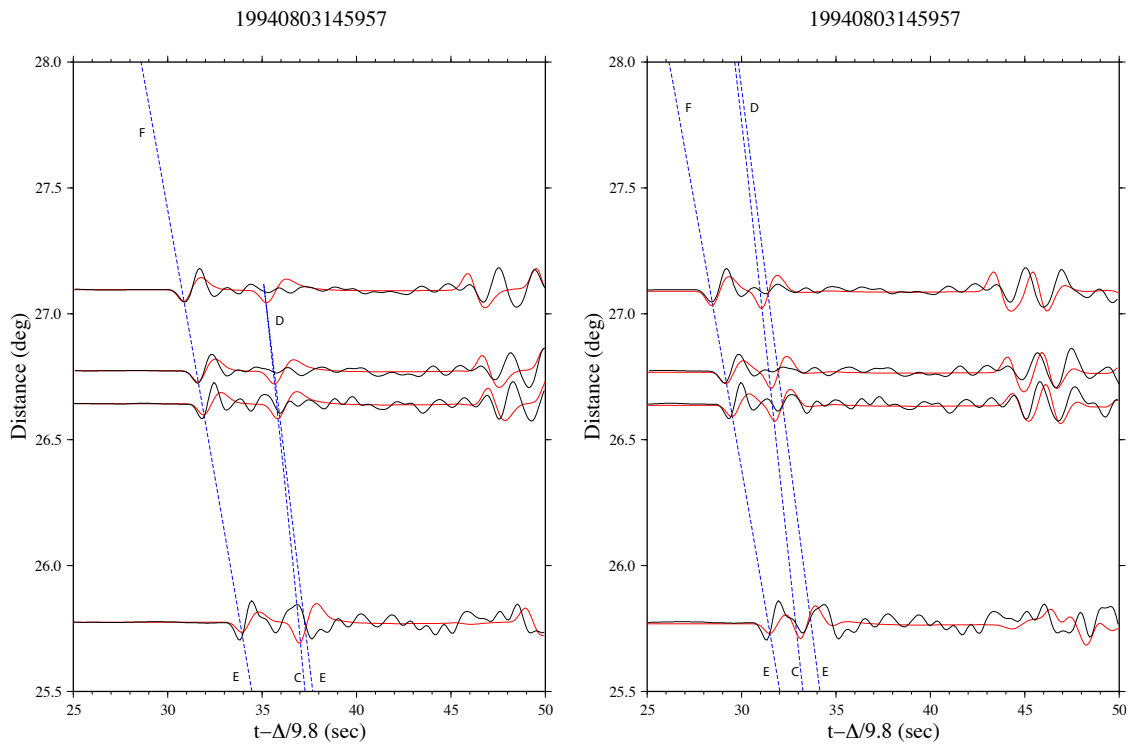


Figure 5.22: Arrival times (blue dashed lines) and synthetics (red-colored traces) predicted by the IASP91 model (left) and the best velocity model for the Qiangtang Terrane (right).

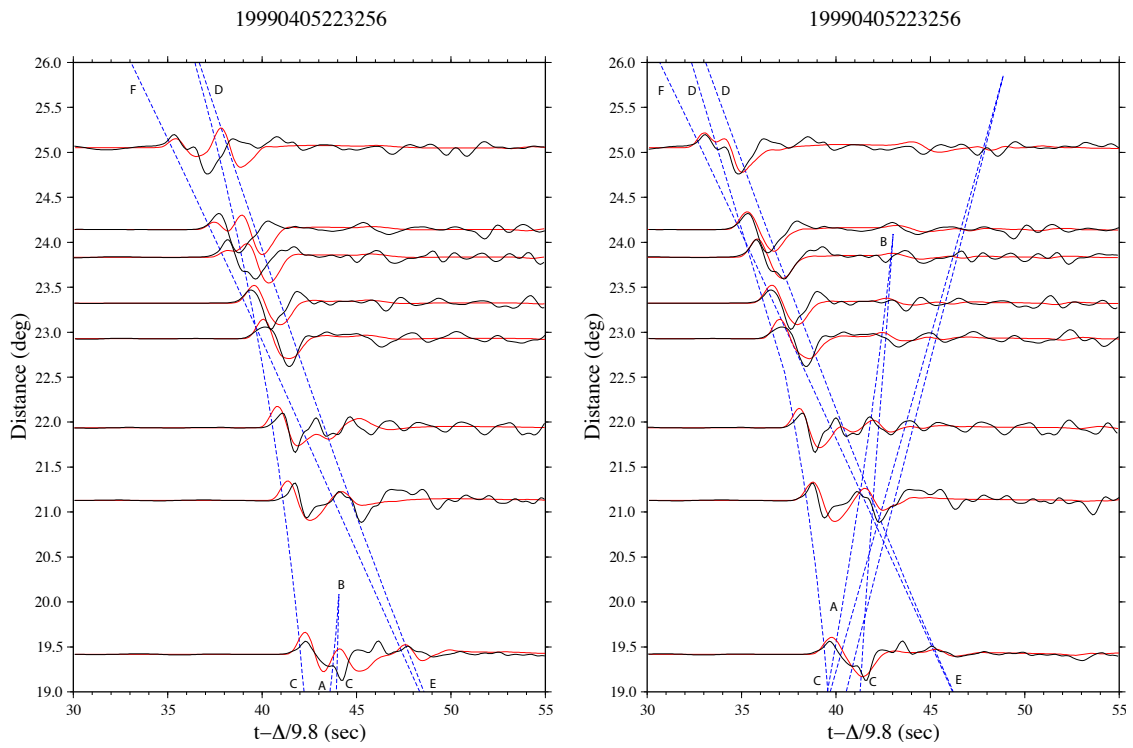


Figure 5.23: Arrival times (blue dashed lines) and synthetics (red-colored traces) predicted by the IASP91 model (left) and the best velocity model for the Qiangtang Terrane (right).

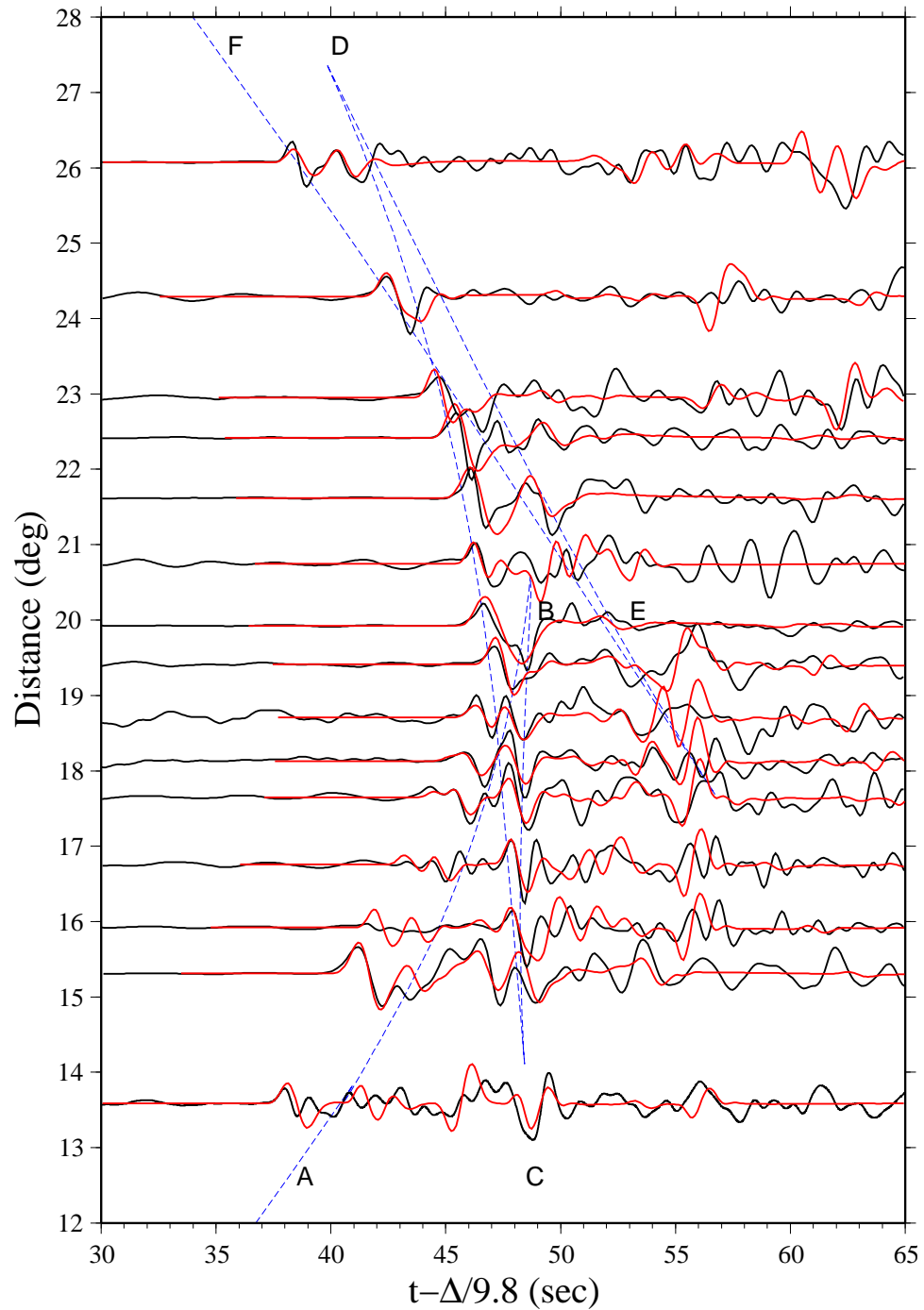


Figure 5.24: Waveform fits for the Qiangtang Terrane. Black-colored seismograms are observed data. Red traces are synthetic seismograms of the best 1-D model shown in Fig. 5.25. Blue lines represent arrival times predicted by the IASP91 model.

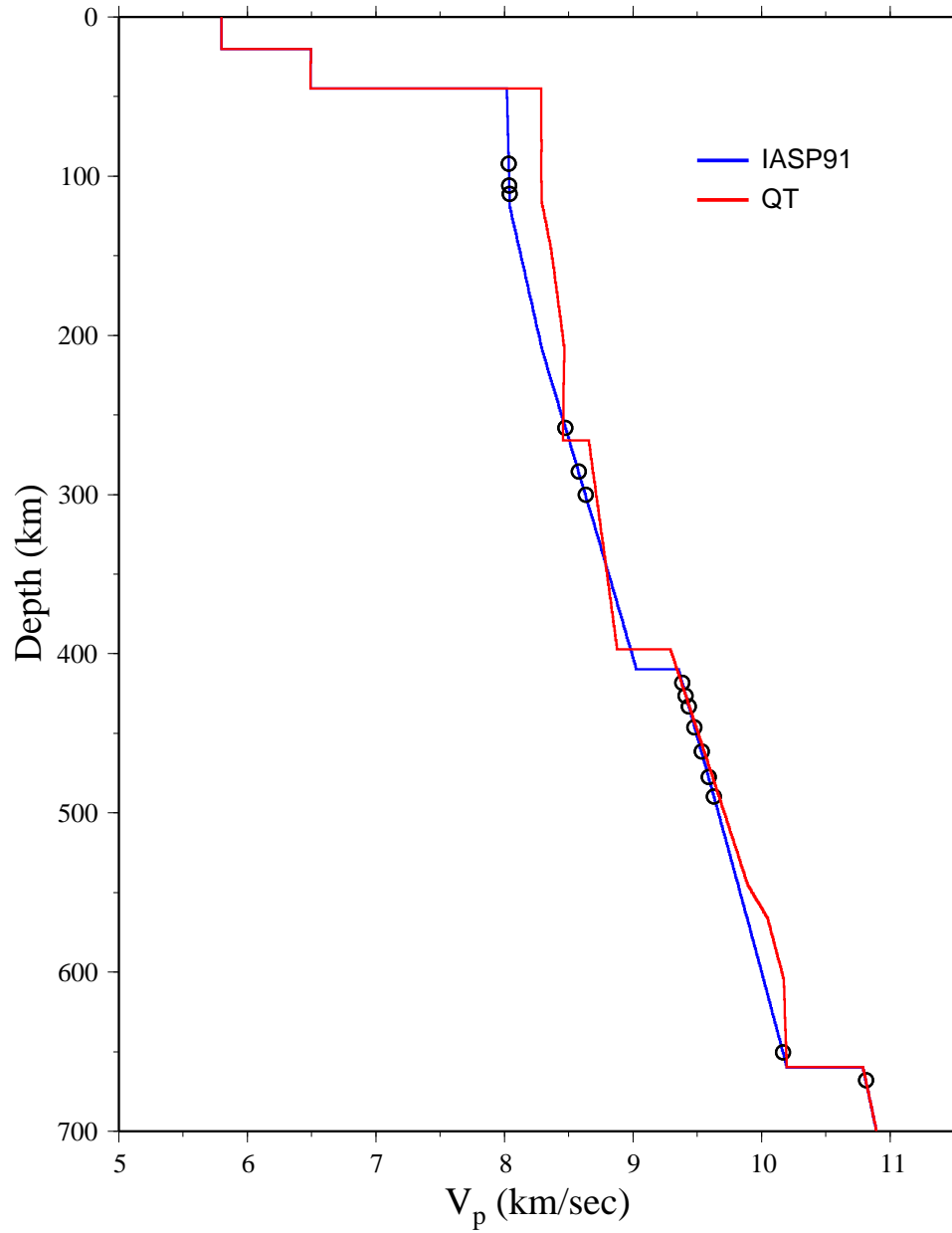


Figure 5.25: P -wave velocity model for the Qiangtang Terrane. Black circles represent the turning depths of the waveforms in Fig. 5.24.

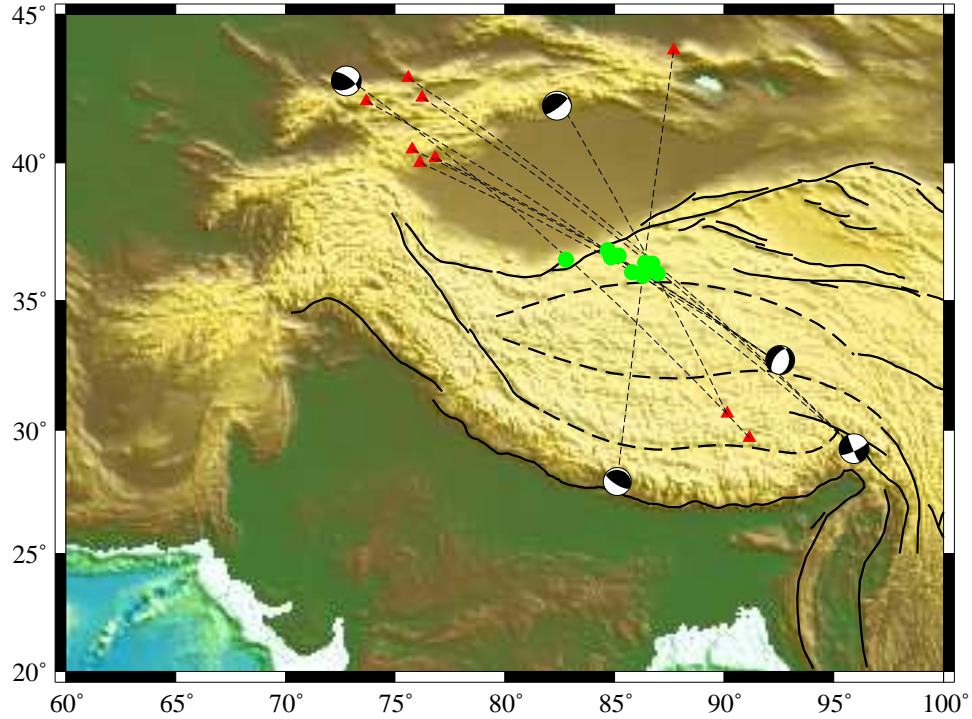


Figure 5.26: Event-station pairs used to obtain the upper-mantle velocity structure beneath the Songpan-Ganzi Terrane.

the same as the IASP91 model. No high-velocity anomaly was detected. It had a 410 discontinuity velocity structure similar to that of the Qiangtang Terrane, with a shallow 410 and a reduced velocity above it. This was also due to a broad BC branch in the observed waveforms in the distance range of 20° to 22° (Fig. 5.28). However, in order to fit the waveforms between 12° and 17° , a low-velocity layer between the depths of 100 to 180 km was needed (Fig. 5.29).

Finally, the upper-mantle velocity structure beneath the Tarim Basin was obtained by modeling 10 waveforms with turning points beneath the region (Fig. 5.30). The waveform fits of large distances beyond 19° indicated that the transition-zone velocity structure was the same as the global average model. However, the AB branch was about 2 sec earlier than predicted by the IASP91 model. This required a high-velocity lid about 150 km thick in the top of the upper mantle, with a P_n velocity of 8.22 km/s (Fig. 5.32).

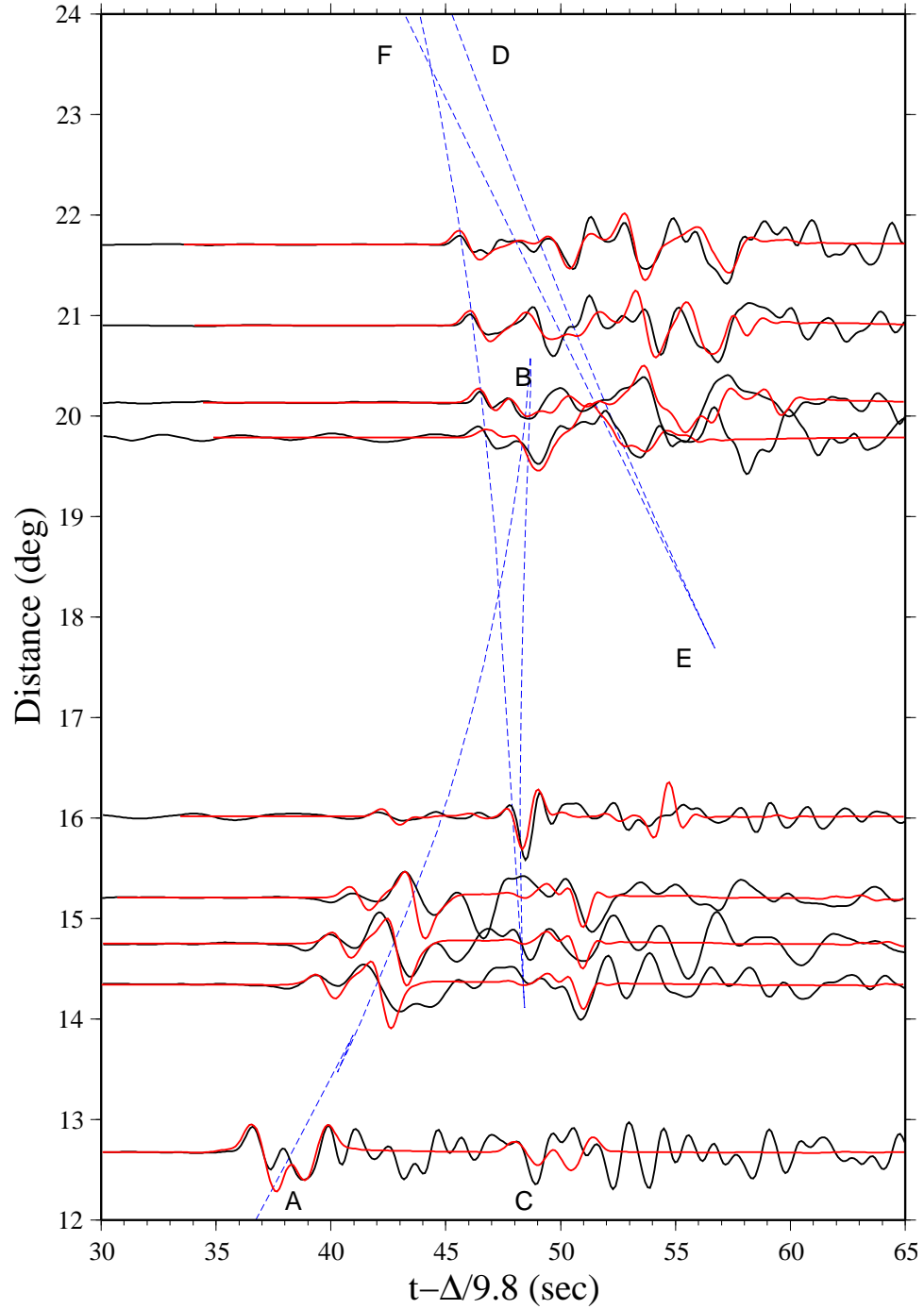


Figure 5.27: Waveform fits for the Songpan-Ganzi Terrane. Black-colored seismograms are observed data. Red traces are synthetic seismograms of the best 1-D model shown in Fig. 5.29. Blue lines represent arrival times predicted by the IASP91 model.

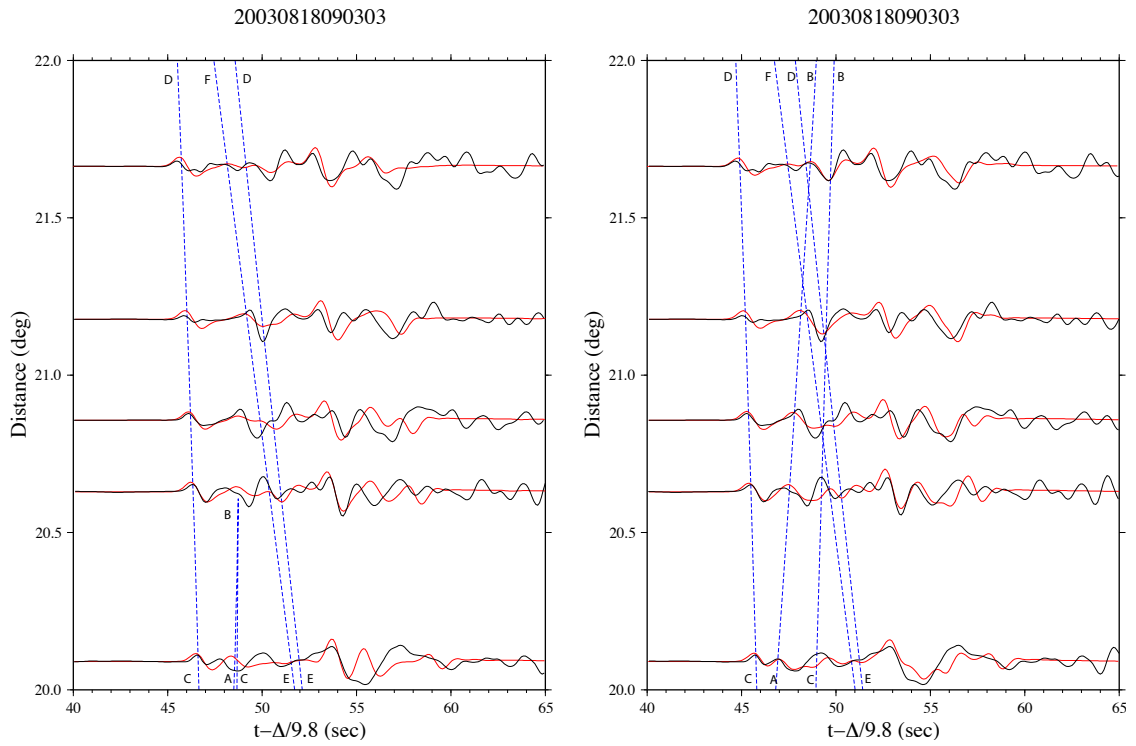


Figure 5.28: Arrival times (blue dashed lines) and synthetics (red-colored traces) predicted by the IASP91 model (left) and the best velocity model for the Songpan-Ganzi Terrane (right).

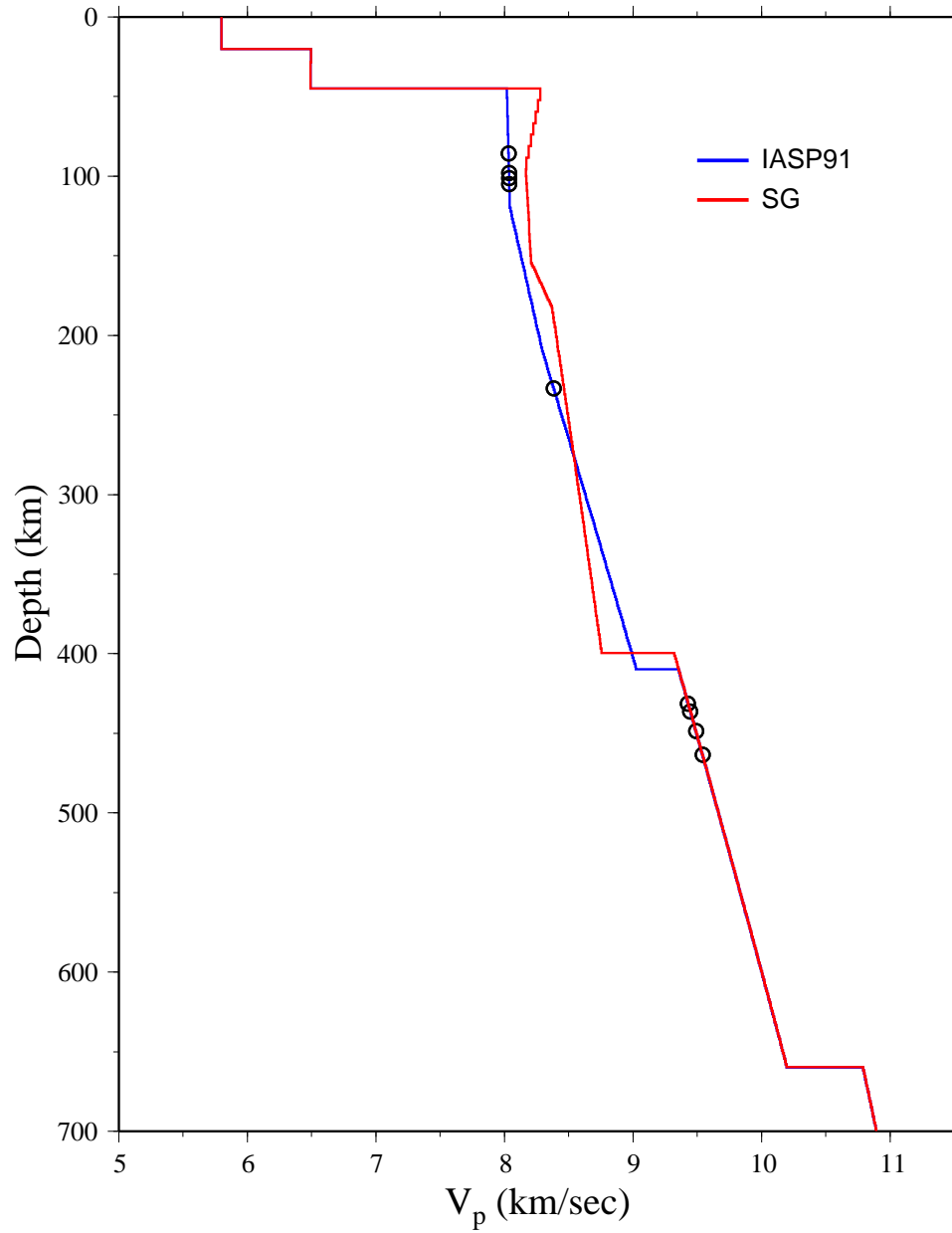


Figure 5.29: P -wave velocity model for the Songpan-Ganzi Terrane. Black circles represent the turning depths of the waveforms in Fig. 5.27.

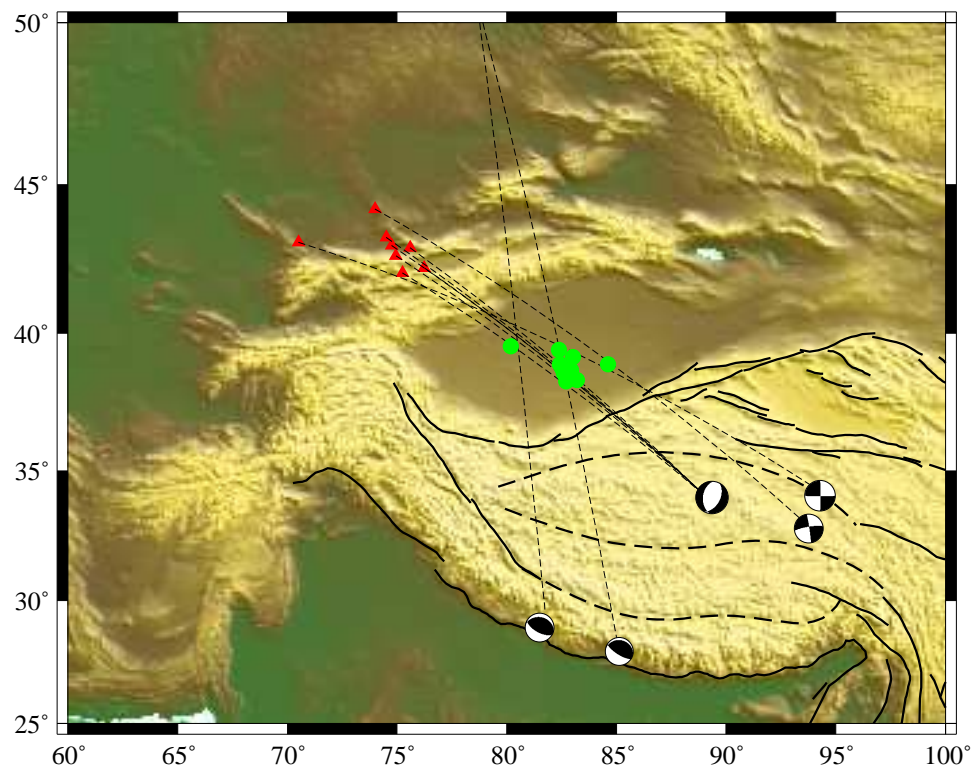


Figure 5.30: Event-station pairs used to obtain the upper-mantle velocity structure beneath the Tarim Basin.

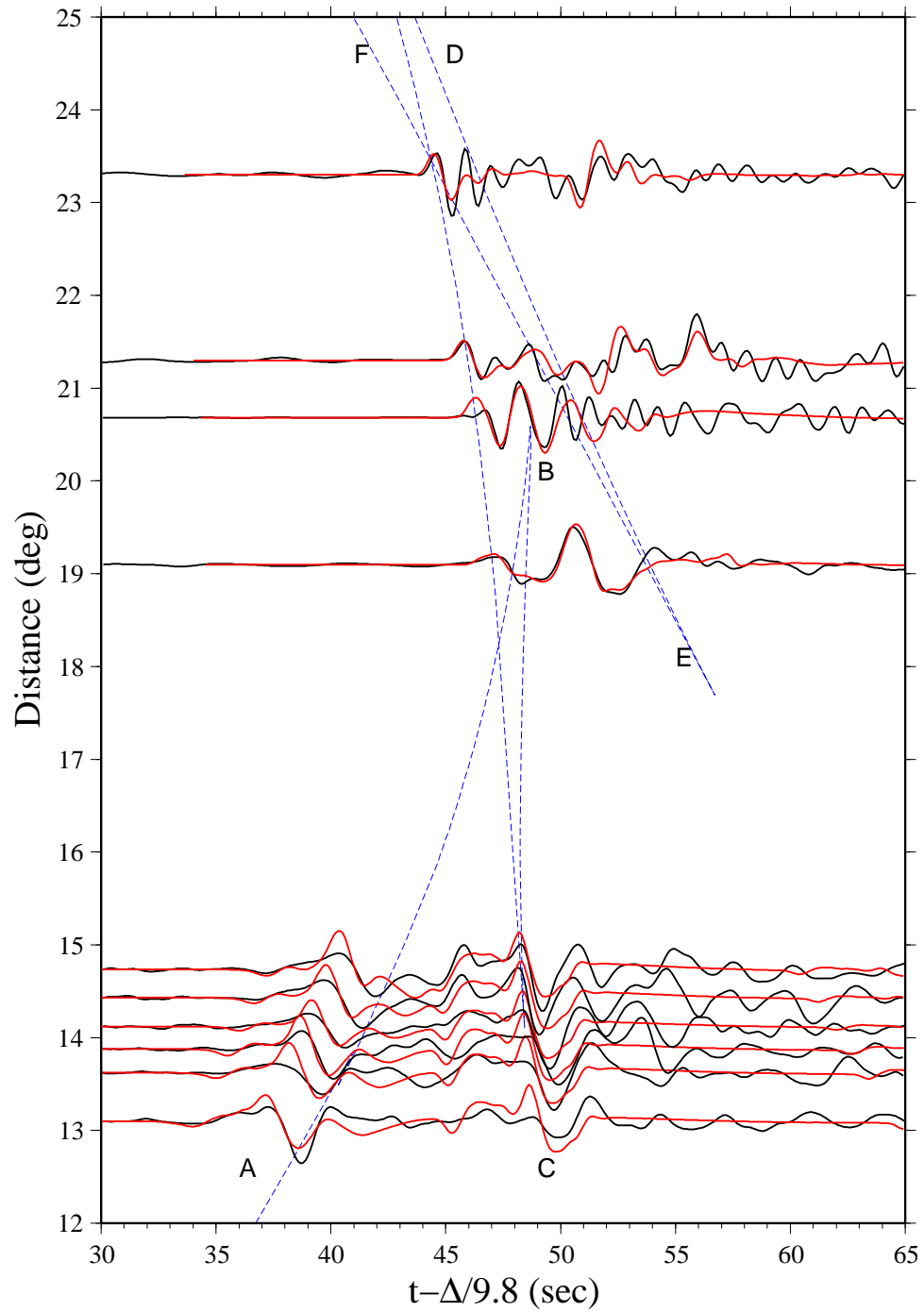


Figure 5.31: Waveform fits for the Tarim Basin. Black-colored seismograms are observed data. Red traces are synthetic seismograms of the best 1-D model shown in Fig. 5.32. Blue lines represent arrival times predicted by the IASP91 model.

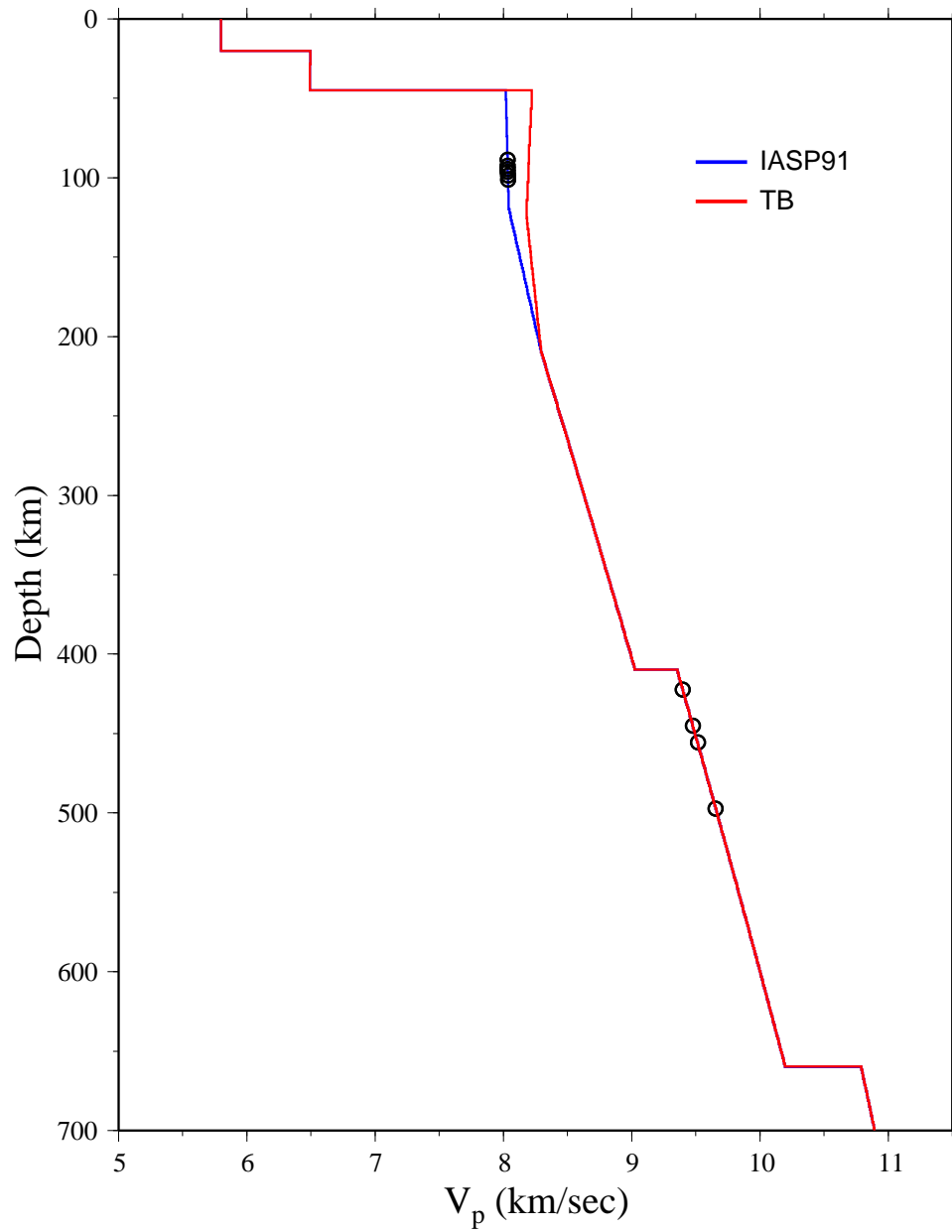


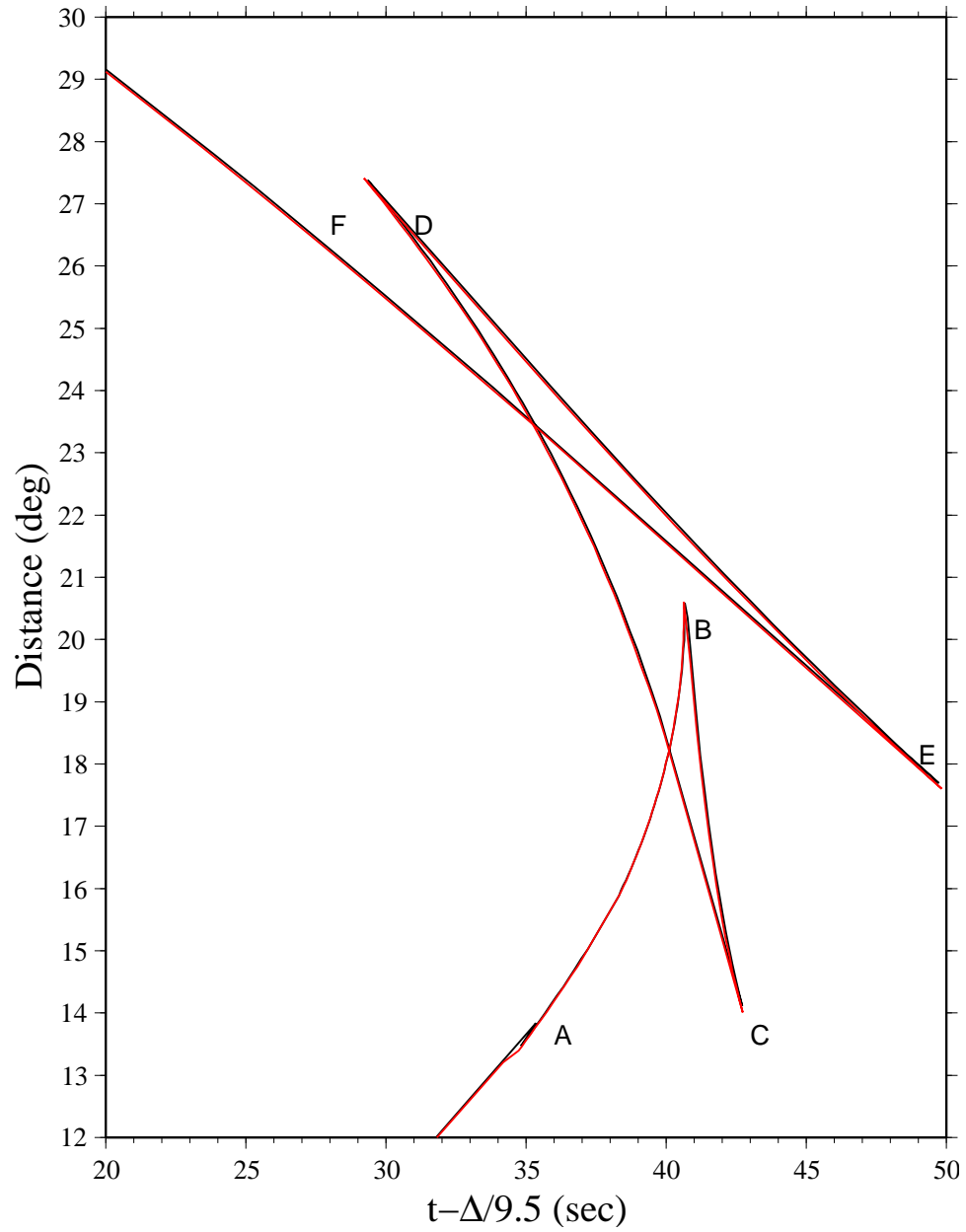
Figure 5.32: P -wave velocity model for the Tarim Basin. Black circles represent the turning depths of the waveforms in Fig. 5.31.

Chapter 6: Discussion and Conclusions

6.1 Uncertainties of the upper-mantle velocity structure

In this study, the waveforms in the upper-mantle distances were filtered using a bandpass filter between the frequencies of 0.02 Hz and 1.0 Hz. Thus, the shortest wavelength of the signals was about 8–10 km. Using the quarter-wavelength rule, I estimated that the waveform data had a vertical resolution power of 2–3 km. This was 1–2 order of magnitudes higher than resolution of travel-time tomography (>50 km) and surface-wave studies (>100 km). The horizontal resolution of my results depended on station and earthquake distributions. In regions such as the Lhasa and Qiangtang Terranes, which were sampled by abundant seismic rays, waveforms of turning points separated by less than 4° were grouped together for modeling. The corresponding horizontal resolution was 400–500 km. In other regions like India and the Tarim Basin where data were scarce, the whole tectonic block was treated as one unit.

Uncertainties of the velocity models came from several sources, including the ignoring of lateral velocity structural variations in the crust, earthquake epicenter mislocations, and earthquake depth errors. Although all the focal depths of the earthquakes used were determined using the differential travel times between the direct P and the depth phases at teleseismic distances, a depth uncertainty of 2–3 km was believed to exist since a 1-D velocity model was used. To estimate the effect of source depth uncertainties on the modeling results, I calculated travel-time triplications from a 10-km-deep earthquake and a 15-km-deep earthquake (Fig. 6.1). After removing the arrival-time delay due to different source depths, the two triplications were almost identical. This indicated that a difference of 5 km in event depth caused less than 0.1 sec in differential arrival times. Such a small error can be safely ignored.



Travel-time triplications for a 10-km-deep earthquake (black lines) and a 15-km-deep earthquake (red lines). The red line is shifted by 0.65 sec to account for the delay caused by the source depth difference.

6.2 Comparison of the upper-mantle velocity structures with results from previous studies

The waveform modeling results showed that a high-velocity lid exists beneath India, the Himalayas, the Lhasa Terrane, and the Tarim Basin. Both India and Tarim are Archean cratons and are believed to lie over a cold and strong mantle lithosphere. Travel-time tomography studies suggested a high-velocity anomaly down to 250–300 km beneath India (VAN DER VOO, 1999; REPLUMAZ *et al.*, 2004; ZHOU and MURPHY, 2005; LI *et al.*, 2006; HUANG and ZHAO, 2006). A thick high-velocity upper mantle lid was also suggested by LYON-CAEN (1986) using SH -wave triplication between 10° and 30° . P_n travel-time studies showed that the P_n velocity beneath India was 8.40 km/s (BARAZANGI and NI, 1982; NI and BARAZANGI, 1983). LEBEDEV and VAN DER HILST (2008) obtained a global S -wave velocity model by modeling surface and S -wave seismograms. In their model, high-velocity features dominated the upper mantle beneath the Tibetan Plateau. At the 200 km depth, high-velocity anomalies as large as 5% could be seen in the Himalayas and the Lhasa Terrane. Existing results of the upper-mantle velocity structure beneath the Tarim Basin are controversial. Surface-wave dispersion and some travel-time tomographic results indicated that upper-mantle velocities beneath the Tarim Basin were slow (CURTIS *et al.*, 1998; LI *et al.*, 2006; LEBEDEV and VAN DER HILST, 2008), while other travel-time tomography studies suggested high velocities (LIU *et al.*, 2004; ZHOU and MURPHY, 2005). YAO *et al.* (2005) used inter-station Rayleigh-wave dispersions and found lateral velocity variations beneath the basin. The northeastern Tarim had higher upper-mantle velocities than the southwestern Tarim. My waveform modeling did not reveal such a lateral variation. The 8.22 km/s P velocity at the top of the mantle agreed with the P_n velocity from the travel-time tomographic result (MCNAMARA *et al.*, 1997).

The upper-mantle velocities above 200 km beneath the Qiangtang and

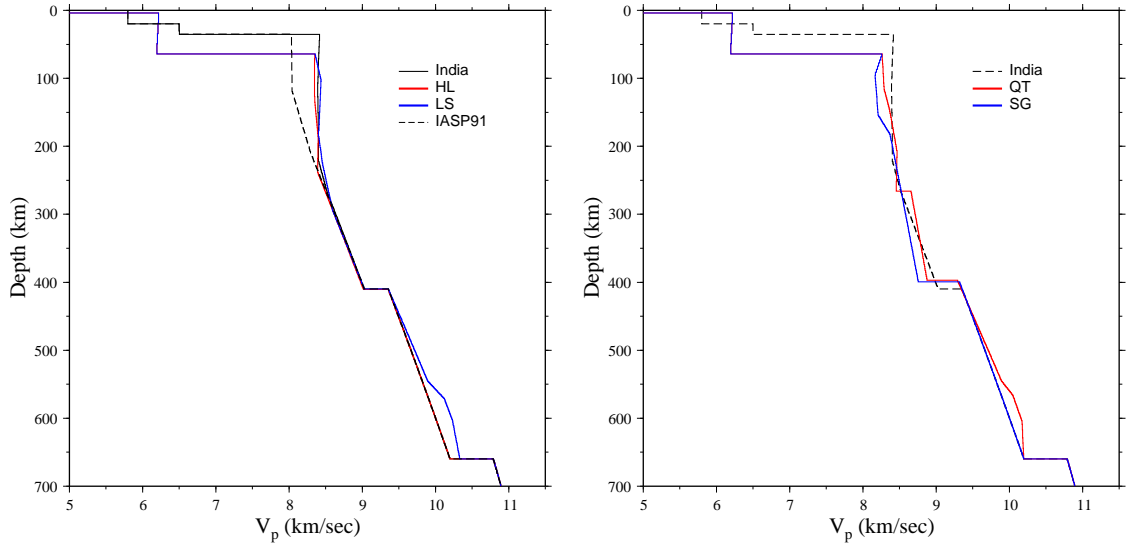


Figure 6.1: Left panel compares upper-mantle velocity models in India, the Himalayas (HL), and the Lhasa Terrane (LS). Right panel shows comparison of velocity models in the Qiangtang Terrane (QT) and the Songpan-Ganzi Terrane (SG) with the model of India.

Songpan-Ganzi Terranes are lower than in its north and south, especially beneath the Songpan-Ganzi Terrane where a low-velocity zone exists (Fig. 6.1). The results agree with previous S_n and P_n studies that showed a region of inefficient S_n propagation and low P_n velocities in northern-central Tibet (NI and BARAZANGI, 1983; MCNAMARA *et al.*, 1997). Cenozoic volcanism was also discovered in this region (GANSER, 1980).

6.3 Implications

Based on the results from waveform modeling, an upper-mantle structural cross-section along a N-S profile across the Tibetan Plateau can be sketched (Fig. 6.2). Since the upper-mantle velocity structures beneath the Himalayas and the Lhasa Terrane are similar to those beneath India, I suggest that the Indian mantle lithosphere thrusts beneath the Tibetan Plateau as far as to the Bangong-Nujiang Suture. The high velocity anomalies in the transition zone

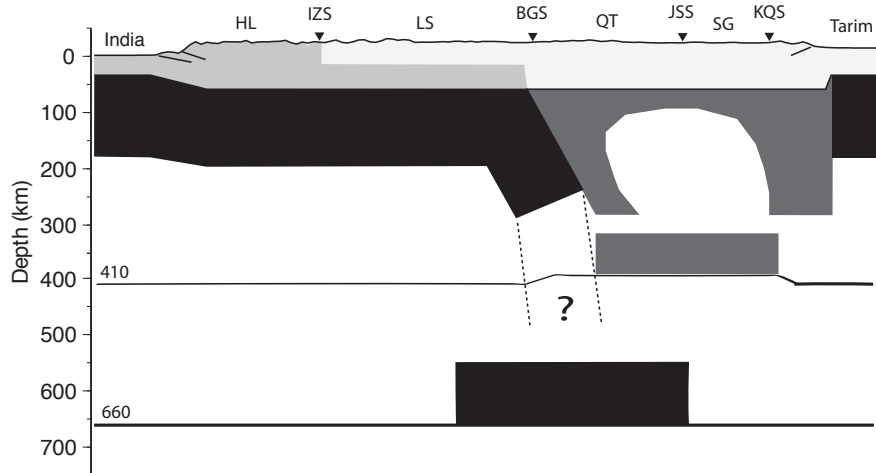


Figure 6.2: Collision model for the India-Eurasia convergence. The black block sitting atop of the 660 discontinuity represents the remnants of the subducted Indian lithosphere. The dark-gray box above the 410 discontinuity is the detached Eurasian mantle lithosphere. HL: the Himalayas, IZS: the Indus-Zangbo Suture, LS: the Lhasa Terrane, BGS: the Bangong Suture, QT: the Qiangtang Terrane, JSS: the Jingsha Suture, SG: the Songpan-Ganzi Terrane, KQS: the Kunlun-Qinling Suture.

beneath the Lhasa and Qiangtang Terranes were interpreted as the remnants of the subducted Indian slab. It is not clear whether they are still connected to the Indian lithosphere or have been detached. Answering this question requires much greater horizontal resolution. The low velocities between the depths of 100 and 200 km under the Qiangtang and Songpang-Ganzi Terranes were caused by the delamination of a portion of the thickened Asian lithosphere due to a thermal instability and/or small-scale mantle convections. Some of the delaminated lithosphere is now resting on top of the 410 discontinuity and produces the velocity jump at the depth of 270 km beneath the Qiangtang and the Songpang-Ganzi Terranes. It also lowers the temperatures of the 410 discontinuity and causes the discontinuity to be elevated by 20 km.

A similar elevated 410 discontinuity was found by receiver function studies by KIND *et al.* (2002), who interpreted it as a product of the upwelling mantle materials. However, upwelling of hot material should increase the 410 discontinuity

depth due to the positive Clapeyron slope of the mineral phase change associated with the discontinuity. In another study using SS precursors bouncing beneath the Tibetan Plateau, DEUSS and WOODHOUSE (2001) found a velocity discontinuity at the depth of 550 km beneath the area. They suggested that the velocity increase was due to a mineral phase change from wadsleyite (β -phase) to ringwoodite (γ -phase). This interpretation, however, does not explain why the discontinuity only exists beneath the Lhasa and Qiangtang Terranes. I believe that my Indian slab remnant interpretation is more plausible.

6.4 Conclusions

In summary, I have developed a new method to retrieve source time functions and determine focal depth using teleseismic P -wave waveforms. By applying it to earthquakes between 1990 and 2005 in and around the Tibetan Plateau, I obtained source time functions and depths of 504 events. Comparison with the Harvard CMT solutions showed that Harvard CMT catalog systematically over-estimated both the source durations and depths.

By fitting P waveforms in the distance range between 12° and 30° , I obtained upper-mantle velocity models beneath six regions along a N-S profile across the Tibetan Plateau. The results show that the upper-mantle velocity structures beneath India, the Himalayas and the Lhasa Terrane are similar and contain a high-velocity lid about 250 km thick. The Tarim Basin also lies above a high-velocity upper-mantle lid. The upper-mantle velocities over 200 km beneath the Qiangtang and Songpan-Ganzi Terranes are lower than those in the north and south, especially beneath the Songpan-Ganzi Terrane. The 410 discontinuity beneath these two terranes are elevated by 20 km. I also found high-velocity anomalies in the transition zone below 500 km under the Lhasa and Qiangtang Terranes. The results suggest that the Tibetan Plateau was generated by the

thrusting of the Indian mantle lithosphere under the southern part of Tibet. A portion of the thickened Asian lithosphere in northern Tibet was delaminated and is now sitting atop of the 410 discontinuity below it. The high-velocity anomalies in the transition zone beneath the Lhasa and Qiangtang Terranes are probably the remnants of subducted Indian lithosphere.

References

- ALSDORF, D., MAKOVSKY, Y., ZHAO, W., BROWN, L. D., NELSON, K. D., *et al.* (1998), *INDEPTH (International Deep Profiling of Tibet and the Himalaya) multichannel seismic reflection data: Description and availability*. J. Geophys. Res. *103*, 26993–26999.
- ARGAND, E. (1924), *La tectonique de l'Asie*. Proceedings of the 13th Int. Geol. Congr., Brussels 7, 171–372.
- ARVIDSSON, R., and EKSTRÖM, G. (1998), *Global CMT analysis of moderate earthquakes, $M_w \geq 4.5$, using intermediate-period surface waves*. Bull. Seismol. Soc. Am. *88*, 1003–1013.
- BARAZANGI, M., and NI, J. (1982), *Velocities and propagation characteristics of P_n and S_n beneath the Himalayan arc and Tibetan Plateau: Possible evidence for underthrusting of Indian continental lithosphere beneath Tibet*. Geology *10*, 179–185.
- BASSIN, C., LASKE, G., and MASTERS, G. (2000), *The current limits of resolution for surface wave tomography in North America*. Eos Trans. AGU *81*.
- BECKERS, J., SCHWARTZ, S. Y., and LAY, T. (1994), *The velocity structure of the crust and upper mantle under China from broad-band P and PP waveform analysis*. Geophys. J. Int. *119*, 574–594, doi:10.1111/j.1365-246X.1994.tb00143.x.
- BILEK, S. L. (2007), *Using earthquake source durations along the Sumatra-Andaman subduction system to examine fault-zone variations*. Bull. Seismol. Soc. Am. *97*, S62–S70.
- BILEK, S. L., and LAY, T. (1998), *Variation of interplate fault zone properties with depth in the Japan subduction zone*. Science *281*, 1175–1178.
- BILEK, S. L., and LAY, T. (1999), *Comparison of depth dependent fault zone properties in the Japan trench and middle America trench*. PAGEOPH *154*, 433–456.
- BINA, C. R. (1991), *Mantle discontinuities*. Rev. Geophys. Suppl. , 783–793.
- BIRD, P. (1978), *Initiation of intracontinental subduction in the Himalayas*. J. Geophys. Res. *83*, 4975–4987.
- BOS, A. G., NOLET, G., RUBIN, A., HOUSTON, H., and VIDALE, J. E. (1998), *Duration of deep earthquakes determined by stacking of Global Seismograph Network seismograms*. J. Geophys. Res. *103*, 21059–21065.

- BRUDZINSKI, M. R., and CHEN, W.-P. (2000), *Variation in P wave speeds and outboard earthquakes: Evidence for a petrologic anomaly in the mantle transition zone*. J. Geophys. Res. *105*, No. B9, 21661–21682.
- CHEN, W. P. (1988), *A brief update on the focal depths of intracontinental earthquakes and their correlation with heat flow and tectonic age*. Seismol. Res. Lett. *59*, 263–272.
- CHEN, W.-P., and MOLNAR, P. (1975), *Short-period Rayleigh-wave dispersion across the Tibetan Plateau*. Bull. Seismol. Soc. Am. *65*, 1051–1057.
- CHEN, W.-P., and MOLNAR, P. (1983), *Focal depths of intracontinental and intraplate earthquakes and their implications for the thermal and mechanical properties of the lithosphere*. J. Geophys. Res. *88*, 4183–4124.
- CHEN, W.-P., and MOLNAR, P. (1990), *Source parameters of earthquakes and intraplate deformation beneath the Shillong Plateau and the northern Indoburman ranges*. J. Geophys. Res. *95*, 12527–12552.
- CHEN, W.-P., and TSENG, T.-L. (2007), *Small 660-km seismic discontinuity beneath Tibet implies resting ground for detached lithosphere*. J. Geophys. Res. *112*, B05309, doi:10.1029/2006JB004607.
- CHEN, W.-P., and YANG, Z. (2004), *Earthquakes beneath the Himalayas and Tibet: Evidence for strong lithospheric mantle*. Science *304*, 1949, doi:10.1126/science.1097324.
- CHEN, W.-P., NÁBELEK, J. L., FITCH, T. J., and MOLNAR, P. (1981), *An intermediate depth earthquake beneath Tibet: Source characteristics of the event of September 14, 1976*. J. Geophys. Res. *86*, 2863–2876.
- CHUN, K.-Y., and YOSHII, T. (1977), *Crustal structure of the Tibetan Plateau: A surface wave study by a moving window analysis*. Bull. Seismol. Soc. Am. *67*, 735–750.
- COTTE, N., PEDERSEN, H., CAMPILLO, M., MARS, J., NI, J. F., *et al.* (1999), *Determination of the crustal structure in southern Tibet by dispersion and amplitude analysis of Rayleigh waves*. Geophys. J. Int. *138*, 809–819.
- CURTIS, A., and WOODHOUSE, J. H. (1997), *Crust and upper mantle shear velocity structure beneath the Tibetan plateau and surrounding regions from interevent surface wave phase velocity inversion*. J. Geophys. Res. *102*, 11789–11814, doi:10.1029/96JB03182.
- CURTIS, A., TRAMPERT, J., and SNIEDER, R. (1998), *Eurasian fundamental mode surface wave phase velocities and their relationship with tectonic structures*. J. Geophys. Res. *103*, 26919–26947.

- DE LA TORRE, T., and SHEEHAN, A. (2005), *Broadband seismic noise analysis of the Himalayan Nepal Tibet seismic experiment*. Bull. Seismol. Soc. Am. *95*, 1202–1208.
- DEUSS, A., and WOODHOUSE, J. H. (2001), *Seismic observations of splitting of the mid transition zone discontinuity*. Science *294*, 345–357.
- DEWEY, J. F., and BIRD, J. M. (1970), *Mountain belts and the new global tectonics*. J. Geophys. Res. *75*, 2625–2647.
- DEWEY, J. F., and BURKE, K. (1973), *Tibet, Variscan and Precambrian basement reactivation: Products of a continental collision*. J. Geol. *81*, 683–692.
- DEWEY, J. F., SHACKLETON, R. M., CHENG, F. R. S. C., and YIYIN, S. (1988), *The tectonic evolution of the Tibetan Plateau*. Philos. Trans. R. Soc. London *327*, 379–413.
- DREGER, D. S. (1994), *Empirical Green's function study of the January 17, 1994 Northridge, California earthquake*. Geophys. Res. Lett. *21*, 2633–2636.
- DZIEWONSKI, A. M., CHOU, T.-A., and WOODHOUSE, J. H. (1981), *Determination of earthquake source parameters from waveform data for studies of global and regional seismicity*. J. Geophys. Res. *86*, 2825–2852.
- EKSTRÖM, G., and DZIEWONSKI, A. M. (1985), *Centroid-moment tensor solutions for 35 earthquakes in western North America (1977-1983)*. Bull. Seismol. Soc. Am. *75*, 23–39.
- ENGLAND, P. C., and HOUSEMAN, G. A. (1986), *Finite strain calculations of continental deformation 2: Comparison with the India-Asia collision zone*. J. Geophys. Res. *91*, 3664–3676.
- ENGLAND, P. C., and MCKENZIE, D. P. (1982), *A thin viscous sheet model for continental deformation*. Geophys. J. R. astr. Soc. *70*, 295–321.
- FAN, G., NI, J. F., and WALLACE, T. C. (1994), *Active tectonics of the Pamirs and Karakorum*. J. Geophys. Res. *99*, 7131–7160.
- FAN, G. W., and WALLACE, T. C. (1991), *The determination of source parameters for small earthquakes from a single very broadband seismic station*. Geophys. Res. Lett. *18*, 1385–1388.
- GALVÉ, A., SAPIN, M., HIRN, A., DIAZ, J., LÉPINE, J.-C., *et al.* (2002), *Complex images of Moho and variation of V_p/V_s across the Himalaya and South Tibet, from a joint receiver-function and wide-angle-reflection approach*. Geophys. Res. Lett. *29*, 2182, doi:10.1029/2002GL015611.
- GANSER, A. (1980), *The significance of the Himalayan suture zone*. Tectonophysics. *62*, 37–52.

- GARNERO, E. J., HELMBERGER, D. V., and BURDICK, L. J. (1992), *Preliminary observations from the use of US-Soviet joint seismic program data to model upper mantle triplications beneath Asia*. *Geophys. J. Int.* *113*, 252–259.
- GIVEN, J. W., and HELMBERGER, D. V. (1980), *Upper mantle structure of northwestern Eurasia*. *J. Geophys. Res.* *85*, 7183–7194.
- GRAND, S. P., and HELMBERGER, D. V. (1985), *Upper mantle shear structure beneath Asia from multi-bounce S wave*. *Phys. Earth Planet. Inter.* *41*, 154–169.
- GUPTA, H. K., and NARAIN, H. (1967), *Crustal structure in the Himalayan and Tibet Plateau region from surface wave dispersion*. *Bull. Seismol. Soc. Am.* *57*, 235–248.
- HEARN, T. M., WANG, S., NI, J., XU, Z., YU, Y., *et al.* (2004), *Uppermost mantle velocities beneath China and surrounding regions*. *J. Geophys. Res.* *109*, B11301, doi:10.1029/2003JB002874.
- HELFFRICH, G. R. (1997), *How good are routinely determined focal mechanisms? Empirical statistics based on a comparison of Harvard, USGS and ERI moment tensors*. *Geophys. J. Int.* *131*, 741–750.
- HELMBERGER, D. V. (1973), *On the structure of the low velocity zone*. *Geophys. J. Int.* *34*, 251–263.
- HELMBERGER, D. V., *Theory and application of synthetic seismograms*, in *Earthquakes: Observation, Theory and Interpretation* (Soc. Italiana di Fisica, Bolgna, Italy 1983), pp. 174–222.
- HUANG, J., and ZHAO, D. (2006), *High-resolution mantle tomography of China and surrounding regions*. *J. Geophys. Res.* *111*, B09305, doi:10.1029/2005JB004066.
- HUANG, Z., SU, W., PENG, Y., ZHENG, Y., and LI, H. (2003), *Rayleigh wave tomography of China and adjacent regions*. *J. Geophys. Res.* *108*, 2073, doi:10.1029/2001JB001696.
- JIN, D. J., and ROGERS, J. R. (1983), *Homomorphic deconvolution*. *Geophysics* *48*, 1014–1016.
- JOBERT, N., JOURNET, B., HIRN, A., and ZHONG, S. K. (1985), *Deep structure of southern Tibet inferred from the dispersion of Rayleigh waves through a long-period seismic network*. *Nature* *313*, 386–388.
- JOHNSON, M. (2002), *Shortening budgets and the role of continental subduction during the India-Asia collision*. *Earth Sci. Rev.* *59*, 101–123.
- KANAMORI, H., and ANDERSON, D. L. (1975), *Theoretical basis of some empirical relations in seismology*. *Bull. Seismol. Soc. Am.* *65*, 1073–1095.

- KAO, H., GAO, R., RAU, R., SHI, D., CHEN, R., *et al.* (2001), *Seismic image of the Tarim basin and its collision with Tibet*. *Geology* 29, 575–578.
- KAYAL, J. R. (1987), *Microseismicity and source mechanism study: Shillong Plateau, northeast India*. *Bull. Seismol. Soc. Am.* 77, 184–194.
- KAYAL, J. R., and ZHAO, D. (1998), *Three-dimensional seismic structure beneath Shillong Plateau and Assam Valey, Northeast India*. *Bull. Seismol. Soc. Am.* 88, 667–676.
- KENNETT, B. L. N., and ENGDAHL, E. R. (1991), *Travel times for global earthquake location and phase identification*. *Geophys. J. Int.* 105, 429–465.
- KIKUCHI, M., and KANAMORI, H. (1982), *Inversion of complex body waves*. *Bull. Seismol. Soc. Am.* 72, 491–506.
- KIND, R., YUAN, X., SAUL, J., NELSON, D., SOBOLEV, S. V., *et al.* (2002), *Seismic images of crust and upper mantle beneath Tibet: Evidence for Eurasian Plate Subduction*. *Science* 298, 1219–1221, doi: 10.1126/science.1078115.
- KOPNICHEV, Y. F., SHEPELEV, O. M., and SOKOLOVA, I. N. (2001), *Seismic discrimination of nuclear explosions at the Lobnor test site*. *Izvestiya, Phys. of Solid Earth* 37, 1026–1038.
- KOSAREV, G., KIND, R., SOBOLEV, S. V., YUAN, X., HANKA, W., *et al.* (1999), *Seismic evidence for a detached Indian lithospheric mantle beneath Tibet*. *Science* 283, 1306–1309.
- KOULAKOV, I., and SOBOLEV, S. V. (2006), *A tomographic image of Indian lithosphere break-off beneath the Pamir-Hindukush region*. *Geophys. J. Int.* 164, 425–440.
- KUMAR, P., YUAN, X., KIND, R., and KOSAREV, G. (2005), *The lithosphere-asthenosphere boundary in the Tien Shan-Karakoram region from S receiver functions: Evidence for continental subduction*. *Geophys. Res. Lett.* 32, 7305, doi:10.1029/2004GL022291.
- KUMAR, P., YUAN, X., KIND, R., and NI, J. (2006), *Imaging the colliding Indian and Asian lithospheric plates beneath Tibet*. *J. Geophys. Res.* 111, B06308, doi: 10.1029/2005JB003930.
- LE DAIN, A. Y., TAPPONNIER, P., and MOLNAR, P. (1984), *Active faulting and tectonics of Burma and surrounding regions*. *J. Geophys. Res.* 89, 453–472.
- LEBEDEV, S., and VAN DER HILST, R. D. (2008), *Global upper-mantle tomography with the automated multi-mode surface and S waveforms*. *Geophys. J. Int.* , doi:10.1111/j.1365-246X.2008.03721.x.

- LI, C., VAN DER HILST, R. D., and TOKSÖZ, N. M. (2006), *Constraining spatial variations in P-wave velocity in the upper mantle beneath SE Asia*. *Phys. Earth Planet. Inter.* *154*, 180–195.
- LI, C., VAN DER HILST, R. D., MELTZER, A. S., and ENGDAHL, E. R. (2008), *Subduction of the Indian lithosphere beneath the Tibetan Plateau and Burma*. *Earth Planet. Sci. Lett.* *274*, 157–168.
- LIANG, C., and SONG, X. (2006), *A low velocity belt beneath northern and eastern Tibetan Plateau from P_n tomography*. *J. Geophys. Res.* *33*, L22306, doi:10.1029/2006GL027926.
- LIANG, C., SONG, X., and HUANG, J. (2004), *Tomographic inversion of P_n travel times in China*. *J. Geophys. Res.* *109*, B11304, doi:10.1029/2003JB002789.
- LIU, M., CUI, X., and LIU, F. (2004), *Cenozoic rifting and volcanism in eastern China: a mantle dynamic link to the Indo-Asian collision?* *Tectonophysics* *393*, 29–42.
- LIU, N., CHEN, Q.-F., NIU, F., and CHEN, Y. (2007), *Rupture of the 2004 Sumatra-Andaman earthquake inferred from direct P-wave imaging*. *Sci. in China Series D-Earth Sci.* *52*, 1312–1316.
- LYON-CAEN, H. (1986), *Comparison of the upper mantle shear wave velocity structure of the Indian Shield and the Tibetan Plateau and Tectonic Implications*. *Geophys. J. Int.* *86*, 727–749, doi:10.1111/j.1365-246X.1986.tb00657.x.
- MAGGI, A., JACKSON, J. A., MCKENZIE, D., and PRIESTLEY, K. (2000a), *Earthquake focal depths, effective elastic thickness, and the strength of the continental lithosphere*. *Geology* *28*, 495–498.
- MAGGI, A., JACKSON, J. A., PRIESTLEY, K., and BAKER, C. (2000b), *A re-assessment of focal depth distributions in southern Iran, the Tien Shan and northern India: do earthquakes really occur in the continental mantle?* *Geophys. J. Int.* *143*, 629–661.
- MARTYNOV, V. G., VERNON, F. L., MELLORS, R. J., and PAVLIS, G. L. (1999), *High-frequency attenuation in the crust and upper mantle of the northern Tien Shan*. *Bull. Seismol. Soc. Am.* *89*, 215–238.
- MCMANARA, D. E., WALTER, W. R., OWENS, T. J., and AMMON, C. J. (1997), *Upper mantle velocity structure beneath the Tibetan Plateau from P_n travel time tomography*. *J. Geophys. Res.* *102*, 493–505.
- MELLORS, R. J. (2005), *Two studies in central Asian seismology: A teleseismic study of the Pamir/Hindu Kush seismic zone and analysis of data from the Kyrgyzstan broadband seismic network*, Ph.D. thesis, Indiana University.

- MELLORS, R. J., PAVLIS, G. L., HAMBURGER, M. W., AL-SHUKRI, H. J., and LUKK, A. A. (1995), *Evidence for a high-velocity slab associated with the Hindu Kush seismic zone*. *J. Geophys. Res.* *100*, 4067–4078.
- MELTZER, A. S., ZEITLER, P. K., SCHOEMANN, M. L., BEAUDOIN, B. C., SEEBER, L., *et al.* (1996), *The Nanga Parbat Seismic Experiment*. *Eos Trans. AGU* *77*, Fall Meeting Suppl., Abstract T12E–09.
- MELTZER, A. S., SARKER, G., BEAUDOIN, B., SEEBER, L., and ARMBRUSTER, J. G. (2001), *Seismic characterization of an active metamorphic massif, Nanga Parbat, Pakistan Himalaya*. *Geology* *29*, 651–654.
- MITRA, S., PRIESTLEY, K., BHATTACHARYYA, A. K., and GAUR, V. K. (2005), *Crustal structure and earthquake focal depths beneath northeastern India and southern Tibet*. *Geophys. J. Int.* *160*, 227–248.
- MOLNAR, P., and CHEN, W.-P. (1983), *Focal depths and fault plane solutions of earthquakes under the Tibetan Plateau*. *J. Geophys. Res.* *88*, 1180–1196.
- MOLNAR, P., and LYON-CAEN, H. (1989), *Fault plane solutions of earthquakes and active tectonics of the Tibetan Plateau and its margins*. *Geophys. J. Int.* *99*, 123–153.
- MOLNAR, P., and TAPPONNIER, P. (1975), *Cenozoic tectonics of Asia: Effects of a continental collision*. *Science* *189*, 419–426.
- MOLNAR, P., FITCH, T. J., and WU, F. T. (1973), *Fault plane solutions of shallow earthquakes and contemporary tectonics in Asia*. *Earth Planet. Sci. Lett.* *19*, 101–112.
- MOLNAR, P., CHEN, W.-P., FITCH, T. J., TAPPONNIER, P., WARSI, W. E. K., *et al.* (1977), *Structure and tectonics of the Himalaya: A brief summary of relevant geophysical observations*. *Himalaya: Sciences de la Terre*, Paris: Ed. Cent. Natl. Rech. Sci., 269–294.
- MOLNAR, P., ENGLAND, P., and MARTINOD, J. (1993), *Mantle dynamics, uplift of the Tibetan Plateau, and the Indian monsoon*. *Rev. Geophys.* *31*, 357–396.
- MONSALVE, G., SHEEHAN, A., SCHULTE-PELKUM, V., RAJAURE, S., PANDEY, M. R., *et al.* (2006), *Seismicity and one-dimensional velocity structure of the Himalayan collision zone: Earthquakes in the crust and upper mantle*. *J. Geophys. Res.* *111*, B10301, doi:10.1029/2005JB004062.
- NELSON, K. D., ZHAO, W. J., BROWN, L. D., KUO, J., CHE, J. K., *et al.* (1996), *Partially molten middle crust beneath southern Tibet - synthesis of Project INDEPTH results*. *Science* *274*, 1684–1688.

- NI, J., and BARAZANGI, M. (1983), *High-frequency seismic-wave propagation beneath the Indian shield, Himalayan arc, Tibetan plateau and surrounding regions – high uppermost mantle velocities and efficient S_n propagation beneath Tibet*. Geophys. J. R. astr. Soc. *72*, 665–689.
- OWENS, T. J., and ZANDT, G. (1997), *Implications of crustal property variations for models of Tibetan plateau evolution*. Nature *387*, 37–43.
- OWENS, T. J., RANDALL, G. E., WU, F. T., and ZENG, R. S. (1993), *PASSCAL instrument performance during the Tibetan plateau passive seismic experiment*. Bull. Seismol. Soc. Am. *83*, 1959–1970.
- PAVLIS, G. L., and DAS, S. (2000), *The Pamir-Hindu Kush seismic zone as a strain marker for flow in the upper mantle*. Tectonics *19*, 103–115.
- PEGLER, G., and DAS, S. (1998), *An enhanced image of the Pamir-Hindu Kush Seismic zone from relocated earthquake hypocenters*. Geophys. J. Int. *134*, 573–595, doi:10.1046/j.1365-246x.1998.00582.x.
- PEI, S., ZHAO, J., SUN, Y., XU, Z., WANG, S., *et al.* (2007), *Upper mantle seismic velocities and anisotropy in China determined through P_n and S_n tomography*. J. Geophys. Res. *112*, B05312, doi:10.1029/2006JB004409.
- POWELL, C. M., and CONAGHAN, P. J. (1973), *Plate tectonics and the Himalayas*. Earth Planet. Sci. Lett. *20*, 1–12.
- POWELL, C. M., and CONAGHAN, P. J. (1975), *Tectonic models of the Tibetan Plateau*. Geology *3*, 727–731.
- PRIESTLEY, K., JACKSON, J., and MCKENZIE, D. (2008), *Lithospheric structure and deep earthquakes beneath India, the Himalaya and southern Tibet*. Geophys. J. Int. *172*, 345–362.
- RAPINE, R., TILMANN, F., WEST, M., NI, J., and RODGERS, A. (2003), *Crustal structure of northern and southern Tibet from surface wave dispersion analysis*. J. Geophys. Res. *108*, 2120, doi:10.1029/2001JB000445.
- REPLUMAZ, A., KÁRASON, H., VAN DER HILST, R. D., BESSE, J., and TAPPONNIER, P. (2004), *4-D evolution of SE Asia’s mantle from geological reconstructions and seismic tomography*. Earth Planet. Sci. Lett. *221*, 103–115.
- RITZWOLLER, M. H., and LEVSHIN, A. L. (1998), *Eurasian surface wave tomography: Group velocities*. J. Geophys. Res. *103*, 4839–4878.
- RITZWOLLER, M. H., BARMIN, M. P., VILLASENÑOR, A., LEVSHIN, A. L., and ENGDAHL, E. R. (2002), *P_n and S_n tomography across Eurasia to improve regional seismic event locations*. Tectonophysics *358*, 39–55.

- RODGERS, A. J., and SCHWARTZ, S. Y. (1998), *Lithospheric structure of the Qiangtang Terrane, northern Tibetan Plateau, from complete regional waveform modeling: Evidence for partial melt*. J. Geophys. Res. *103*, 7137–7152.
- ROECKER, S. (1999), *New constraints on the crust and upper mantle of the Kyrgyz Tien Shan from the analysis of GHENGIS broadband seismic data*. Eos Trans. AGU, Fall Meeting Suppl., Abstract T41C–14.
- SCHULTE-PELKUM, V., MONSALVE, G., SHEEHAN, A., PANDEY, M. R., SAPKOTA, S., *et al.* (2005), *Imaging the Indian subcontinent beneath the Himalaya*. Nature *435*, 1222–1225.
- SHEARER, P. M. (2000), *Upper mantle seismic discontinuities*. Geophys. Monogr. *117*, 115–131.
- SOL, S., MELTZER, A., BÜRGMANN, R., VAN DER HILST, R. D., KING, R., *et al.* (2007), *Geodynamics of the southeastern Tibetan Plateau from seismic anisotropy and geodesy*. Geology *35*, 563–566, DOI: 10.1130/G23408A.1.
- SOMERVILLE, P. G., MCLAREN, J. P., LEFEVRE, L. V., BURGER, R. W., and HELMBERGER, D. V. (1987), *Comparison of source scaling relations of eastern and western North American earthquakes*. Bull. Seismol. Soc. Am. *77*, 322–346.
- SONG, T.-R. A., HELMBERGER, D. V., and GRAND, S. (2004), *Low velocity zone atop the 410 seismic discontinuity in the northwestern US*. Nature *427*, 530–533.
- SUN, Y., and TOKSÖZ, M. N. (2006), *Crustal structure of China and surrounding regions from P wave travelttime tomography*. J. Geophys. Res. *111*, B03310, doi:10.1029/2005JB003962.
- TAPPONNIER, P., XU, Z., ROGER, F., MEYER, B., ARNAUD, N., *et al.* (2001), *Oblique stepwise rise and growth of the Tibet Plateau*. Science *294*, 1671–1677, doi: 10.1126/science.105978.
- TILMANN, F., NI, J., and INDEPTH III SEISMIC TEAM (2003), *Downwelling Indian lithosphere beneath central Tibet*. Science *300*, 1424, doi: 10.1126/science.1082777.
- ULRYCH, T. J. (1971), *Application of homomorphic deconvolution to seismology*. Geophysics *36*, 650–660.
- VAN DER HILST, R. D., CHEN, Z., LI, C., LEV, E., XU, L., *et al.* (2005), *Crust and upper mantle structure beneath Sichuan/Yunnan provinces, SW China: Preliminary results of a joint MIT-CIGMR broad-band seismometry project*. Eos Trans. AGU *87*, West. Pac. Geophys. Meet. Suppl., Abstract S41A–01.
- VAN DER VOO, R. (1999), *Tethyan subducted slabs under India*. Earth Planet. Sci. Lett. *171*, 7–20.

- VELASCO, A. A., MILLER, K. C., HOLLISTER, L. S., FORT, M., HARDER, S., *et al.* (2002), *A pilot earthquake seismic network in Bhutan: preliminary results*. Eos Trans. AGU, Fall Meeting Suppl., Abstract S51B–1044.
- VELASCO, A. A., GEE, V. L., BOWE, C., GRUJIC, D., HOLLISTER, L. S., *et al.* (2007), *Using small, temporary seismic networks for investigating tectonic deformation: Brittle deformation and evidence for strike slip faulting in Bhutan*. Seismol. Res. Lett. 78, 446–453.
- VERGNE, J., WITTLINGER, G., HUI, Q., TAPPONNIER, P., POUPINET, G., *et al.* (2002), *Seismic evidence for stepwise thickening of the crust across the NE Tibetan plateau*. Earth Planet. Sci. Lett. 203, 25–33.
- VILLASEÑOR, A., RITZWOLLER, M. H., LEVSHIN, A. L., BARMIN, M. P., ENGDAHL, E. R., *et al.* (2001), *Shear velocity structure of central Eurasia from inversion of surface wave velocities*. Phys. Earth Planet. Inter. 123, 169–184.
- WANG, C., SILVER, P., ZHU, L., and CHAN, W. (2006), *Seismic experiment along 30N in the east Tibetan and west Sichuan, China*. Eos Trans. AGU 87, West. Pac. Geophys. Meet. Suppl., Abstract S41A–0162.
- WANG, Q., ZHANG, P. Z., FREYMUELLER, J. T., BILHAM, R., LARSON, K. M., *et al.* (2001), *Present-day deformation in China constrained by global positioning system measurements*. Science 294, 574–577.
- WILLET, S. D., and BEAUMONT, C. (1994), *Subduction of Asian lithospheric mantle beneath Tibet inferred from models of continental collision*. Nature 369, 643–645.
- WITTLINGER, G., VERGNE, J., TAPPONNIER, P., FARRA, V., POUPINET, G., *et al.* (2004), *Teleseismic imaging of subducting lithosphere and Moho offsets beneath western Tibet*. Earth Planet. Sci. Lett. 221, 117–130, 10.1016/S0012-821X(03)00723-4.
- WU, F. T., LEVSHIN, A. L., and KOZHEVNIKOV, V. M. (1997), *Rayleigh wave group velocity tomography of Siberia, China and the vicinity*. PAGEOPH 149, 447–473.
- XU, Y., LIU, F., LIU, J., and CHEN, H. (2002), *Crust and upper mantle structure beneath western China from P wave travel time tomography*. J. Geophys. Res. 107, 2220, doi:10.1029/2001JB000402.
- YAO, H., XU, G., ZHU, L., and XIAO, X. (2005), *Mantle structure from inter-station Rayleigh wave dispersion and its tectonic implication in western China and neighboring regions*. Phys. Earth Planet. Inter. 148, 39–54.
- YIN, A., and HARRISON, T. N. (2000), *Geologic evolution of the Himalayan-Tibetan orogen*. Annu. Rev. Earth Planet. Sci. 28, 211–280.

- YUAN, X., NI, J., KIND, R., MECHIE, J., and SANDVOL, E. (1997), *Lithospheric and upper mantle structure of southern Tibet from a seismological passive source experiment*. *J. Geophys. Res.* *102*, 27491–27500.
- ZHAO, L. S., and XIE, J. (1993), *Lateral variations in compressional velocities beneath the Tibetan Plateau from Pn travelttime tomography*. *Geophys. J. Int.* *115*, 1070–1084, doi:10.1111/j.1365–246X.1993.tb01510.x.
- ZHAO, L. S., HELMBERGER, D. V., and HARKRIDER, D. G. (1991), *Shear-velocity structure of the crust and upper mantle beneath the Tibetan Plateau and southeastern China*. *Geophys. J. Int.* *105*, 713–730.
- ZHAO, W. (2001), *Crustal structure of central Tibet as derived from project INDEPTH wide angle seismic data*. *Geophys. J. Int.* *145*, 486–498.
- ZHAO, W., and MORGAN, J. (1985), *Uplift of the Tibetan Plateau*. *Tectonics* *4*, 359–369.
- ZHAO, W., and MORGAN, W. J. (1987), *Injection of Indian crust into Tibetan lower crust: a two-dimensional finite element model study*. *Tectonics* *6*, 489–504.
- ZHAO, W., NELSON, K. D., and TEAM, P. I. (1993), *Deep seismic reflection evidence for continental underthrusting beneath southern Tibet*. *Nature* *366*, 557–559.
- ZHOU, H., and MURPHY, M. A. (2005), *Tomographic evidence for wholesale underthrusting of India beneath the entire Tibetan Plateau*. *J. Asian Earth Sci.* *25*, 445–457.
- ZHU, L. (1998), *Broadband waveform modeling and its application to the lithospheric structure of the Tibetan Plateau*, Ph.D. thesis, California Institute of Technology, Pasadena, CA.
- ZHU, L., and HELMBERGER, D. V. (1996), *Intermediate depth earthquakes beneath the India-Tibet collision zone*. *Geophys. Res. Lett.* *23*, 435–438, doi:10.1029/96GL00385.
- ZHU, L., and HELMBERGER, D. V. (1998), *Moho offset across the northern margin of the Tibetan Plateau*. *Science* *281*, 1170–1172.
- ZHU, L., OWENS, T. J., and RANDALL, G. E. (1995), *Lateral variation in crustal structure of the northern Tibetan Plateau inferred from teleseismic receiver functions*. *Bull. Seismol. Soc. Am.* *85*, 1531–1540.
- ZHU, L., HELMBERGER, D. V., SAIKIA, C. K., and WOODS, B. B. (1997), *Regional waveform calibration in the Pamir-Hindu Kush region*. *J. Geophys. Res.* *102*, 22799–22813, doi:10.1029/97JB01855.

Vita Auctoris

Risheng Chu was born in Yuexi, China in December 1978. He went to Yuexi Middle School in 1994. After 3 years' hard work, he was enrolled in the Department of Earth and Space Sciences, University of Science and Technology of China (USTC) in 1997, majoring in geophysics.

In 2000, Mr. Chu worked in the Seismology Laboratory of USTC as an undergraduate researcher under the supervision of Dr. Guoming Xu. The main purpose of his research was to develop a program with Visual Basic to visualize a 3D velocity tomographic model in eastern China. This work led to his B.S. thesis.

After he obtained his B.S. degree, Mr. Chu came to the United States in August 2002 to study geophysics at the Department of Earth and Atmospheric Sciences, Saint Louis University under the supervision of Dr. Lupei Zhu. He expects to receive his Ph.D degree in April, 2008 and is planning to continue his research as a post-doc at the Seismo Lab, Caltech.